ADVANCED DATA-DRIVEN METHODS FOR AUTOMOTIVE BATTERY HEALTH PROGNOSTICS

WESLEY POH QI TONG

School of Electrical & Electronic Engineering

A thesis submitted to the Nanyang Technological University
in partial fulfilment of the requirement for the degree of
Doctor of Philosophy

2025

Statement of Originality

I hereby certify that the work embodied in this thesis is the result of original research, is free of plagiarised materials, and has not been submitted for a higher degree to any other University or Institution.

10-01-2025

Date

Wesley Poh Qi Tong

Supervisor Declaration Statement

I have reviewed the content and presentation style of this thesis and declare it is free of plagiarism and of sufficient grammatical clarity to be examined. To the best of my knowledge, the research and writing are those of the candidate except as acknowledged in the Author Attribution Statement. I confirm that the investigations were conducted in accord with the ethics policies and integrity standards of Nanyang Technological University and that the research data are presented honestly and without prejudice.

10-01-2025

Date

Xu Yan

Authorship Attribution Statement

This thesis contains material from four papers published in the following peer-reviewed journals and conference proceedings in which I am listed as an author.

Chapter 1 contains information from the paper published as **W. Q. T. Poh**, Y. Xu, and R. T. P. Tan, “A Review of Machine Learning Applications for Li-Ion Battery State Estimation in Electric Vehicles,” in *2022 IEEE PES Innovative Smart Grid Technologies – Asia (ISGT Asia)*, Singapore, Nov. 2022, pp. 265–269, doi: 10.1109/ISGTAsia54193.2022.10003481.

The contributions of the co-authors are as follows:

- Prof. Xu and Mr. Tan provided the initial project direction, and they discussed the idea with me.
- I read the literatures and wrote the manuscript draft. Prof. Xu provided important advice and guidance during this process.
- Prof. Xu revised the manuscript.

Chapter 2 is from the following papers that have been published:

W. Q. T. Poh, Y. Xu, and R. T. P. Tan, “A Review of Machine Learning Applications for Li-Ion Battery State Estimation in Electric Vehicles,” in *2022 IEEE PES Innovative Smart Grid Technologies – Asia (ISGT Asia)*, Singapore, Nov. 2022, pp. 265–269, doi: 10.1109/ISGTAsia54193.2022.10003481.

W. Q. T. Poh, Y. Xu, W. Liu, and R. T. P. Tan, “Momentary Informatics based Data-Driven Estimation of Lithium-Ion Battery Health Under Dynamic Discharging Currents,” *J. Power Sources*, vol. 629, pp. 236041, Feb. 2025, doi: 10.1016/j.jpowsour.2024.236041.

For both papers, the contributions of the co-authors are as follows:

- Prof. Xu suggested the general idea of the research topic. I discussed the idea with Prof. Xu, Dr. Liu and Mr. Tan before implementing it.
- Dr. Liu and Mr. Tan provided me with the resources to begin the research.
- I read the literatures, performed the experiments, collected the data, and performed result analysis. Then, I discussed the results with Prof. Xu.

- I wrote the manuscript drafts. Prof. Xu revised the manuscripts.

Chapter 4 is published as **W. Q. T. Poh**, Y. Xu, and R. T. P. Tan, “Data-Driven Estimation of Li-Ion Battery Health using a Truncated Time-based Indicator and LSTM,” in *2023 IEEE Power & Energy Soc. General Meeting (PESGM)*, Orlando, FL, USA, Jul. 2023, pp. 1–5, doi: 10.1109/PESGM52003.2023.10252352.

The contributions of the co-authors are as follows:

- Prof. Xu and Mr. Tan provided the initial direction of the research topic, and they discussed the idea with me.
- I performed the simulations, collected the data and performed result analysis. Then, I discussed the results with Prof. Xu and Mr. Tan.
- I wrote the manuscript draft. Then, it was revised by Prof. Xu.
- Prof. Xu provided valuable comments on how to revise the manuscript.

Chapter 5 is published as **W. Q. T. Poh**, Y. Xu, W. Liu, and R. T. P. Tan, “Momentary Informatics based Data-Driven Estimation of Lithium-Ion Battery Health Under Dynamic Discharging Currents,” *J. Power Sources*, vol. 629, pp. 236041, Feb. 2025, doi: 10.1016/j.jpowsour.2024.236041.

The contributions of the co-authors are as follows:

- Prof. Xu suggested the general idea of the research topic. I discussed the idea with Prof. Xu, Dr. Liu and Mr. Tan before implementing it.
- Dr. Liu and Mr. Tan provided me with the resources to begin the research.
- I performed the experiments, collected the data and performed result analysis. Then, I discussed the results with Prof. Xu.
- I wrote the manuscript draft. Then, it was revised by Prof. Xu.

Chapter 6 is published as **W. Q. T. Poh**, Y. Xu, and R. T. P. Tan, “Data-Driven Estimation of Li-Ion Battery Health: Integrating GPT-4 With Distilled Lifelong Learning,” *IEEE Trans. Energy Convers*., vol. 40, no. 2, pp. 1682–1685, Jun. 2025, doi: 10.1109/TEC.2025.3548400.

The contributions of the co-authors are as follows:

- Prof. Xu provided the general idea of the research topic.
- Mr. Tan provided me with the resources to begin the research.
- I performed the experiments, collected the data and performed result analysis. Then, I discussed the results with Prof. Xu.
- I wrote the manuscript draft. Then, it was revised by Prof. Xu.

10-01-2025

Date

Wesley Poh Qi Tong

Acknowledgements

First and foremost, I would like to express my sincerest gratitude to my supervisor, the esteemed Cham Tao Soon Professor in Engineering, Associate Professor Xu Yan. In 2020, he offered me the opportunity to study as a PhD student in his Stability, Optimization and Data-Analytics (SODA) power system research group, with financial support from the Economic Development Board of Singapore's Industrial Postgraduate Programme (IPP) Scholarship. Hence, I have the chance to work on this promising, industry-relevant research topic for my PhD degree at Nanyang Technological University (NTU), in collaboration with Infineon Technologies. I am grateful to Prof. Xu for his vast knowledge, professional insight and patient guidance. I also deeply appreciate the time and effort he dedicated to reviewing my work, offering constructive advice, and fostering a supportive environment for my personal and professional development. Prof. Xu is strongly passionate towards research and sets a very high standard for himself, which inspired me to conduct research with critical thinking while paying meticulous attention to research details. This in turn enabled me to innovate solutions that address real-world engineering problems.

I would also like to give many thanks to the senior members of the SODA Group, namely Dr. Gou Bin, Dr. Liu Wei, and Dr. Benjamin Chew. When I first joined the group, they shared valuable resources and advice to prepare me for my research in data-driven methods for battery health prognostics. Through their guidance, I managed to overcome the initial challenges in my PhD journey and improve my research capabilities. Their expertise, coupled with insightful feedback, have shaped my research and academic development. Special thanks to Dr. Liu for his valuable guidance on the aspect of battery aging data analytics.

Additionally, I would like to extend my deep gratitude to my industrial supervisor and collaborator, Mr. Robert Tan from Infineon Technologies. Through his mentorship, I have gained valuable hands-on experience and exposure to real-world applications which are essential to my growth as a researcher, and much of this is due to the opportunities he had provided. His ability to balance both

technical aptitude and practical relevance has been truly inspiring, and I have learned invaluable lessons that will stay with me throughout my career. My technical competence in the respective fields of firmware engineering, embedded machine learning, and battery management systems, have vastly improved during my tenure at Infineon Technologies.

Last but not least, I would like to express my deepest appreciation and gratitude to my family, especially my mother, for being the strongest pillar of support for me during my entire PhD candidature at NTU. Due to her constant encouragement, words of affirmation, and unconditional love, I was able to dig deep and attain the mental fortitude to complete my PhD while working at Infineon Technologies.

Wesley Poh Qi Tong

10 January 2025

Table of Contents

Summary

The advent of machine learning (ML) has led to the exploration of new methods to estimate the state-of-health (SOH) of lithium-ion batteries (LIBs) in automotive applications. Data-driven approaches involving ML are increasingly employed in battery prognostics due to the greater accessibility of historical battery data and the improved efficiency in computing systems. ML algorithms can self-learn through the intrinsic analysis of historical data, where a profound understanding of LIB electrochemistry principles is not required. Hence, they do not rely on presumptions derived from a battery model. The working principle of a data-driven approach is to first extract the health indicator (HI) from the battery charging/discharging process, and then estimate the SOH based on a trained ML model with the HI as input. Notably, the choice of the HI and the ML algorithm will affect the estimation performance. By obtaining accurate SOH estimates, timely maintenance can be carried out to avoid system failure.

At present, the battery management system (BMS) of electric vehicles (EVs) tends to face challenges in attaining highly accurate SOH estimates using traditional methods such as model-based methods and adaptive filter methods, since LIBs possess strong time-varying and non-linear traits whilst remaining susceptible to the influence of external factors (e.g., vehicle propulsion). Moreover, extensive lab condition-based battery testing is often required to model and parameterise the algorithms used in those methods. In the existing literature, most of the data-driven approaches are designed for conditions of constant-current (CC) charging/discharging at a specific rate over a long duration. However, the loading profiles of batteries can be highly volatile in an EV driving cycle, which restricts the application of existing data-driven methods. Proper SOH estimation is key to minimising overdesign costs of an LIB pack, and it constitutes the overall safety and reliability of an EV.

In light of the aforementioned motivations, this thesis develops robust, data-driven SOH estimation models that exploit the prediction capabilities of ML algorithms. On this basis, the following four contributions are made. Firstly, an in-depth review of the existing works on battery SOH estimation is performed, with a primary focus on data-driven approaches which include the extraction

and practical application of HIs. An analytical assessment of these methods is performed to determine their feasibility for on-board deployment in automotive BMSs. Herein, the advantages and drawbacks are identified, and improvements involving ML are recommended.

Secondly, battery aging data analytics is implemented to discover HIs that are not only practicable but also exhibit a strong correlation with SOH. In this regard, a novel HI, named the voltage disparity in truncated time interval (VDTTI), is extracted from a truncated time interval (110 s) of the LIB's discharge process, which is a challenge in literature since it is usually less controllable than the charge process. The VDTTI is derived from a short segment of voltage curves and since the segment can begin at any time spot, it is easy to extract from different voltage ranges. Furthermore, this HI can be extracted from either CC discharging or randomised discharging, which makes it highly flexible for application. Leveraging the subset of ML, the deep learning algorithm known as long short-term memory (LSTM) is employed to map the extracted VDTTI to the SOH. The testing results with an open dataset show that the proposed method can effectively capture the capacity regeneration trends of the LIB to output high-accuracy SOH estimations.

Thirdly, a hierarchical-ensembled ML model incorporating a new, momentary HI is proposed for online SOH estimation of LIBs under dynamic discharging. Extracted from a very short duration (< 0.1 s), the HI, named the electrical transient during short time interval (ETSTI), is exceptionally easy to derive and therefore applicable under various discharging currents and state-of-charge levels. The rationality of the ETSTI is to indirectly reflect battery internal ohmic resistance, which is justified by theoretical analysis with an equivalent circuit model. To evaluate the efficacy of the proposed method, hardware-in-the-loop experiments are performed using a BMS microcontroller that incorporates LIB test data derived from EV driving cycle profiles. The results show that the proposed method enables intelligent, stochastic-based learning of model weights across four esteemed ML algorithms used in the hierarchical ensemble model framework. Due to this, a much faster computation speed for high-accuracy SOH estimation performance is observed when compared to both single-model and average ensemble model frameworks.

Lastly, a novel SOH estimation method involving the generative pre-trained transformer-4 (GPT-4) and distilled lifelong learning (DLL) is proposed. The HI is extracted from partial charging voltage curves which are associated with the incomplete charging of an EV in real-world application. Then, the language-based perceptivity of the GPT-4 is converted to LIB data-based by only retraining its input and adaptors on the extracted HI based on selected LIB labels (vectorised text specifications). DLL is applied to enable robustness against data shifts and noise as it continuously updates the GPT model and retains vital knowledge. The proposed method is implemented in an application-centric BMS microcontroller for evaluation based on three unseen LIBs that are of varied chemistry. From the results, it is revealed that the proposed method is computationally cheap and highly precise when estimating SOH under fixed current and dynamic current profiles.

List of Figures

Page

List of Tables

Page

List of Abbreviations

AC	Alternating Current
AEM	Average Ensemble Model
BEV	Battery Electric Vehicle
BLS	Broad Learning System
BMS	Battery Management System
CC	Constant-Current
CCCT	Constant-Current Charge Time
CV	Constant-Voltage
CVCT	Constant-Voltage Charge Time
CNN	Convolutional Neural Network
CPU	Central Processing Unit
DL	Deep Learning
DLL	Distilled Lifelong Learning
DNN	Deep Neural Network
DTR	Decision Tree Regression
DV	Differential Voltage
DVA	Differential Voltage Analysis
DVDETI	Discharging Voltage Difference of Equal Time Interval
ECM	Equivalent Circuit Model
EEDVD	Energy of Equal Discharging Voltage Difference
EIS	Electrochemical Impedance Spectroscopy
EKF	Extended Kalman Filter
ELM	Extreme Learning Machine
EOL	End-Of-Life
ESS	Energy Storage System
ETSTI	Electrical Transient during Short Time Interval
EV	Electric Vehicle
FC	Fully Connected
FL	Fuzzy Logic
FNN	Feedforward Neural Network
fp32	32-Bit Floating Points

GPR	Gaussian Process Regression
GPT-4	Generative Pre-Trained Transformer-4
GPU	Graphics Processing Unit
GRU	Gated Recurrent Unit
GUI	Graphical User Interface
HEM	Hierarchical Ensemble Model
HI	Health Indicator
HIL	Hardware-in-the-Loop
HPPC	Hybrid Pulse Power Characterisation
IC	Incremental Capacity
ICA	Incremental Capacity Analysis
IDE	Integrated Development Environment
IES	Incremental Energy per State-Of-Charge
KF	Kalman Filter
KPCA	Kernel Principal Components Analysis
LFP	Lithium Iron Phosphate
LIB	Lithium-Ion Battery
LL	Lifelong Learning
LLM	Large Language Model
LS	Least Squares
LSTM	Long Short-Term Memory
MACC	Multiply-Accumulate
MiniGPT-4	Miniature Generative Pre-Trained Transformer-4
MF	Membership Function
MHA	Multi-Head Attention
ML	Machine Learning
MLP	Multi-Layer Perceptron
MMD	Maximum Mean Discrepancy
MOBO	Multi-Objective Bayesian Optimisation
NASA	National Aeronautics and Space Administration
NCA	Nickel Cobalt Aluminium Oxide
NMC	Nickel Manganese Cobalt Oxide
NN	Neural Network

OCV	Open-Circuit Voltage
PaLM-2	Pathways Language Model-2
PF	Particle Filter
PHEV	Plug-in Hybrid Electric Vehicle
P2D	Pseudo Two-Dimensional
RAM	Random Access Memory
RBF	Radial Basis Function
RC	Resistor-Capacitor
RF	Random Forest
RLS	Recursive Least Squares
RMSE	Root-Mean-Square Error
RNN	Recurrent Neural Network
SCC	Spearman Correlation Coefficient
SLFNN	Single Hidden Layer Feedforward Neural Network
SOC	State-Of-Charge
SOH	State-Of-Health
SPM	Single-Particle Model
SVM	Support Vector Machine
SVR	Support Vector Regression
TIEDVV	Time Interval of Equal Discharging Voltage Variance
TSECVC	Time Spots of Equispaced Charging Voltage Curve
TL	Transfer Learning
UART	Universal Asynchronous Receiver-Transmitter
UKF	Unscented Kalman Filter
VDEDT	Voltage Decline during Equal Discharge Time
VDTTI	Voltage Disparity in Truncated Time Interval
VKP	Voltage Knee Points
VVETI	Voltage Variance during Equal Time Interval
WLTP	Worldwide Harmonised Light Vehicles Test Procedure
XGBoost	Extreme Gradient Boosting

Chapter 1

Introduction

This chapter mainly introduces the background and motivations of the research topic. Firstly, the background and motivations for state-of-health (SOH) monitoring of lithium-ion batteries (LIBs) in automotive application are elaborated. Secondly, the existing challenges in battery SOH estimation are discussed. Thirdly, the objectives of this thesis to address existing challenges are specified. Thereafter, the contributions of this thesis are summarised. Finally, the organisation of this thesis is introduced.

1.1 Background and Motivations

1.1.1 Automotive Electrification and the Lithium-Ion Battery

The looming threat of a severe energy crisis as well as the dire need to achieve carbon neutrality has prompted governments worldwide to actively promote the development and usage of electric vehicles (EVs) as a mode of transport instead of internal combustion engine vehicles, hence attributing the reduction of fossil fuel consumption and carbon emissions through electrification. The two major EV types are the battery electric vehicle (BEV) [1] and plug-in hybrid electric vehicle (PHEV) [2], which possess components that operate on electricity as opposed to a conventional energy source. The lithium-ion battery (LIB) has become the preferred choice for energy storage in EVs due to its advantages such as high energy density, long lifetime, fast charging rate, high operating voltage platform, and low self-discharge [3].

Figure 1.1 shows the global EV adoption rate from 2014 to 2023 [4], while Figure 1.2 shows the global LIB demand and corresponding sales revenue attained from 2015 to 2024 [5]. It is evident from both figures that the EV and LIB uptake have rapidly increased over the past decade. Even under the impact of the Covid-19 pandemic, the global EV uptake still surged to 6.77 million in 2021. According to reports from the International Energy Agency [6], the global market for automotive LIBs is projected to grow from US$7.8 billion in 2015 to US$30.6 billion by the end of 2024. Concurrently, the LIB capacity serving the automotive

market is projected to grow from 15.9 GWh in 2015 to 93.1 GWh by the end of 2024. This increment denotes a compound annual growth rate of 21.7%, thereby suggesting continual, high demand for LIBs in the coming decades.

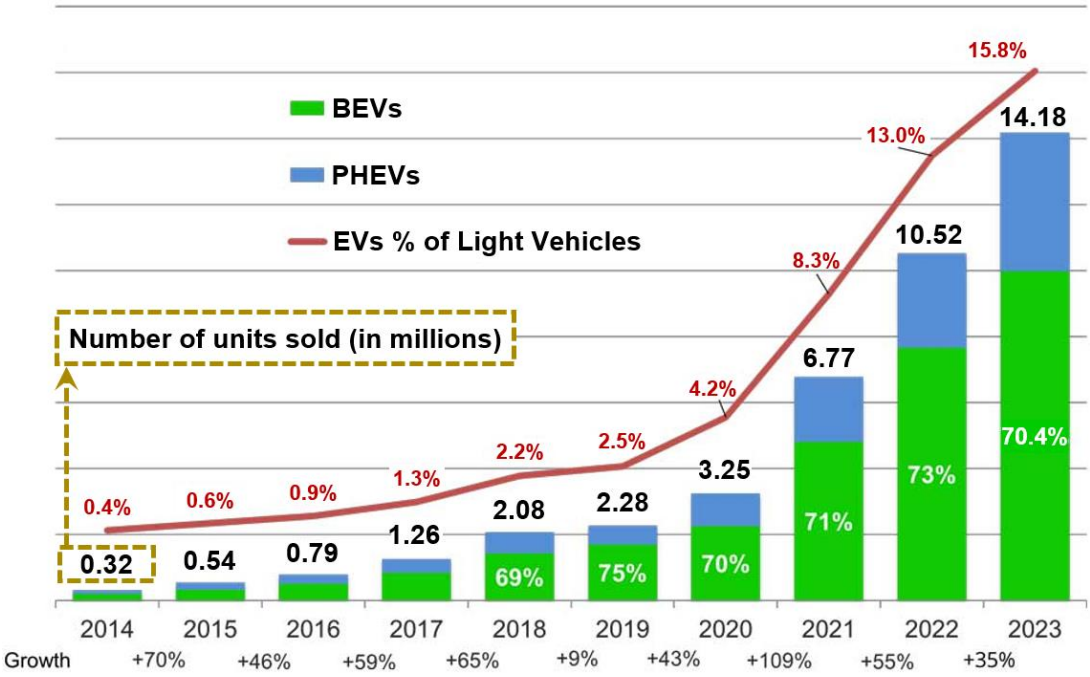

Figure 1.1. Global EV uptake from 2014 to 2023 [4].

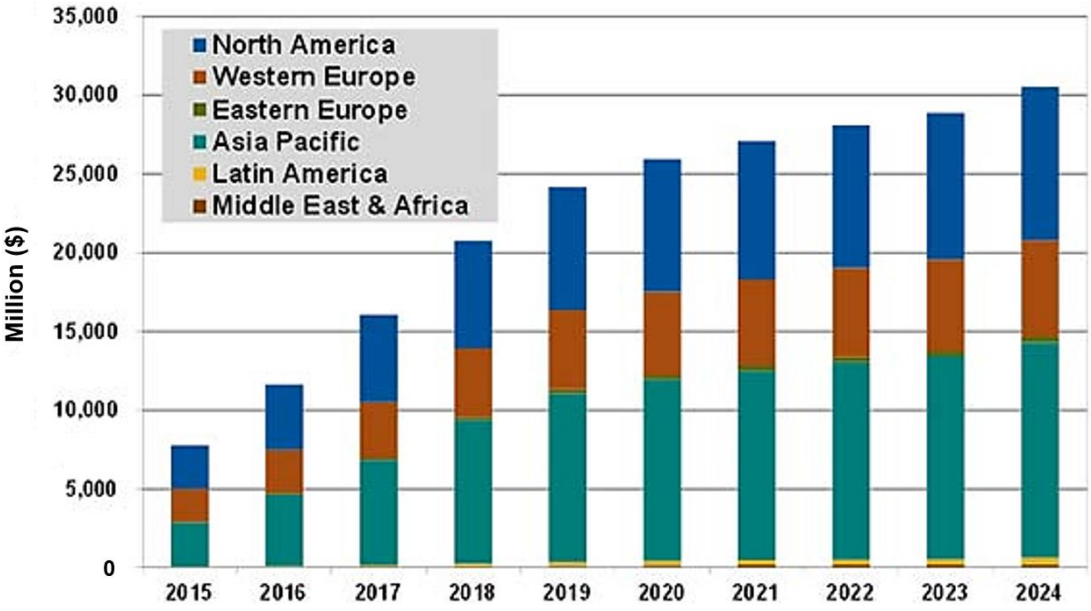

Figure 1.2. Global automotive LIB uptake and revenue from 2015 to 2024 [5].

On the aspect of LIB operations, charging and discharging of the LIB induces complex and irreversible electrochemical changes internally, resulting in the gradual decline of the battery health condition and performance. Figure 1.3

depicts the internal electrochemical reactions which occur during repeated charging and discharging, via the movement of the electrons. The electrons' movement could trigger irreversible, battery aging defects such as lithium plating, dendrite formation, graphite exfoliation, delamination (contact loss), and solid electrolyte interface formation [7]. In light of such phenomenon, coupled with the fact that an LIB pack is one of the costliest components in an EV, proper estimation of the LIB's states is key to minimising overdesign costs and increasing the overall vehicle efficiency, safety as well as reliability [7]–[9]. Thus, much effort has been concentrated on the software design of the EV's battery management system (BMS) to perform accurate state-of-charge (SOC) and state-of-health (SOH) estimation in real-time.

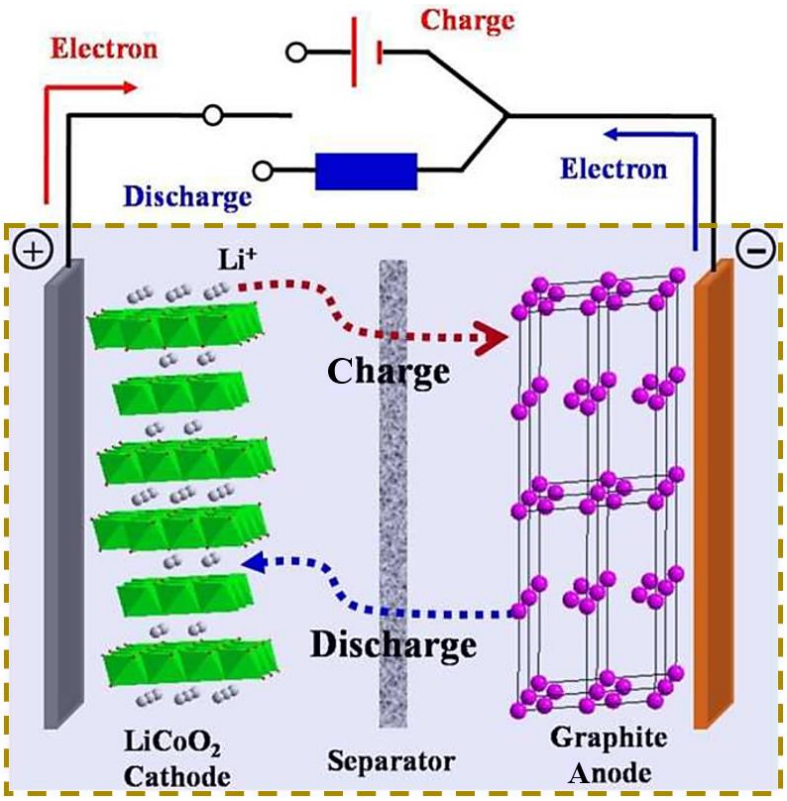

Figure 1.3. Schematic depiction of the charge/discharge process in an LIB [7].

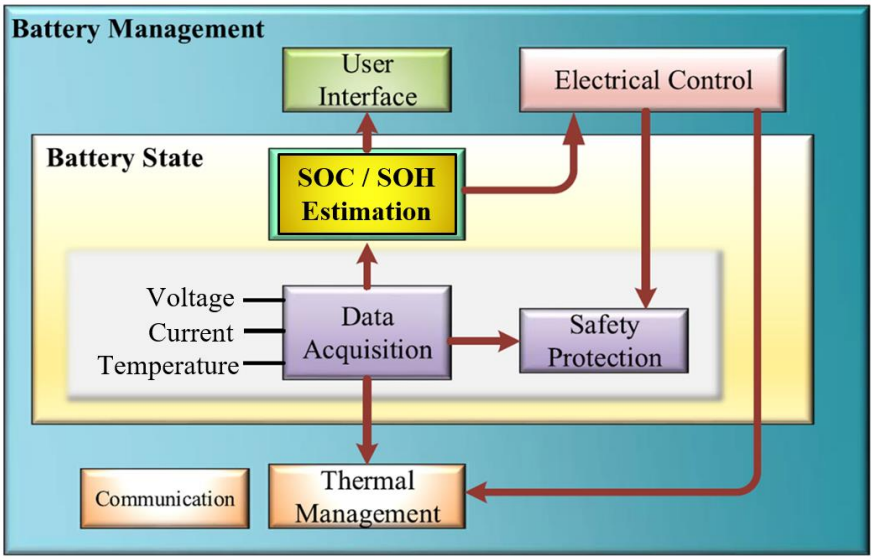

Figure 1.4. Block diagram of a battery management system (BMS) [3].

1.1.2 Battery State-Of-Health Estimation in Electric Vehicles

SOH represents the degree of battery aging relative to the battery's capacity loss or resistance increment, whereas SOC represents the level of charge of a battery relative to its capacity. The estimated SOC serves as an EV's energy gauge (i.e., the equivalent of a fuel gauge used in traditional gasoline vehicles), which constitutes the SOH, cell balancing and power computations. In mathematical terms [10], the SOC is generally defined as:

$$\mathrm{SOC} = \frac{C_{\mathrm{curr}}}{C_{\mathrm{full}}} \times 100\% \tag{1.1}$$

where C_{curr} is the capacity of the LIB in its current state, while C_{full} is the capacity of the LIB in its fully charged state. SOC is 100% when the LIB is fully charged and 0% when it is empty. A brand-new LIB's SOH is 100% and reaches 80% at end-of-life (EOL), which signifies that C_{full} has dipped to 80% of its nominal value. In mathematical terms [10], the SOH is generally defined as:

$$\mathrm{SOH} = \frac{C_{\mathrm{full}}}{C_{\mathrm{nom}}} \times 100\% \tag{1.2}$$

where C_{nom} is the nominal capacity of the brand-new LIB. The remaining number of charge/discharge cycles until the LIB reaches EOL is the remaining useful life of the LIB. Existing BMSs can determine the SOC of LIBs with an error margin of 0.6% to 5% [11]–[13], but are unable to predict the SOH of LIBs accurately.

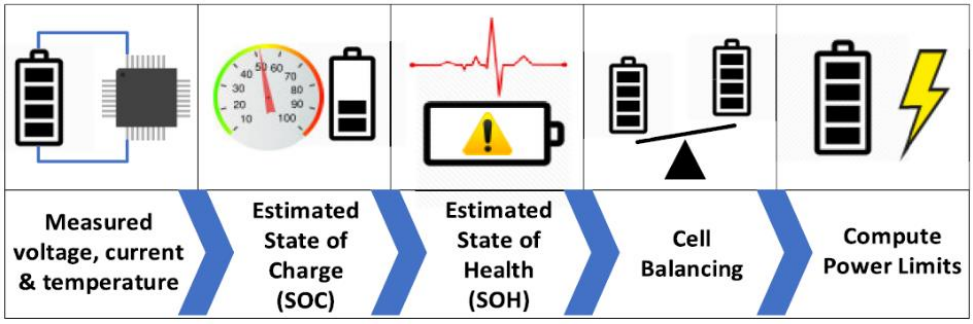

Figure 1.5. Typical BMS workflow involving SOH estimation [12].

As SOC and SOH are both not measurable, accurate estimation of these two parameters is necessary in order to avoid overcharge and deep discharge occurrences [1]. Such estimations can be attained via various online and offline methods, which differ in terms of complexity and accuracy. However, the influence of temperature changes, electromagnetic interference and external disturbances has caused SOC estimation to become a regular, non-linear instability problem in the context of EV-based LIBs. Estimating the SOH of LIBs is much more challenging due to a myriad of factors, both external and internal, that can influence battery performance and degradation. Notable examples of these factors include uncertain EV driving conditions and the complex physicochemical reactions that take place inside LIB cells [2].

Traditional methods have been implemented with attempts to address the aforementioned issues. The open-circuit voltage (OCV) method [14] is a simple offline SOC estimation technique, whereby its effectiveness is based on the correlation between the LIB's terminal voltage and SOC. However, this method is only relevant towards EV application if combined with a current integration based, online SOC estimation technique known as coulomb counting [15]. In addition, Kalman filter (KF) algorithms [16] are commonly incorporated to rectify the estimation errors before the SOH value can finally be obtained. The drawback of such hybrid methods is that they are compute-intensive and require an accurate LIB model to be effective, especially if considering the effects of ambient temperature on the LIB's performance [8], [9]. SOH methods relative to capacity estimation are generally based on ampere-hour counting between reference SOC points, whereas SOH methods for resistance estimation are more diverse; ranging from simple averaging of the change in voltage-current

ratio, to recursive algorithms [17]–[19]. Equivalent circuit models (ECMs) [20] are currently the main battery models that are used in the BMS of EVs for online estimations due to their low computational demand, but the accuracy is limited to the range that the model has been parameterised; which lacks comprehensive physics-based information. To ensure these methods [14]–[20] work well, significant lab condition-based battery testing is usually needed to model and parameterise the algorithms used. More robust and intricate state estimation techniques are required to handle the EVs' BMS sensor errors alongside uncertain model knowledge.

Contrastingly, machine learning (ML) inherently possesses the potential of self-learning from data with minimal reliance on mathematical models of physical systems, thus providing an effective solution that handles increased system complexity and uncertainty. With the recent technological breakthroughs in ML applications, data-driven machine ML models are being progressively used for battery state estimation [21]. This data-driven approach can practically handle the issues of non-linearity and instability found in the LIB data (or signals) measured by the BMS of EVs, and is able to make predictions without prior knowledge of the system. It only relies on the intrinsic analysis of historical data, where a profound understanding of LIB electrochemistry principles is not required.

The ML operations employ a sizeable amount of offline, LIB charge/discharge test cycle data, and the features extracted from raw voltage, current and temperature data are often used as training inputs to establish a mapping model of either the SOC or SOH. Generally, ML-based mapping models include neural network (NN), support vector machine (SVM), and deep learning (DL) methods [10]. The plethora of publicly available battery datasets has made it relevant to enhance BMS performance by combining data analytics with advanced ML algorithms. In the context of online SOC and SOH estimation involving ML, the main computational load demand only occurs during the offline training phase of an ML model; hence allowing feasible on-board deployment of the trained ML model in BMS hardware.

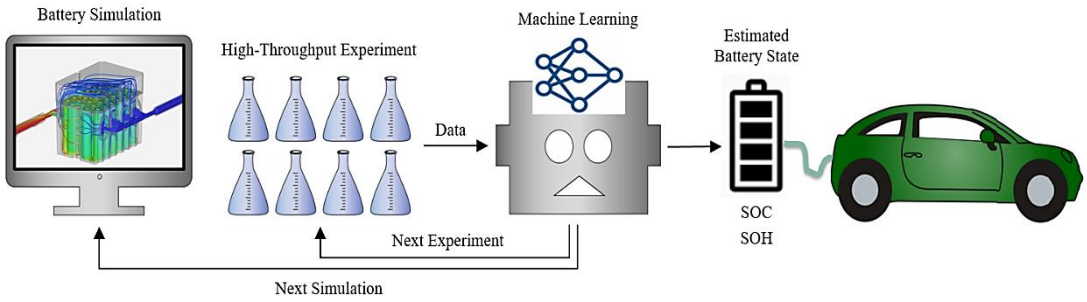

Figure 1.6. Data-driven approach involving ML for battery state estimation [21].

Current ML models need extensive training which uses large datasets derived from multi-scale battery modelling and high-throughput automation procedures. The training time is prolonged and requires GPU-based systems to expedite the entire training process. Notably, as most ML methods employ either a lengthy or fixed charging/discharging profile which fails to reflect real EV driving pattern (e.g., regenerative braking and torque profile), an effective training process is necessary for enhanced model performance.

Another key concern is the ML models' reliability towards online SOH estimation of LIBs; since capacity measurements traditionally involve a tedious coulomb counting test that spans across the entire SOC range (i.e., from 100% to 0%) using highly precise current measurements. The LIB's internal resistance can be directly measured too, using an electrochemical impedance spectroscopy (EIS) test [18] that applies a voltage signal over a range of amplitude and frequency to analyse the electrochemical changes within the LIB. Even so, the EIS test is unfeasible for online estimations as it can only be performed offline. It is worth noting that for an LIB in online operation, the capacity and internal resistance are both difficult to be measured directly. Coupled with the non-linear temperature and SOC dependent nature of LIBs, online SOH estimation is deemed a major automotive engineering challenge that has yet to be thoroughly addressed.

Recent literature have attempted to demonstrate the LIB's degradation-inherent relationship by detecting and extracting promising features known as health indicators (HIs). Estimating the SOH in real-time is crucial for LIB fault diagnosis and ensures an accurate SOC estimation. Moreover, extracting the appropriate HI effectively simplifies the mass of measured data and minimises computation

time. HIs are generally classified into two types, namely direct HIs and indirect HIs. A direct HI is an extracted feature based on offline, direct measurements such as EIS and coulomb counting, while an indirect HI is an extracted feature based on online, indirect measurements [22].

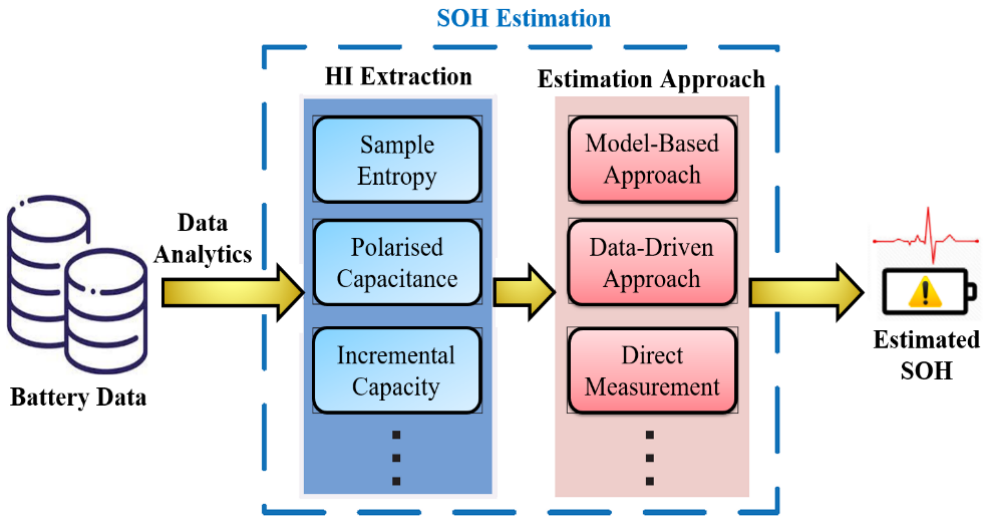

Figure 1.7. An SOH estimation framework based on HI extraction [10].

Since direct measurements are nearly impossible for on-board embedded systems such as automotive BMSs, indirect HIs are the ideal choice for quantifying SOH. Any indirect HI for online SOH estimation should be a derivative of voltage, current or temperature, i.e., the real-time measured variables from either charge mode or discharge mode of the LIB; while allowing extraction online. Although data-driven approaches are generally superior to model-based approaches in terms of simplicity and prediction accuracy [21], further research is needed to identify novel HIs that can complement the prediction capabilities of data-driven ML models.

1.2 Objectives

Considering all the above-discussed battery prognostics trends, it is evident that SOH estimation is a complicated and prevalent challenge faced by automotive BMSs. Therefore, seeking to overcome this challenge, the research objectives of this thesis are:

- To propose state-of-the-art, data-driven methods that reduce the complexities in battery data and training requirements of ML models. A

survey on ML algorithms and HIs that support the efficient transfer of knowledge in respect of high-quality, yet minimalistic data will be performed.

- To develop robust data-driven ML models that incorporate optimal training inputs for accurate, online SOH estimations of LIBs; with relevancy towards real-world EV usage. Through comprehensive battery aging data analytics, novel indirect HIs can be extracted from different charging/discharging profiles and inputted to the ML model.
- To evaluate and optimise the trained ML models for computational resource-efficient deployment in an SOH estimation framework.

1.3 Major Contributions of the Thesis

The major contributions of the thesis are summarised as follows:

1) A comprehensive review of the existing battery SOH estimation methods is conducted with a focus on HIs. These methods are comparatively studied with respect to the complexity of modelling, the extraction processes of the HIs, and the practical scenarios in which the HI-integrated models can be implemented. Their advantages and limitations are analytically identified, and further improvements involving ML are suggested.
2) A comprehensive analysis of the LIB aging data is performed to discover HIs that are not only practicable but also exhibit a strong correlation with the battery SOH. In this regard, a novel HI, named the voltage disparity in truncated time interval (VDTTI), is extracted for SOH estimation. It is designed for derivation from a short segment of voltage curves and since the segment can begin at any time spot, the VDTTI is easy to extract from batteries operating at different voltage ranges. In addition to constant-current (CC) discharge mode, the VDTTI can be extracted in randomised discharge mode, thus enabling the employed data-driven method to obtain SOH estimates of LIBs that often switch between the two modes. Leveraging the subset of ML, the DL algorithm known as long short-term memory (LSTM) is used to estimate SOH with the extracted VDTTI. It is highly precise in capturing the capacity regeneration trends of the LIB due to the prioritised learning of capacity data.

3) Most of the existing data-driven approaches have been designed for conditions of CC charging/discharging at a specific rate over a long duration. Yet, the loading profiles of batteries can be highly volatile, which restricts the application of existing data-driven methods. Hence, by integrating a novel momentary HI with hierarchical ensemble machine learning, it is shown that the SOH can be efficiently estimated under dynamic discharging and varied SOC levels. The HI, named the electrical transient during short time interval (ETSTI), is extracted from the battery voltage and current profiles during the transition between discharging and rest (< 0.1 s). A hierarchical ensemble model (HEM) of four popular ML algorithms, namely the deep neural network (DNN), extreme learning machine (ELM), Gaussian process regression (GPR), and support vector regression (SVR), is designed for SOH estimation using the ETSTI as the input. The rationale behind this innovation is to: (i) exploit the complementary strengths of the different algorithm via a dual-level training process. (ii) Diversify and optimise the learning of model weights with only a limited number of ML algorithms. (iii) Attain an estimation accuracy that surpasses both single-model and traditional ensemble model frameworks, with far greater computation savings. The proposed method exhibits superior real-time capability in a BMS microcontroller when verified against various LIBs, HIs and SOH estimation models.
4) It is often laborious and computationally costly to robustly train and implement one ML model for different LIB chemistries across varied operations of the battery. In light of this issue, coupled with the recent technological breakthrough of large language models (LLMs), the proposed research exploits the strong generalisation capability of the generative pre-trained transformer-4 (GPT-4) for SOH estimation; which is the first-ever attempt in the literature of data-driven battery health prognostics. Since battery data usually arrives sequentially with varied distribution in the real world, the teacher-to-student model-based distillation of knowledge and lifelong learning (LL) are incorporated into GPT-4 to estimate SOH adaptively with minimal fine-tuning. Testing results of this proposed novel method on a BMS microcontroller show a very high estimation accuracy at low computational cost.

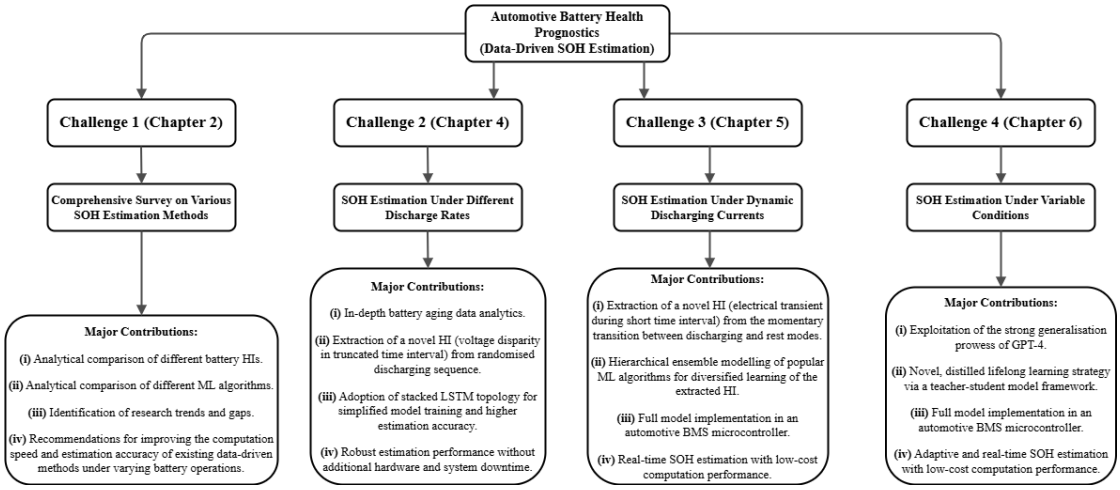

Figure 1.8. An overview of the challenges identified by this thesis, as well as the major contributions made to address these challenges.

1.4 Organisation of the Thesis

This thesis is organised into seven chapters as follows:

Chapter 1 introduces the research background, motivations, objectives, and major contributions of this thesis.

Chapter 2 provides a comprehensive literature review of the existing SOH estimation methods with emphasis on data-driven approaches, including battery HIs. Furthermore, the associated algorithms that could potentially improve the synergistic efficacy of these methods in EV applications are jointly analysed and discussed.

Chapter 3 introduces the battery aging datasets that are employed to verify the efficacy of the SOH estimation methods proposed in this thesis. Herein, four datasets created by research groups from the National Aeronautics and Space Administration (NASA), University of Michigan, and Infineon Technologies, are described in detail. These datasets contain EV application-oriented load profiles derived from three widely used LIB chemistries and are therefore suitable for accurate benchmarking of the estimation methods' performance.

Chapter 4 presents the SOH estimation method based on the VDTTI and LSTM. The VDTTI can be extracted during either CC discharging or randomised discharging, and is obtainable through a short segment of discharging voltage curves. Unlike most of the existing HIs, the VDTTI can be easily extracted from

various voltage ranges, thus making it highly flexible for application. Since the VDTTI is both a singular and truncated feature, it does not need to be pre-processed with a filter. The LSTM is trained to learn the mapping relationship between the extracted VDTTI and practical SOH of the LIB. The proposed method is tested using the NASA (random walk) dataset and benchmarked against four widely used data-driven methods.

Chapter 5 presents the SOH estimation method based on the ETSTI and HEM. The ETSTI is extracted from a very short period (< 0.1 s) when the battery momentarily transits from discharging to rest, considering that most of the existing data-driven models are designed for a lengthy CC charging/discharging process without accounting for the volatility of an EV's regenerative braking. The highly truncated nature of this HI also makes it exceptionally easy to implement under various discharging currents and SOC levels, whilst removing the need for filtering. The rationality of the ETSTI is to indirectly reflect battery internal ohmic resistance, which is justified by theoretical analysis with an ECM. Then, the HEM comprising of renowned ML algorithms is designed to efficiently learn the relationship between ETSTI and SOH through momentary informatics. The proposed method is experimentally verified using two aging datasets and benchmarked against a wide variety of HIs and SOH estimation models.

Chapter 6 presents the SOH estimation method based on GPT-4 and distilled lifelong learning (DLL). The HI is extracted from partial charging voltage curves which are associated with the incomplete charging of an EV in real-world application. Then, the language-based perceptivity of the GPT-4 is converted to LIB data-based by only retraining its input and adaptors on the extracted HI based on selected LIB labels (vectorised text specifications). DLL is applied to enable robustness against data shifts and noise as it continuously updates the GPT model and retains vital knowledge. The proposed method is experimentally verified using three unseen LIBs that are of different chemistry and benchmarked against six popular data-driven methods.

Chapter 7 concludes this thesis and highlights future works including enabling pack-level, data-driven SOH estimation considering inconsistencies in battery operations, and the integration of cloud-edge technology with LLMs for SOH estimation.

Chapter 2

Literature Review

This chapter provides a critical survey of the existing works on battery SOH estimation, with a primary focus on data-driven approaches which include the extraction and practical application of HIs. Importantly, an analytical assessment of these methods is performed to determine their feasibility for on-board deployment in automotive BMSs.

2.1 SOH Estimation Methods

A myriad of approaches have been proposed for battery SOH estimation, as summarised in Figure 2.1. Generally, these approaches can be classified into four categories: 1) direct methods, 2) model-based methods, 3) adaptive filter methods, and 4) data-driven methods.

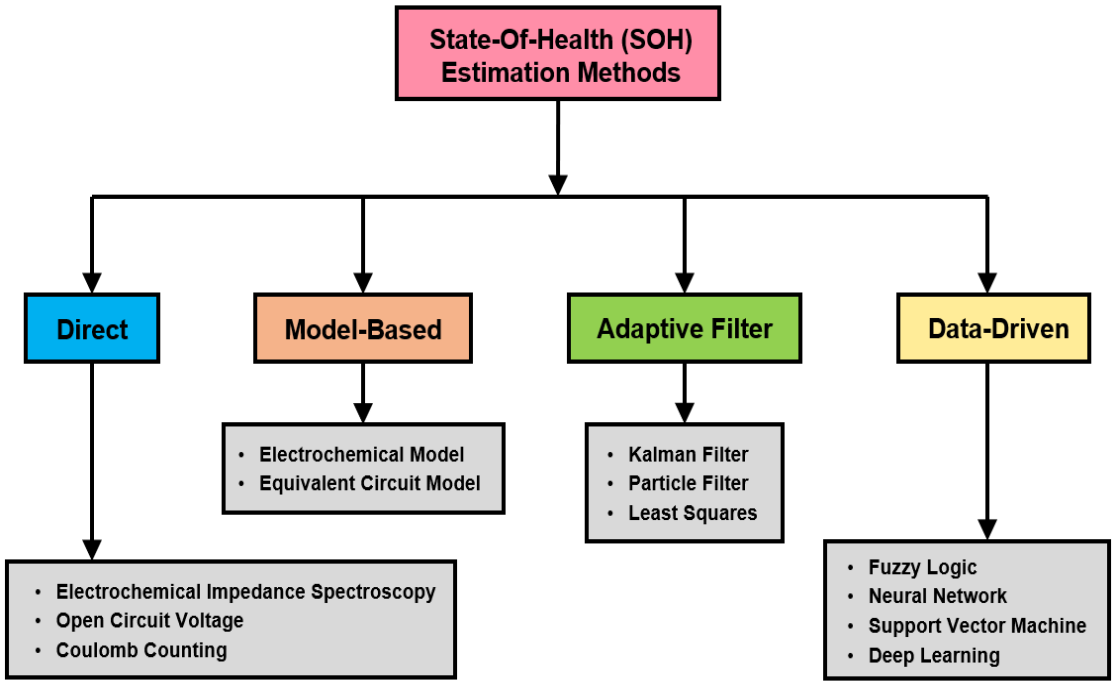

Figure 2.1. An overview of different SOH estimation methods [3].

2.1.1 Direct Methods

Direct methods are simple, but they can only work offline and require additional hardware equipment that are oftentimes bulky, which makes them generally

unsuitable for implementation in mobile energy storage systems (ESSs) such as EVs. The electrochemical impedance spectroscopy (EIS) method is used to measure a battery's impedance over a range of frequencies ranging from 50 mHz to 10 kHz. It applies a small alternating current (AC) signal to the battery and measures the corresponding voltage response. By studying the impedance spectrum [23], insights can be gained into various electrochemical processes, such as charge transfer resistance, diffusion, and double-layer capacitance. This allows the SOH to be monitored in various battery chemistries.

The open-circuit voltage (OCV) [24] can be a rapid indicator of SOH since it directly reflects the SOC level. It is measured when the battery is either disconnected from the load or immediately after its resting period, so as to allow the voltage transients to be stabilised. However, in contrast to EIS, this method provides less information on the internal degradation of the battery. The coulomb counting method tracks the charging/discharging cycles of a battery through the integration of current over time, as described by Eq. (2.1):

$$\mathrm{SOC} = \mathrm{SOC}\,(t_0) + \frac{1}{C_{\mathrm{nom}}} \int_{t_0}^{t_0+\tau} I_{\mathrm{batt}} \tag{2.1}$$

where C_{nom} is the nominal battery capacity and I_{batt} is the battery current. Herein, the charge quantity entering and exiting the battery is calculated, enabling the remaining capacity and SOC to be approximated and, by extension, the resultant SOH. While coulomb counting [25] is the most used method in commercial ESSs due to its ability to provide continuous updates on the battery status, it is prone to cumulative measurement errors over time; which can lead to large deviations in the estimated SOH values.

2.1.2 Model-Based Methods

Model-based methods involve the use of mathematical models to demonstrate the time-varying behaviour and traits of a battery. They simulate the internal working principles of the battery, such as temperature effects, charge/discharge cycles, and aging mechanisms. The electrochemical model is based on the fundamental electrochemistry principles governing battery operation. It involves complex mathematical modelling of the intrinsic reactions [8] occurring within the battery, which include solid-phase ion transportation, Butler-Volmer charge

transfer dynamics, and thermodynamic properties (e.g., law of Arrhenius). The model usually employs parameters such as potential, concentration, and current density to simulate the battery's behaviour under various operating conditions. While electrochemical models such as the single-particle model (SPM) [26] and pseudo two-dimensional (P2D) model [27] have been popularly used for accurate adaption to different battery chemistries and configurations, they are both mathematically and computationally demanding. This makes them difficult to implement in real-time embedded BMSs for efficient SOH estimation.

Unlike the electrochemical model which performs complex simulation of battery's internal degradation physics, the equivalent circuit model (ECM) simply captures the battery's behaviour through an electrical circuit comprised of voltage sources and resistor-capacitor (RC) networks. These circuit elements mimic the battery's impedance variance in response to inputs such as voltage and current, by considering both dynamic and polarisation characteristics. The most popular ECM used in EVs is the first-order Thevenin model [28] due to its balance between simplicity, computational efficiency, and reasonable accuracy in SOH estimation. Figure 2.2 illustrates the schematic diagram of the first-order Thevenin model. Herein, V_{OCV} and V_T represent the OCV and terminal voltage, respectively. C_1 represents the polarisation capacitance, while R_0 and R_1 respectively denote the internal ohmic resistance and polarisation resistance.

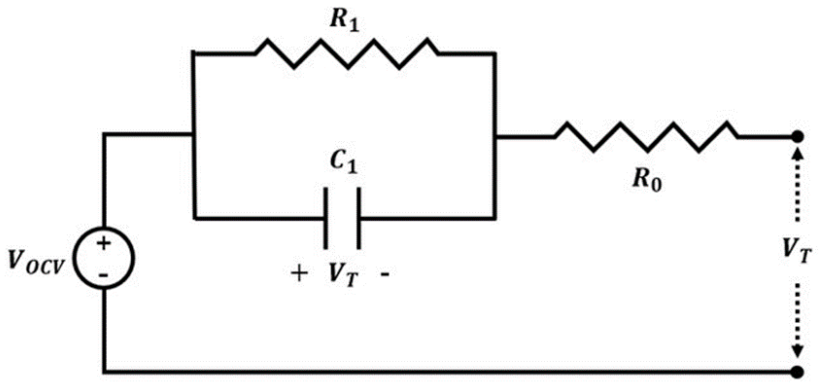

Figure 2.2. Schematic diagram of the first-order Thevenin model [28].

Based on the Thevenin model and OCV tests, the recursive least squares (RLS) algorithm is applied in [29] to parameterise the model. The identified internal ohmic resistance and polarised resistance are then used to denote SOH on the basis of battery capacity fade. In [30], the CC charging profiles at various

degradation stages of the LIB are used to fit the Thevenin model and the SOH is computed with the model parameters. A joint-state estimator is proposed in [31] by integrating the Thevenin model with two extended Kalman filters (EKFs) that incorporate time-varying scales for real-time SOC estimation and offline SOH estimation, respectively. Additional RC components have been included to establish second and third-order Thevenin models [32], [33] for more precise LIB simulations, but this raises the computational burden significantly due to greater model complexity.

2.1.3 Adaptive Filter Methods

Adaptive filter methods are mathematical functions which update their parameters in real-time based on changes in the battery's operating conditions, such as charge/discharge cycles, load and temperature. Such adaptability allows for more accurate tracking of the SOH over time. Furthermore, adaptive filters can effectively reduce noise in the measured battery voltage, current and temperature signals, which is crucial for precise SOH estimation. By filtering out irrelevant data, they improve the quality of the input signal for the SOH estimator.

In [34], an ensemble of polynomial and exponential models is proposed to track the degradation trend of the LIB capacity. Then, the particle filter (PF) technique is applied to continuously update the model coefficients and perform online SOH estimation. A hybrid ECM that combines the unscented Kalman filter (UKF) with RLS is proposed in [35] for SOH estimation. Firstly, the model parameters are identified by RLS. Secondly, UKF is used to evaluate the ohmic resistance and SOC status of the battery. Lastly, testing results show that the proposed UKF-RLS algorithm offers greater computation efficiency and SOH estimation accuracy when compared to the classic KF algorithm. In [36], a backpropagation dual-EKF method for SOC and SOH co-estimation of LIBs based on the least squares (LS) algorithm is proposed. It is designed to augment the precision of online parameter identification. Taking into account the coupling effect between SOC and SOH, the co-estimation technique is realised through the dual-EKF by using ampere-hour integral as the bridge, which boosts the convergence speed and accuracy of the estimation results. The backpropagation NN is incorporated

to rectify the estimation errors accumulated by the EKF algorithm.

Considering the above-discussed trends and methods [34]–[36] for adaptive filter-based SOH estimation, it is discovered that they all share several common drawbacks in EV applications. Firstly, adaptive filter methods can be computationally costly, potentially leading to increased processing time and power consumption, which is critical in automotive BMSs. Secondly, the performance of adaptive filters can be susceptible to convergence issues, especially during dynamic discharging of the battery (i.e., regenerative braking), since the battery characteristics are changing rapidly. Lastly, the operations of these methods are largely dependent on initial driving cycle conditions, which may not always be optimal.

2.1.4 Data-Driven Methods

An approach for battery SOH estimation involves two vital components: (i) the extracted HIs, and (ii) the methods employed to fit the HIs with the SOH. Of which, the data-driven method has gained the most traction, due to recent advancements in computing hardware and ML algorithms. In a data-driven approach, a large volume of battery parameters such as voltage, current and temperature, are collected from LIBs (via accelerated aging experiments) by continuously recording the health condition of the LIBs until failure is reached; hence acquiring aging datasets which are then used to train an ML model for online SOH estimation.

An ML model converts input data into decisive outputs; often described as a black box process which learns from exposure to known samples of inputs and outputs. The extracted or processed features (e.g., HIs) are typically used as inputs and output a battery capacity-based degradation curve, such as SOH. An ML model can be described by Eq. (2.2), where $f^{(h)}$ denotes the function of the h-th layer of an NN, $h = 1, 2, \ldots m$.

$$f_\theta(x) = f^{(m)}(\ldots f^{(2)}(f^{(1)}(x))) \tag{2.2}$$

Eq. (2.3) describes the model's training process, which minimises the disparity between the prediction $f_\theta(x)$ and the ground truth label y,

$$\min_\theta L_f(f_\theta(x), y) \tag{2.3}$$

while $L(\cdot,\cdot)$ is the pre-defined loss function of the model $f_\theta(\cdot)$. NNs in general can solve such backpropagation process, using gradient descent algorithms to update the model parameters as follows:

$$\theta_{i+1} = \theta_i - \eta \cdot \nabla_\theta L_f(f_\theta(x), y) \tag{2.4}$$

where η is the learning rate, i denotes the i-th iteration step, and θ_i denotes the model parameters [10]. Once the training sample x and label y are known, a precise ML model can be obtained by various NN training algorithms. In the literature, fuzzy logic (FL), NN, SVM, and DL are the classical data-driven methods that are used for SOH estimation [37], [38].

FL typically engages a fuzzy rule set to process the measured data of complex and non-linear systems, based on the data's segregation into crisp and fuzzy sets. The crisp set splits the data with certain values, whereas the fuzzy set classifies the data with uncertainty. Each member of the fuzzy set belongs to a membership function (MF), and an accurate SOH prediction is mainly dependent on proper selection of the MF. Two exponential MFs are employed in [39] to compute the SOH's correlative HI index as described by Eq. (2.5):

$$y_{fit} = a_0 + a_1 e^{-\left(\frac{x}{\alpha_1}\right)^{\beta_1}} + a_2 e^{-\left(\frac{x}{\alpha_2}\right)^{\beta_2}} \tag{2.5}$$

where x represents the number of cycles and y represents the normalised capacity value. Through FL algorithm, the fit function is estimated, which firstly computes the HI index using a fitting curve with an error between 5% and 10%. The NN is then engaged to evaluate the HI index to reduce the error to below 5%. An online SOH estimation scheme involving FL is proposed in [40] to determine suitable HI coefficients for both internal resistance and battery capacity measurements in the BMS. Based on the measured battery current and temperature, the coefficients associated with SOH are extracted by the FL algorithm. An improved yet similar scheme is proposed in [41] to predict the SOH using FL with battery voltage, current, temperature and time as coefficients to compute internal resistance and maximum capacity; which in turn facilitates online SOH estimation. Even though FL is a rather robust data-driven approach, it requires significantly large sets of test data and a powerful computing system; which are impractical in real-world EV usage scenarios. Moreover, the improper

assumptions considered in fuzzy rules constitute numerous errors that are usually added to the final SOH result.

The NN is a renowned approach that is capable of processing vast amounts of data across complex and non-linear systems, without requiring intricate battery characteristics information (e.g., electrochemical reactions) to estimate the SOH. NN algorithms also require lesser data than FL algorithms. To enable accuracy, the collected LIB experimental data are repetitively processed by a training algorithm until the lowest possible estimation error is obtained. The NN structure is also sufficiently robust for estimating the SOH accurately during variegated LIB operating conditions. The NN's neuron activation function [42] used for modelling the electrochemical properties of a battery is depicted as:

$$\begin{aligned} &\phi_i(r_k) == G(\|r_k - t_i\|) \\ &= \exp\left(-\frac{\| r_k - t_i|^2}{\sigma_i^2}\right), i = 1 \ldots\ldots M \end{aligned} \tag{2.6}$$

such that the input vector of the NN is expressed by $r_k = [V_k I_k SOC_k]^T$, where V_k, I_k, SOC_k denotes the voltage, current and SOC at the sampling time k. The standard deviation is denoted by σ_i, while the number of neurons in the hidden layer is denoted by M. Using the acquired voltage-capacity slopes, the battery SOH is computed. The NN's prediction accuracy can be further enhanced by employing additional training data such as temperature.

Using HPPC tests to extract battery parameters from a first-order ECM, an NN variant named extreme learning machine (ELM) is conceptualised in [43] to calculate the maximum available capacity to denote battery SOH. In [44], an NN-integrated, Gaussian process regression (GPR) model is built to determine SOH based on CC-CV recharging and CC discharging of 110 LIBs. This method considers OCV, instantaneous voltage drop, and current charging time as the key battery parameters for estimating SOH. A polynomial NN is developed in [45] using data grouping to derive the relationship between SOH and the differential geometric traits of battery terminal voltage curves. In [46], a multi-layer perceptron (MLP) based NN is developed to estimate the SOH of an LIB in EV application; by firstly extracting its parameters using ECM. To attain greater estimation accuracy, this method considers the data collected from

discrete LIB life span. It is observed that the drawbacks of the NN are its high computational cost as well as its need for diversified training data [43]–[46].

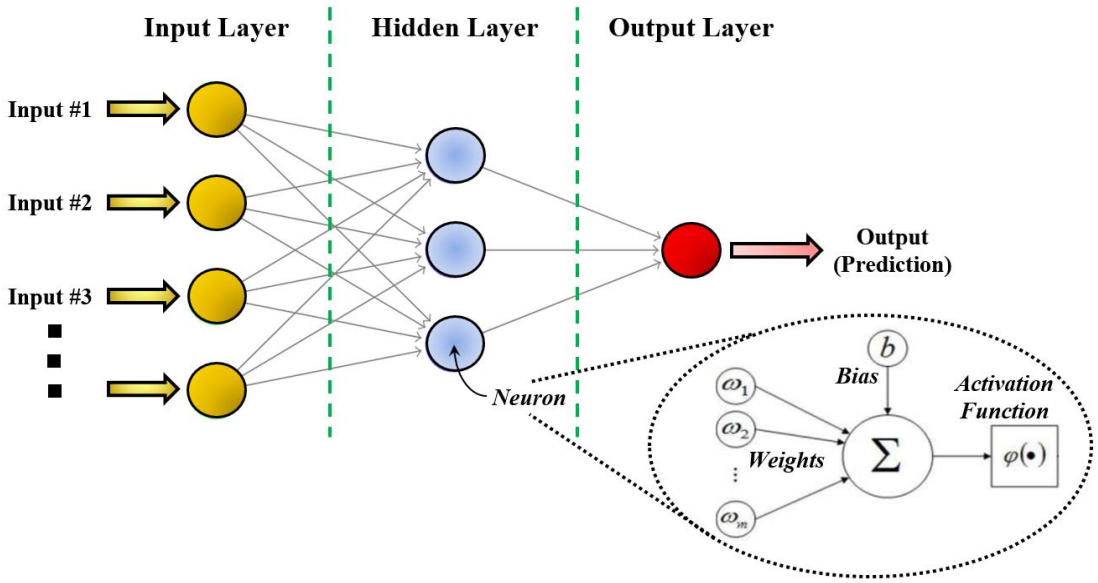

Figure 2.3. The general structure of a neural network (NN) [45].

SVM is commonly employed to solve problems involving classification and regression. It strives to establish hyperplanes in high dimensional space to separate data based on their distinctive class. When the distance from the hyperplane to the nearest data point of any class is maximised, it is evident that an optimal separation boundary is attained. Notably, SVM is a representative kernel-based supervised learning algorithm which can perform data analysis and capture patterns in non-linear systems. It employs a regression algorithm to solve problems involving data that are not linearly separable, and hence suitable for performing SOH prediction of LIBs.

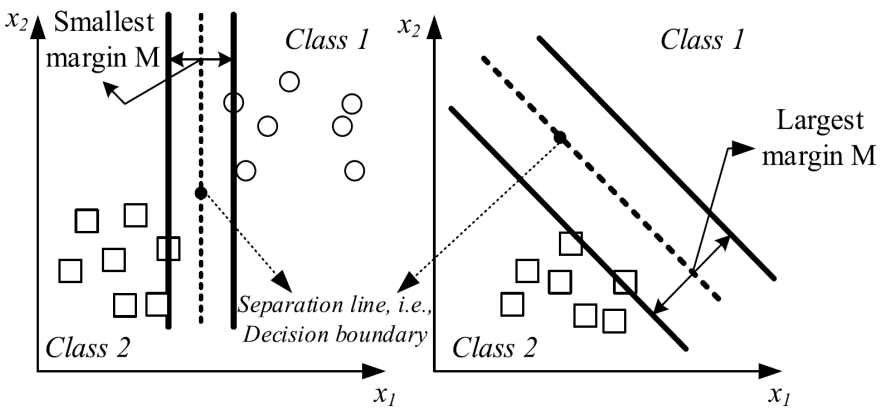

Figure 2.4. Construction of SVM hyperplane(s) for data class separation [38].

Battery state estimation often requires a regression learning method to minimise the error function in a sequential manner. Henceforth, it is appropriate to consider employing a generalised regression variant of the SVM, known as support vector regression (SVR). It is worth noting that while the SVR shares several similarities with radial basis function (RBF) methods [47], a key difference is the SVR aims to utilise simplified optimisation routines for parameter fitting, such as quadratic programming with linear constraints. In addition, the notion of error tolerance margin is engaged, whereby no cost function penalty will be applied to the fitting error if it is found to be within a specified error band; thus stabilising the estimation.

In [48], an SVR incorporating training and testing data is used to estimate the SOH in dynamic conditions pertaining to both the load and environment. Initially, vast quantities of LIB data are collected via lab-based, direct measurements at varying degrees of battery aging. Validation is then performed using automotive homologation drive cycles at different temperatures, which indicated adequate accuracy in LIB health diagnostics. The work in [49] proposed using partial charging voltage and the current of the LIB to extract three feature vectors, or HIs; namely energy signal, charge duration and ampere-hour throughput. Then, SVR with RBF is applied on these inputs to estimate SOH. The acquired results show that the proposed method can estimate the SOH online effectively with less than 5% error. A major drawback of the SVM/SVR is its need for large quantities of data to enable accuracy enhancements and fine-tuning of the required battery parameters, which is a highly time-consuming procedure.

DL is built upon the concept of NNs, and essentially an improved version of the MLP with the ability to overcome the limitations of ML [50]. Furthermore, it can adopt either supervised learning or unsupervised learning approach. The objective of DL is to form a connection between the input and target parameters by non-linear functions, whilst utilising specific methods to compute the function parameters. The term “deep” in DL signifies multiple computational layers in the NN, and there is a general consensus whereby any NN containing more than one hidden layer is considered to be a deep neural network (DNN) [51]. Notable DNNs include convolutional neural network (CNN) [52] and recurrent neural network (RNN) [53], as well as RNN variants; namely the gated recurrent unit

(GRU) [54] and LSTM [55]. While the CNN is mainly suitable for image recognition and computer vision applications, the RNN is proficient in addressing time-series related problems and facilitating forecasting operations. The standard NN, also known as the single hidden layer feedforward neural network (SLFNN), can be described by Eq. (2.7), where x denotes the input sample, $f(x)$ denotes the SLFNN output, f_a denotes the activation function, w is the weight, and b is the bias. Contrastingly, the DNN can be described by Eq. (2.8). Both SLFNN and DNN are mostly trained using backpropagation [36]; an optimisation algorithm involving gradient descent to optimise the weights and biases in the NN.

$$y = f(x) = f_{\mathrm{a}}(w_0^T f_a(w_0^T x + b_0) + b_1) \tag{2.7}$$

$$f(x) = f_a\left(w_i^T f_a\left(w_{i-1}^T \ldots f_a(w_0^T x + b_0)\right) + b_i\right) \tag{2.8}$$

A DNN is proposed in [56] to estimate SOH using a dropout algorithm that trains the model by randomly dropping neurons at a fixed probability of 0.25. Another work [57] suggested thinning the weights of the DNN instead in order to minimise overfitting, therefore enhancing the DNN's performance. Subsequent comparisons between different methods have shown that the DNN possesses superior SOH estimation accuracy due to its mean root-mean-square error (RMSE) of 3.43%. This mean RMSE is lower than that of the logistic regression (4.56%), *k*-nearest neighbour (5.6%), SLFNN (4.61%), and SVR (4.55%).

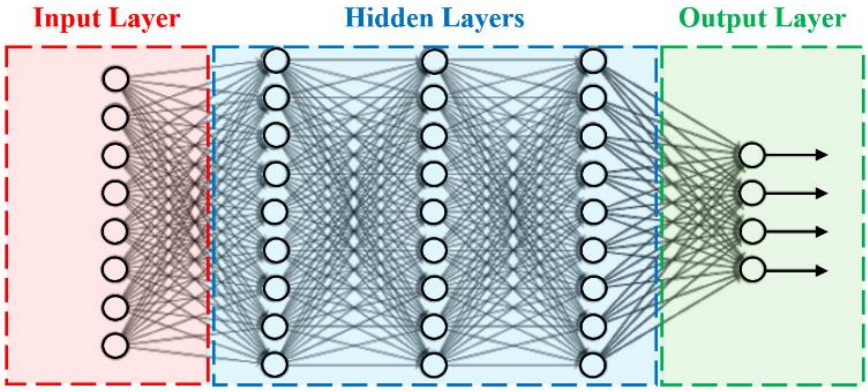

Figure 2.5. A classic example of a deep neural network (DNN) [56].

It is worth noting that even though the non-DNN based ML methods can effectively capture the vital features of a non-linear system, they are generally ineffective towards a time-series based system. Any data collected during a

single discharge cycle of an LIB at a specific time spot is usually unsuitable for online SOH estimation. However, the time-series data acquired from a specific time interval can accurately capture the aging effect of the LIB. Henceforth, any method employed to estimate SOH must be able to handle time-series data effectively for improved prognostics performance in automotive BMSs. One such proven method other than the DNN is the RNN and its variants.

2.2 Indirect Health Indicators

Battery aging is caused by various factors such as the depth of discharge, temperature, and charge/discharge rates. Correspondingly, the performance degradation of LIBs is reflected in the variation characteristics of voltage, current and temperature; which can be used for online SOH estimation when measured by BMS sensors. As the measured data is large and sampled at a non-uniform rate, it is difficult to process them as a whole. Thus, instead of using all the data in the voltage, current and temperature curves, it is more practical to extract indirect HIs from these curves. The major advantage of indirect HIs is the fact that they can be measured online and in real-time, which makes them vital input features that can boost the prediction accuracy of an ML model if appropriately extracted. The working principle [3] of LIBs is generally organised in three stages: 1) constant-current (CC) charging, 2) constant-voltage (CV) charging, and 3) constant-current (CC) discharging. Henceforth, apart from rest mode, it is apparent that the performance of LIBs can be determined by the indirect HIs extracted from either charge mode or discharge mode.

2.2.1 Constant Charge Time

An EV battery's charging profile can be regulated by the BMS throughout the battery lifetime, allowing easier SOH estimation under charge mode. A model-based approach is presented in [58] to estimate SOH using a voltage curve extracted from CC charging stage at variegated life cycles. To exhibit capacity degradation, the constant-current charge time (CCCT) [59] and constant-voltage charge time (CVCT) [60] are respectively extracted as HIs. In tandem with the RNN, the time spots of equispaced charging voltage curve (TSECVC) [61] are employed to estimate the SOH of an LIB in CC operation. The LIB is

charged at CC over 5-second intervals for the TSECVC to be extracted as a HI. The extraction scheme of the aforementioned HIs [58]–[61] is exemplified in Figure 2.6, where $t_{V_{max}}$ and $t_{V_{min}}$ are the required time to charge the LIB to the voltage levels of V_{max} and V_{min}, respectively, in the CC charging stage. The chosen terminal voltage intervals are V_{max} and V_{min}.

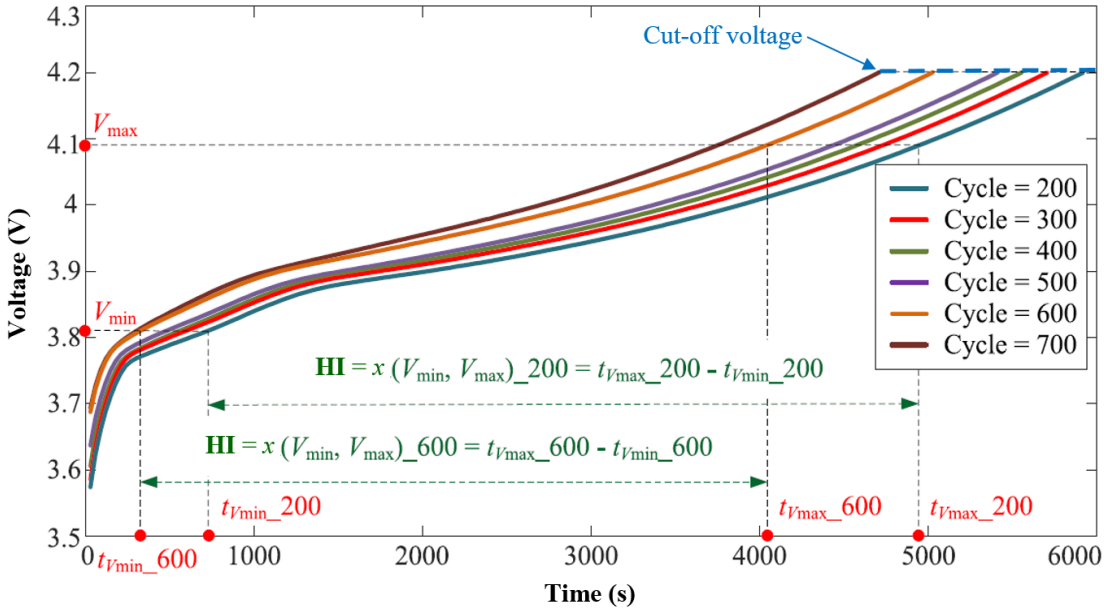

Figure 2.6. HI extraction based on the charging voltage curves of different battery aging cycles [58]–[61].

In explicit mathematical terms, CCCT and CVCT can be expressed using Eq. (2.9) and Eq. (2.10), respectively. With regards to Eq. (2.9), $t_{I_{max}}$ and $t_{I_{min}}$ are the required time to charge the LIB to the voltage levels of V_{max} and V_{min} when employing I_{max} and I_{min};

$$\mathrm{CCCT} = t_{I_{max}} - t_{I_{min}} \tag{2.9}$$

$$\mathrm{CVCT} = t_{V_{max}} - t_{V_{min}} \tag{2.10}$$

It is worth noting that CCCT and CVCT can only be applied if the LIB is charging at CC stage, from low-to-high cut-off voltage, or at CV stage until the current dips to its threshold. Contrastingly, the TSECVC can be extracted from a partial charge process and hence desirable accuracy is attainable with a mere 10 s interval of galvanostatic charge [13], which affirms the simplicity of this HI. The key limitation [11] of the TSECVC is its high sensitivity to the pre-defined starting

voltage required for its extraction, since it will affect its correlativeness to SOH.

2.2.2 Incremental Capacity and Differential Voltage

HI extraction schemes involving the incremental capacity analysis (ICA) [62] and the differential voltage analysis (DVA) [63] of the charging curve are also commonly engaged for SOH estimation. Specifically, ICA and DVA constructs the IC and DV curves, which denote the innate correlation between OCV and dQ/dV, as well as OCV and dV/dQ. The respective peaks on the IC and DV curves can be used to derive vital information on SOH and are therefore feasible HIs. Notably, the voltage peaks of the IC curve are strong indicators of capacity fade. The mathematical expression of IC is described as the battery capacity Q (in ampere-hour, or Ah) differentiated with respect to the voltage V:

$$IC = \frac{dQ}{dV} \approx \frac{\Delta Q}{\Delta V} \tag{2.11}$$

where the voltage change ΔV is chosen ($\Delta V \approx$ 40 mV) by considering the following two factors without compromising either of both: (i) the prominence of the peaks and valleys, and (ii) the ability to repress voltage distortions caused by random current changes due to the EV charger. Q is simply interpreted as the integration of the charging current I during charge mode:

$$Q = \frac{1}{3600} \int I dt \tag{2.12}$$

ICA calculates the derivatives of the charged capacity in respect of OCV but due to the differential process, any minuscule measurement error by the BMS may cause overly unacceptable SOH estimation results. Moreover, the LIB must operate within a specific range of ΔV or SOC that encloses the peaks found on the IC curve. Charging the LIB with near-negligible current is an impractical solution and hence selecting a charging rate of either 0.4 C or 0.5 C is a good compromise between the charging time and the distorting voltage drop across the EV's resistive components (e.g., cables, relays and battery impedance). In contrast to Eq. (2.11), the DV curve is calculated as follows:

$$DV = \frac{dV}{dQ} \approx \frac{\Delta V}{\Delta Q} \tag{2.13}$$

Assuming V and I are sampled by the BMS at an interval of 1 s, the DV in

discrete form can be described using Eq. (2.14), which denotes the DV value at time step $k+1$, while $V|_{t=k}$ and $V|_{t=k+1}$ are the voltage values measured at time step k and $k+1$, respectively.

$$\left.\frac{dV}{dQ}\right|_{t=k+1} \approx \frac{V|_{t=k+1} - V|_{t=k}}{I(t_{k+1} - t_k)} \tag{2.14}$$

Even though both ICA and DVA are well capable of linking the results between electrical monitoring and internal reaction mechanism of the LIB, it is observed that the DVA possesses two distinct advantages over the ICA; (i) the DV exhibits linear behaviour across time and reflects uniformity of the LIB's lithium distribution. (ii) Since the numerator of the DV calculation formula is voltage, its precision is less affected by the BMS's voltage sensor performance as compared to IC. A shared limitation in this class of differential signals, namely ICA and DVA, is that for any signal to infer numerical SOH estimates, it requires extensive manipulation using highly complex, regression-based algorithms.

2.2.3 Sample Entropy

As opposed to charge mode, the discharge mode of an EV battery is sensitive to variable conditions such as the load usage profile, since it is less controllable. It is therefore more complicated to analyse and extract HIs from the discharging curve due to its volatility. Resultantly, most of the existing HIs have been developed on the assumption that the LIB discharges at CC, regardless of its application and degradation stage. Through prior experiments that indicate a discharging curve progressively distorts with prolonged LIB usage, Ref. [64] suggests applying the sample entropy of discharge voltage curve as a HI to denote non-linear battery aging. Sample entropy essentially determines the time-series complexity by measuring the probability of new patterns being generated in the voltage signal. The higher the probability of a new pattern arising, the higher the complexity of the time-series data sequence. Sample entropy can be computed as follows:

$$\text{SampEn}\,(m, r) = \lim_{N\to\infty} -\ln\left[\frac{A^m(r)}{B^m(r)}\right] \tag{2.15}$$

where $B^m(r)$ denotes the probability that two sequences will match for m points with a tolerance of r, while $A^m(r)$ is the probability that two sequences will match

for $m+1$ points. Due to the desirable consistency demonstrated by sample entropy, the values of m and r share certain attributes in respect of their effect on sample entropy. Typically, m is pre-set to a value of 1 or 2, while r is fixed at 0.1. When N is a pre-defined finite number, Eq. (2.15) can be re-formulated as:

$$\text{SampEn}\,(m,r,N) = -\ln\left[\frac{A^m(r)}{B^m(r)}\right] \tag{2.16}$$

In the sample entropy of discharging voltage, the battery current and temperature are not assimilated. Hence, these two parameters can be utilised in sparse scenarios where a reference full discharge is performed [65]. It is worth noting that in the domain of signal processing, sample entropy outperforms both the ICA and DVA, because firstly its calculation is independent from the data length; and secondly, it has greater consistency. Principally, a lower sample entropy value equates to a higher sequence of self-similarity. Whereas for a higher sample entropy value, the sample sequence is more complex. A LIB's internal complexity usually varies in accordance with the battery aging process. Therefore, the sample entropy of the voltage sequence is potentially an effective HI that is correlated to battery SOH.

By engaging both the discharging voltage and current curves, a fractional-order modelling approach is developed in [66] to facilitate the co-estimation of SOC and SOH online. A similar work [67] collectively extracted several sample entropies of both voltage and current as HIs, so as to index the remaining battery capacity with a relevance vector machine model. Since voltage and current are often used for approximating battery SOH, the HIs derived from them are likely to be analogous with the electrical load profiles of EVs. However, it is discovered that the aggregated noise and weights of multiple input predictors (e.g., multiple HIs) could de-stabilise an ML model's prediction performance [66], [67].

2.2.4 Timed Voltage Variance

The time interval of equal discharging voltage variance (TIEDVV) is extracted as a HI in [68] to denote capacity degradation. A similar procedure in [69] extracted the TIEDVV's variant, named the voltage decline during equal discharge time (VDEDT), to determine SOH. These procedures [68], [69] simply consider the online monitoring parameters of the LIB, namely discharging

voltage and time interval, to extract either TIEDVV or VDEDT. Figure 2.7 depicts the extraction scheme of the TIEDVV and VDEDT. Herein, TIEDVV is categorised by Δt_V, which is extracted in correspondence to the pre-defined V_{max} and V_{min} (i.e., the health-indicating voltage signals); whereas VDEDT is categorised by ΔV, which is extracted in correspondence to the pre-defined $t_{V_{max}}$ and $t_{V_{min}}$ (i.e., the health-indicating time spots). The discharging voltage variance in a certain equal-length time interval at the i-th cycle is computed as,

$$V_{i,\,\mathrm{VDEDT}} = V_{t_{min}} - V_{t_{max}},\ i = 1, 2, \ldots, n \tag{2.17}$$

and the raw VDEDT series can be expressed as:

$$V_{\mathrm{VDEDT}} = \left\{V_{1,\,\mathrm{VDEDT}}, V_{2,\,\mathrm{VDEDT}}, \ldots, V_{n,\,\mathrm{VDEDT}}\right\} \tag{2.18}$$

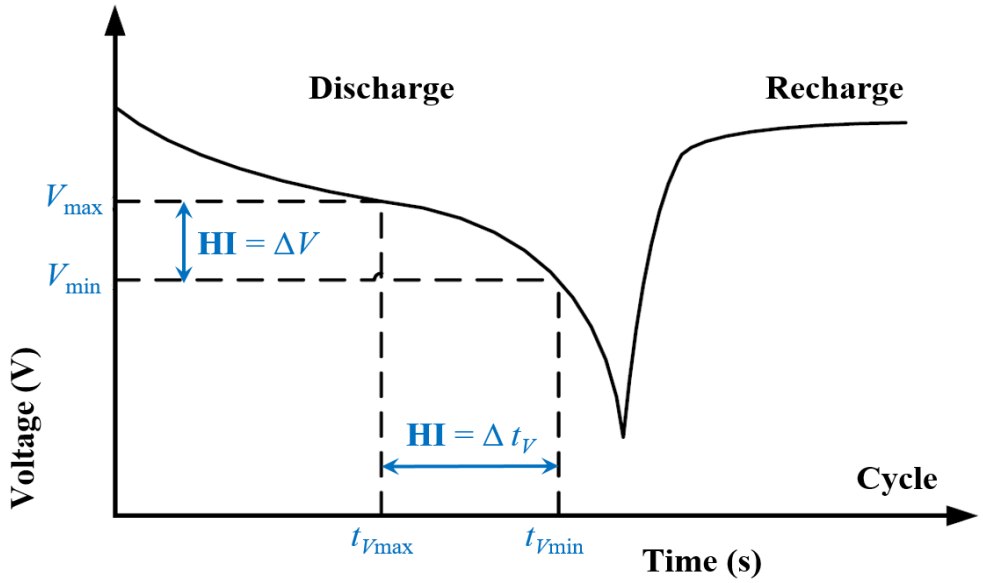

Figure 2.7. HI extraction based on the timed voltage variance of a single discharge cycle [68], [69].

The advantage of TIEDVV and VDEDT over sample entropy is that these two HIs only require the partial discharge curve for their extraction. The range of time interval and discharge voltage difference are pre-determined, which are subjective to both the user's requirement and the available data collected by the BMS sensors. However, it is discovered that these two HIs disregard both discharge current and temperature, and only consider the change in voltage. Their application scenarios are henceforth constrained since the TIEDVV and VDEDT only work properly when the operating load profile relates to the offline

training of the ML model. It is also worth noting that if there is no mutual, standardised interval identified for the discharging voltage, it would be difficult to extract the TIEDVV and VDEDT series across various LIB discharge cycles. Although strongly correlated to SOH, many of the cutting-edge HIs, such as the discharging voltage difference of equal time interval (DVDETI) proposed in [70], can only be extracted from a CC discharging process of over 500 seconds under a fixed current. An improved variant of the DVDETI, named the voltage variance during equal time interval (VVETI) [71], can be extracted from a shorter time interval (300 seconds) but still relies on CC condition and the current is fixed.

2.2.5 Fusion-Based Indicator

In order to denote battery capacity, Ref. [72] proposed to extract ten HIs and fuse them together. The extraction involves four HIs from the CC discharge curve, four HIs from the CC charge curve, and two HIs from the CV charge curve. Then, grey relational analysis is performed and indicated a similarity index greater than 0.5 between the battery capacity and the individual HIs, proving that each HI is a fairly accurate representation of capacity. A singular, fused HI is subsequently generated through kernel principal components analysis (KPCA) and is found to possess an even higher similarity index, i.e., 0.8. The fused HI's advantage over the segregated HIs [58]–[71] is its flexible extraction during CC-CV charging and CC discharging. The designated non-linear mapping function is $\Phi : R^M \rightarrow F$, which maps the input HI space X_k, $(k = 1, 2, \dots, M)$ to the feature space $F : \Phi(X_k)$, $(k = 1, 2, \dots, M)$. KPCA is performed within the boundary of the feature space F as follows:

$$C^F = \frac{1}{M}\sum_{i=1}^{M} \Phi(X_i)\Phi(X_i)^T \tag{2.19}$$

where C^F is the covariance matrix. Assuming that v is the eigenvector and λ is the eigenvalue, the following simplified equation can be derived,

$$C^F v = \lambda v \tag{2.20}$$

which allows the transvection approach to be leveraged and formulated as:

$$\langle \Phi(X_k), C^F \rangle = \lambda \langle \Phi(X_k), v \rangle, \qquad k = 1, 2, \dots, M \tag{2.21}$$

It is worth mentioning that the solutions of Eq. (2.20) are contained within the

subspace of $F : \Phi(X_k)$, $(k = 1, 2, \dots, M)$. Hence, there will be a parameter vector $\alpha = [\alpha_1, \dots, \alpha_n]^T$ that converges to the optimal solution as denoted by Eq. (2.22):

$$v = \sum_{i=1}^{M} \alpha_i \Phi(X_i) \tag{2.22}$$

By aggregating Eqs. (2.20) and (2.21) together and defining $K_{ij} = \Phi(X_i), \Phi(X_j)$ as the kernel function, a simplified mapping expression can be obtained;

$$M\lambda\alpha = K\alpha \tag{2.23}$$

where the eigenvalue λ and matrix $K \in R^{M \times M}$ corresponds to $\alpha = [\alpha_1, \dots, \alpha_n]^T$. To extract the principal component, $\Phi(X)$ must be mapped to v_k. Resultantly, Eq. (2.24) is obtained, such that by solving for t_k, the k-th principal component can be derived to generate the singular, fused HI;

$$t_k = \langle v_k, \Phi(X) \rangle = \sum_{i=1}^{M} \alpha_i^k \langle \Phi(X_i), \Phi(X) \rangle, \qquad k = 1, 2, \dots, p \tag{2.24}$$

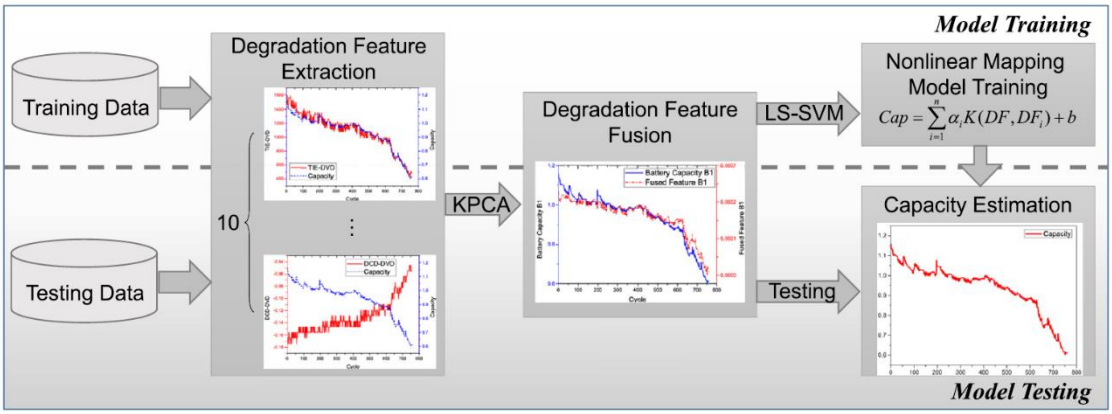

Figure 2.8. HI extraction and capacity estimation via a fusion framework [72].

To enable SOH estimation at different currents, the energy of equal discharging voltage difference (EEDVD) is proposed in [73] but it is still under CC condition and a wide voltage range is required. Extracted from pulse current tests, the voltage knee points (VKP) [74], [75] are relatively easy to obtain but a specific current is required. Moreover, the pulse currents are imposed at a specific SOC level. The concept of combining multiple HIs into a single, optimised HI [72]–[75] ensures decent prediction accuracy across several battery operating conditions. However, during real-world EV propulsion, the fluctuations in current

are more volatile than the simulation tests performed in [72]–[75]. Extensive HI modifications are therefore required to improve the precision of SOH estimation.

2.3 Conclusion

This chapter has indicated that the popularly used ML algorithms in SOH estimation mainly include the DNN, ELM, GPR and SVR, due to their major advantages over traditional methods. For instance, the DNN can automatically pre-process large, raw datasets, thereby reducing the need for extensive feature engineering prior to the online estimation of SOH. ELM trains rapidly unlike traditional NNs and provides improved generalisation performance on new battery data, with fewer parameters. GPR provides a probabilistic learning approach that models complex functions and is particularly effective in high-uncertainty scenarios with limited battery data, which is crucial for reliability in BMSs. The SVR is robust against the overfitting of data, especially when the number of features exceeds the number of observations. Using kernel functions, the SVR can efficiently handle the non-linear relationships that exist in battery degradation trends. RNNs such as LSTMs possess superior structural flexibility, making them adaptable to different HIs while overcoming kernel selection difficulties. Either transfer learning or ensemble learning can be applied during the training of an ML model, so as to increase the training efficiency and the model robustness towards various types of battery data.

It is also discovered that in general, the existing HIs in the literature are derived based on three conditions: 1) CC charging/discharging, 2) a relatively long time interval or a wide voltage variation range, and 3) a specific current. Another limitation found in the existing HIs is their high sensitivity to noise. Hence, filter algorithms need to be applied, and this raises the computational cost. Furthermore, to extract these HIs online, the LIB must operate within a specific current range (i.e., 0.8–2.2 A); which is a major limitation given that the battery discharge process in EVs is usually stochastic. Although the HIs derived from the IC/DV curves, sample entropy, ECM, SPM and P2D can reveal intricate information on the degradation physics of a battery, they are complex by design and often exert heavy computational burden. It is therefore necessary to develop a novel HI that is truncated in nature and can accurately reflect SOH fade.

Chapter 3

Battery Aging Datasets and Model Performance Metric

To evaluate the effectiveness of the SOH estimation methods proposed in this thesis, four LIB datasets comprising of popularly used, battery operation profiles and chemistries are employed. Their respective specifications and cyclic aging procedure are introduced in this chapter. Besides, the performance metric for evaluating the proposed methods is described.

3.1 Introduction

As summarised in Table 3.1, the LIB datasets used in this thesis are: (i) random walk dataset [76] from NASA, (ii) two Worldwide Harmonised Light Vehicles Test Procedure (WLTP) datasets [77] from the University of Michigan, which are based on nickel cobalt aluminium oxide (NCA) chemistry and nickel manganese cobalt oxide (NMC) chemistry, respectively; and (iii) lithium-iron phosphate (LFP) chemistry-based WLTP dataset [78] from Infineon Technologies.

3.2 Random Walk Dataset

The random walk dataset contains the aging data of four 18650-sized (cylindrical) LIBs. The LIBs are of NCA chemistry and respectively labelled as RW3, RW4, RW5 and RW6. They were cycled at room temperature based on three modes of operation, namely charge, discharge and rest. During discharge mode, a randomised sequence of discharging currents is applied onto the LIBs. This type of profile is termed as random walk discharging, wherein each partial discharge cycle lasts 300 seconds and the discharge rate is randomly chosen from a set of currents which range from 0.5 A to 4 A (with a step of 0.5 A). Reference charge and discharge cycles are dispatched after each series of random walk cycles to provide the practical capacity. A reference charge cycle entails a CC step at 2 A until 4.2 V, as well as a CV step until 10 mA. In a reference discharge cycle, discharging is performed at 1 A until the voltage drops to 3.2 V, 3 V, 2.7 V and 2.5 V for RW3, RW4, RW5 and RW6, respectively; thereby manifesting different voltage ranges.

Table 3.1. Specifications of the four LIB aging datasets.

Description	Random walk dataset	WLTP-NCA dataset	WLTP-NMC dataset	WLTP-LFP dataset
Number of batteries	4	4	4	4
Battery labels	RW3 to RW6	A1 to A4	B1 to B4	B5 to B8
Nominal capacity	2.1 Ah	3.2 Ah	5.0 Ah	1.1 Ah
Battery chemistry	NCA	NCA	NMC	LFP
Battery shape	Cylindrical	Pouch	Pouch	Cylindrical
Cycling profile	CC charging, random walk discharging	WLTP drive cycle	WLTP drive cycle	WLTP drive cycle
Voltage range	2.5 V to 4.2 V	3.2 V to 4.2 V	2.0 V to 4.2 V	2.0 V to 3.6 V
Current profile	2 A (charging), 0.5 A to 4.0 A (discharging)	–4.5 A to 4.5 A (charging), –4.5 A to 4.5 A (discharging)	–4.5 A to 4.5 A (charging), –4.5 A to 4.5 A (discharging)	–4.5 A to 4.5 A (charging), –4.5 A to 4.5 A (discharging)
Temperature profile	25°C	40°C	24°C to 32°C	24°C to 32°C

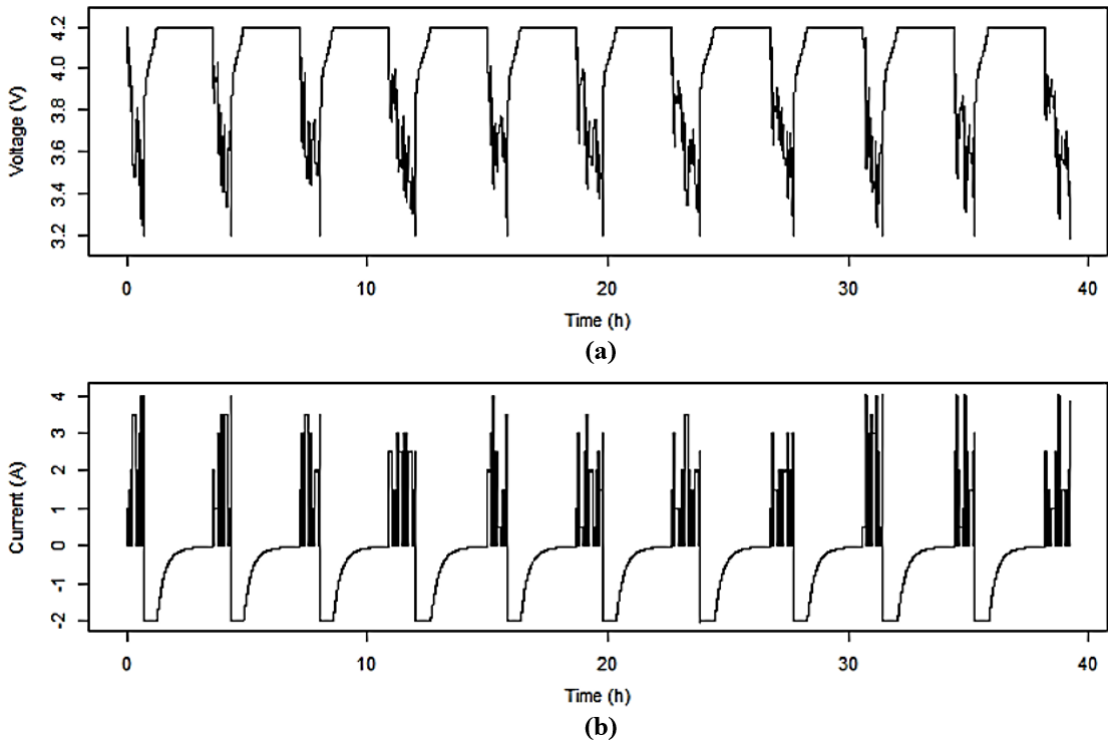

Figure 3.1. Voltage and current profiles under random walk operations [76].

3.3 Drive Cycle (WLTP) Datasets

The three WLTP datasets contain the aging data of both pouch and cylindrical-shaped LIBs. There are twelve LIBs in total, composed of three different chemistries (i.e., NCA, NMC and LFP) that are widely used in EVs. For the three chemistry groups, the LIBs are respectively labelled as A1 to A4, B1 to B4, and B5 to B8. The LIBs were cycled using WLTP for daily urban commute, i.e., home-to-work/work-to-home travel routine, spanning across a five-month long period. This involves an erratic sequence of charging and discharging currents between –4.5 A and 4.5 A with a step of 0.75 A. Each sequence lasts 5 minutes and is followed by a brief rest period (within 1 s). The maximum depth of discharge for each LIB is 70%, assuming full charge (up to 4.2 V) is done overnight. The cut-off voltage for discharging is 2 V. After every 1400 sequences, reference charge/discharge cycles are initiated to compute the ground truth of the battery capacity via coulomb counting. The actual battery capacity can only be calibrated with the reference cycle and the capacity of the erratic sequence is not directly computable. Hence, within each set of 1400 erratic sequences, only the last sequences are chosen, and the capacities are approximated as the capacities of the coming reference cycle. As with the random walk dataset, the battery SOH values for the WLTP datasets are computed using Eq. (1.2).

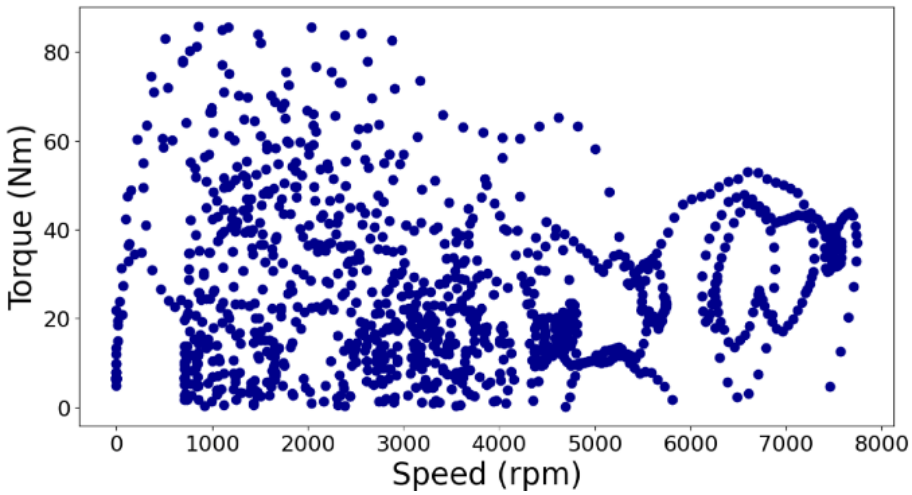

Figure 3.2. EV torque profile for the entire WLTP speed range during urban commute [77], [78].

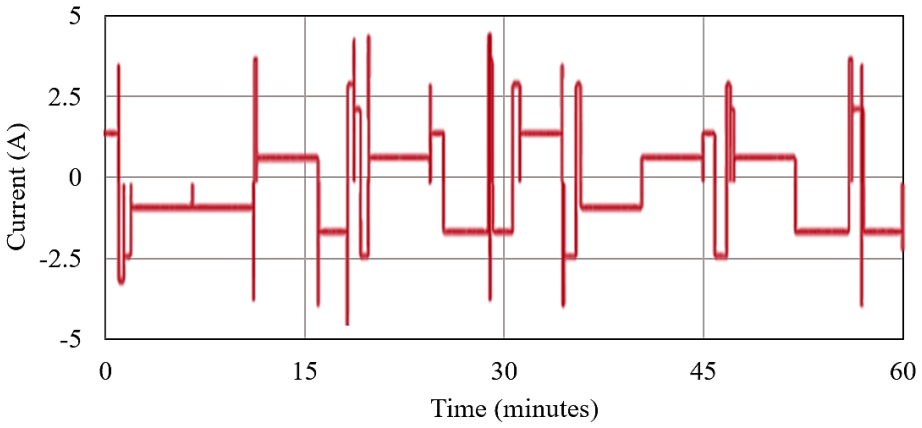

Figure 3.3. Close-up view of the WLTP (dynamic) current profile applied on the LIBs [77], [78].

3.4 Performance Metric for Model Evaluation

To construct the loss function and quantify the SOH estimation errors of the models proposed in this thesis, the model performance metric [79] known as root-mean-square error (RMSE) is applied. It is computed using Eq. (3.1):

$$RMSE = \sqrt{\frac{1}{N}\sum_{i=1}^{N}(\hat{y}_i - y_i)^2} \tag{3.1}$$

where $\hat{y}$ and y represent the estimated and true SOH respectively, while N represents the number of instances in the sampled data. Notably, a lower RMSE indicates a higher SOH estimation accuracy obtained by the model. RMSE penalises large deviations more than small ones (due to squaring), which is beneficial in critical applications like battery health monitoring, where large estimation errors (e.g., estimating 90% SOH when it is 70%) could lead to unsafe operation or poor system performance. Moreover, RMSE provides a single scalar summary of model performance across all data points; and is useful for model comparison during the development and validation stages. In this regard, the RMSE metric is highly applicable towards the SOH estimation models experimented in this thesis.

Chapter 4

Truncated Time Inference-based LSTM Model for SOH Estimation Under Different Discharge Rates

This chapter proposes a data-driven method using a simple but effective HI extracted from a truncated time interval (110 seconds) of the LIB's discharge process, which is a challenge in literature since it is usually less controllable than the charge process. Unlike traditional HIs, the proposed HI can be derived from different voltage ranges, thus making it highly flexible for application. A DL algorithm named the long short-term memory (LSTM) is trained to learn the mapping relationship between the extracted HI and practical SOH of the LIB. The random walk dataset is used to verify whether the developed data-driven method can estimate battery SOH effectively without any additional hardware or system downtime.

4.1 Introduction

As highlighted in Chapter 2, the battery discharge process is dictated by the load profile, whereas the charge process is usually consistent and can be regulated by the BMS. Hence, most of the existing HIs have been designed for extraction based on various parts of the charging voltage curve [58], [59]. However, they require the complete CC and CV charging stages for their extraction, which impedes their transferability during the offline training of the adopted data-driven method [60], [61]. To enable online SOH estimation during randomised battery usage, novel HIs that can be extracted from different discharge rates should be considered and advanced algorithms should be employed to map the relationship between the HIs and the SOH.

This chapter exploits the sampled voltage curve data (an external battery variable), since it is difficult to compute or measure the internal battery variables in practical scenarios where the current could change quickly during the discharge process (e.g., during the regenerative braking of an EV). Therefore, this chapter provides the following contributions:

1) By leveraging quantitative correlation analysis, a truncated time-based HI with strong correlation to battery SOH is extracted. This improved HI, termed as the voltage disparity in truncated time interval (VDTTI), is designed for derivation from a short segment of voltage curves. Since the segment can begin at any time spot, the VDTTI is easy to extract from batteries operating at different voltage ranges.
2) In addition to CC discharge mode, the VDTTI can be extracted in randomised discharge mode, hence enabling the employed data-driven method to obtain SOH estimates of LIBs that often switch between the two modes (differing discharge rates).
3) Through the exploitation of advanced DL, a stacked architecture-based LSTM is used to estimate SOH with the extracted VDTTI. It is highly precise in capturing the capacity regeneration trends of LIBs due to the prioritised learning of capacity data.

4.2 LIB Aging Data Analytics and Proposed Health Indicator

With reference to Eq. (1.2), this thesis defines SOH on the basis of battery capacity, and the degraded SOH is defined as:

$$\text{Degraded SOH} = 100\% - \text{SOH} \tag{4.1}$$

such that the LIB is deemed to have reached its EOL when the degraded SOH is 20% or greater.

4.2.1 Aging Data Analytics

By analysing the capacity degradation curves (Figure 4.1) of the four LIBs (RW3 to RW6) from the random walk dataset, it can be ascertained that the frequent switching between charging and discharging have caused some transient capacity regenerations, despite the capacities' overall decreasing trend with increased cycling. Hence, the degradation curves are not monotonous and this affects the accuracy of SOH estimation. Such non-linear relations will lead to higher data pre-processing requirements for predicting health conditions. It is therefore crucial to extract a high-fidelity HI from an external battery variable, as the HI accounts for the construction of a reliable battery degradation model.

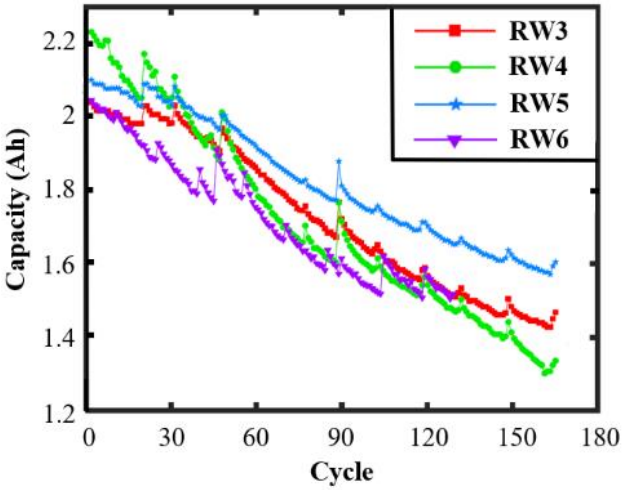

Figure 4.1. Capacity degradation curves of the four LIBs.

To accurately denote SOH, it is best to extract a HI that shares identical or opposite trends with SOH whilst the battery degrades. The capacity can be quantified using coulomb counting, under the premise of full discharge cycles. HIs are therefore only extracted from either a referenced, full discharging cycle or the CC step of the charging cycle prior. In both cases, the current and temperature are unchanging, so it is more appropriate to study the time-varying voltage sequence instead. Using battery RW5 to exemplify the study, Figure 4.2 shows the evolution of both the discharging curves and the CC step of the charging curves, across different stages of cyclic aging.

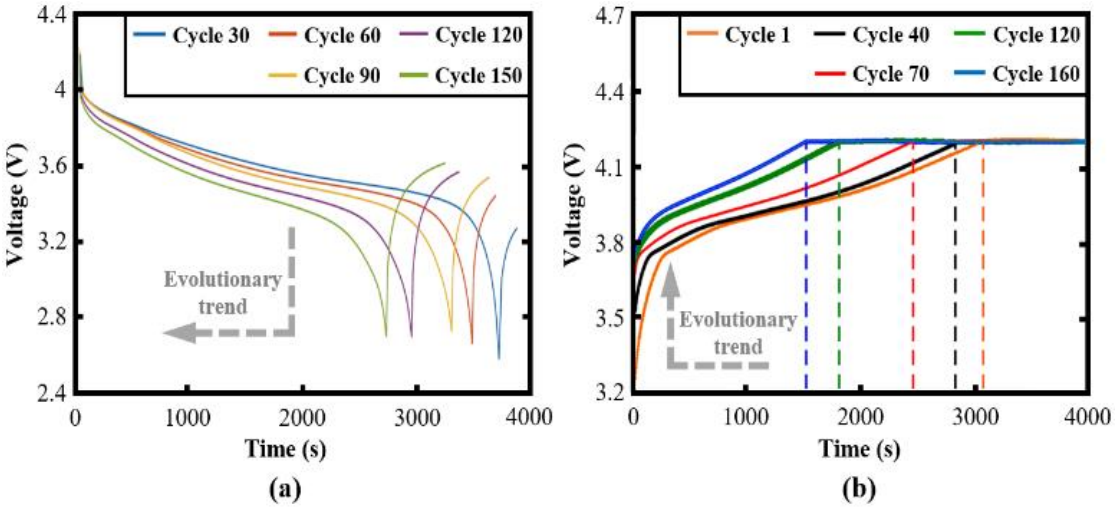

Figure 4.2. Evolution of the time-varying voltage curves of RW5. (a) Discharging curves. (b) CC step of the charging curves.

It is observed in Figure 4.2a that, as RW5 ages and degrades with increasing cycles, the discharging curves gradually shift to the lower left portion of the graph; thereby signifying that the voltage drop speed is increasing. A vaguely comparable trend is observed in Figure 4.2b, whereby the charging curves shift to the upper left portion of the graph to signify the increasing speed of voltage rise. Both observations have revealed that the voltage drop speed of the discharging curve and the voltage rise speed of the charging curve variegate steadily during LIB degradation, which conveys a sense of relatedness to SOH. This inference is further substantiated by Figure 4.3, where the trajectories of the voltage drop beginning at different voltage levels are shown. The voltage drops are derived from the same truncated time interval of 240 seconds. Evidently, the voltage drop speed is progressively increasing based on any given initial voltage. With reference to Eq. (4.1), the degraded SOH is also given to show the identical trend between the voltage drop and the degraded SOH.

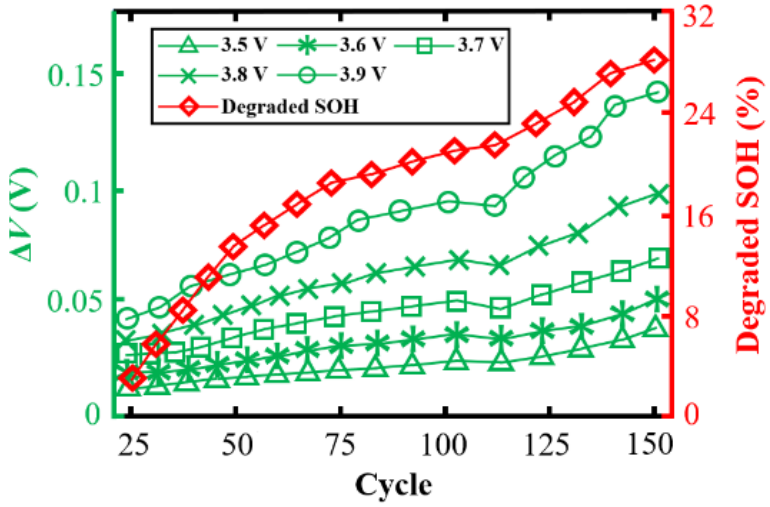

Figure 4.3. Trajectories of the voltage drop and degraded SOH of RW5.

4.2.2 Truncated Time-based Health Indicator

In view of the time-varying voltage trends observed during the LIB's operational cycle life, this chapter develops a truncated time-based HI that closely corresponds with SOH degradation. This HI is named the voltage disparity in truncated time interval (VDTTI). Figure 4.4 depicts the HI extraction process, which is referenced against a discharge cycle. The charge cycle preceding it, including the CV step, are not referenced because they are irrelevant in the extraction of the VDTTI.

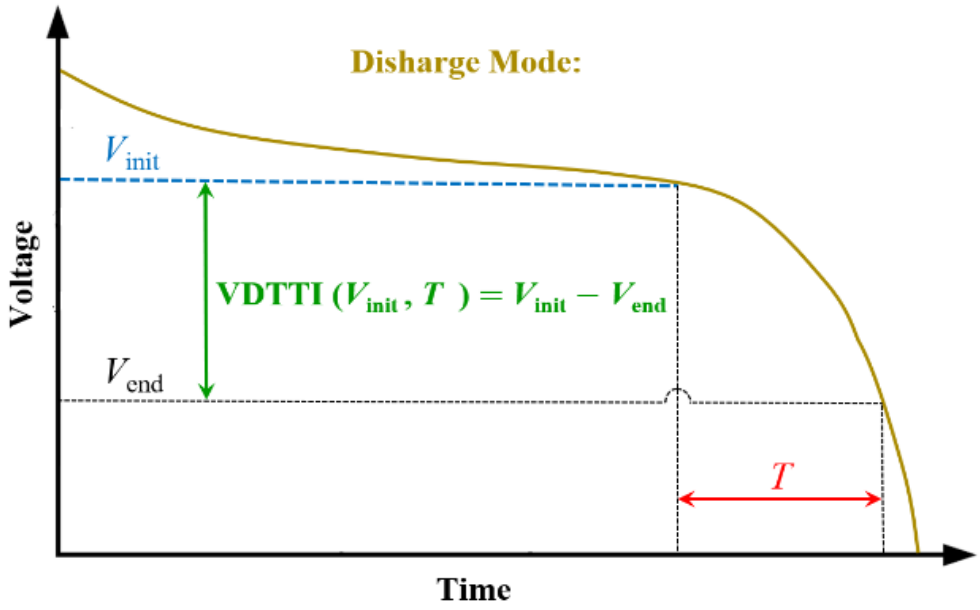

Figure 4.4. Schematic diagram of the proposed VDTTI.

The VDTTI can be formulated by defining two parameters: (i) the initial voltage, and (ii) the truncated time interval. The extraction of the VDTTI is executed in the following four steps:

1) Define the initial voltage V_{init} and detect the corresponding time spot t_1.

2) Define the truncated time interval T.

3) Detect the end voltage V_{end} at $t_2 = t_1 + T$.

4) Compute the extracted HI as,

$$\text{VDTTI}\ (V_{init}, T) = |\ V_{init} - V_{end}\ | \tag{4.2}$$

It is worth noting that the VDTTI is not only applicable in CC charge/discharge scenarios but also applicable in use cases involving randomised charging/discharging, wherein the flow of current is dynamic or inconsistent. A prime example of such use case is the non-uniform acceleration and deceleration of an EV. Herein, the battery load becomes highly dynamic whilst storing recharging pulses with higher currents due to regenerative braking. It is henceforth ideal to define a shortened, or truncated time interval T for computing the VDTTI. With a short T, both current and temperature can be seen as static; thus making it easy to estimate SOH online, even during uncertain LIB operations.

4.2.3 Quantitative Correlation Analysis

To quantitatively evaluate the effectiveness of the extracted VDTTI in acquiring SOH estimates, it is highly vital to perform correlation analysis. This technique assesses both the linear and non-linear monotonic relationships between two variables X and Y, as described using the quantitative metric [80] known as Spearman correlation coefficient (SCC):

$$\mathrm{SCC} = r_{XY} = 1 - \frac{6\sum_{i=1}^{n}\left(R(X_i) - R(Y_i)\right)^2}{n(n^2-1)} \tag{4.3}$$

where n is the number of samples of X and Y, while $R(X_i)$ and $R(Y_i)$ are the rank of X_i and Y_i, respectively. The closer the SCC is to –1 or 1, the stronger the variables' correlation association is. A negative SCC indicates that Y is monotonically decreasing with X, whereas a positive SCC indicates that Y is monotonically increasing with X. In this chapter, X represents the VDTTI while Y represents the SOH. Using battery RW5 of the random walk dataset to exemplify the correlation analysis, Table 4.1 records the SCCs between the various extracted VDTTI (X) and the SOH (Y). For every T, different values of V_{init} are analysed until the entirety of the practicable voltage range is covered.

Table 4.1. SCC between VDTTI (discharge mode) and SOH.

V_{init} (V) \ T (s)	70	90	110	130	150
3.5	0.922	0.942	**0.966**	0.945	0.949
3.6	0.922	0.942	**0.966**	0.945	0.949
3.7	0.922	0.942	**0.966**	0.945	0.949
3.8	0.922	0.942	**0.964**	0.817	0.255
3.9	0.875	–0.736	**–0.961**	–0.945	–0.949

From the table, it is deduced that with any initial voltage, a longer time interval may constitute a stronger correlation. However, this also makes it harder to extract the VDTTI in cases where the LIB regularly alternates between charging and discharging (e.g., regenerative braking). Therefore, a practical time interval of 110 seconds and an initial voltage of 3.7 V are both chosen to finalise the VDTTI extraction. Notably, the SCCs at 110 seconds are closest to either –1 or 1; thereby denoting exceptionally strong ties with SOH.

4.3 Proposed SOH Estimation Framework

4.3.1 Overview of the Framework

Figure 4.5 illustrates the overall framework of the proposed data-driven SOH estimation method, which entails an offline training phase and an online estimation phase. In the offline training phase, the historical voltage, time and capacity data are collected from the random walk dataset. Using the practical capacity values, the true SOH values are computed for the purpose of benchmarking. Through quantitative correlation analysis, an extracted feature which has a strong relationship with the true SOH is employed as the HI. The DL algorithm known as LSTM is then applied to map the relationship between the HI (i.e., VDTTI) and the true SOH, and to estimate the SOH degradation trend of the LIB. Notably, the hidden layers of the LSTM are stacked atop each other to enhance the training efficiency and accuracy. In the online estimation phase, the VDTTI extracted from the real-time measurements is transferred to the trained LSTM to estimate SOH. It is worth mentioning that the training data is generated from offline, battery aging experiments, whereas the real-time measurements are obtained online.

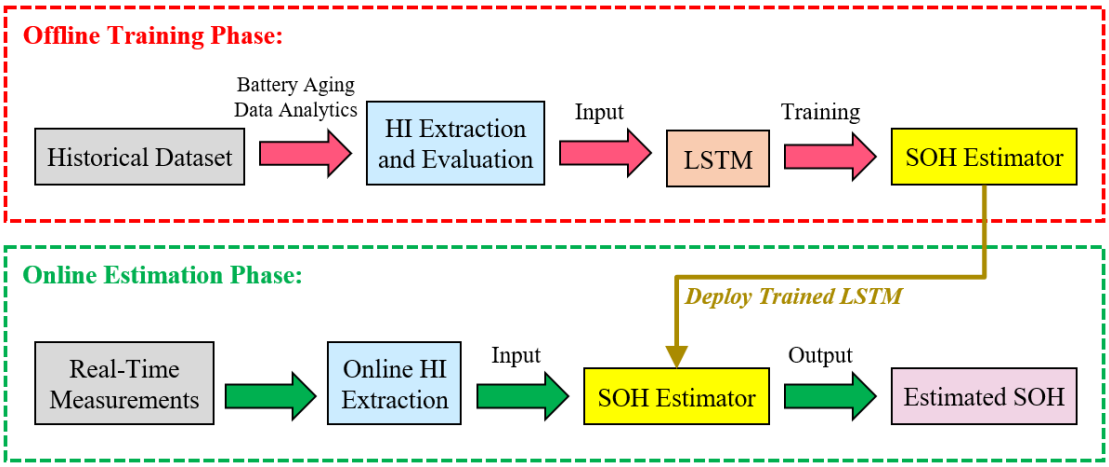

Figure 4.5. Framework of the proposed data-driven SOH estimation method.

4.3.2 Long Short-Term Memory

The LSTM is a unique RNN variant that exploits its memory cells instead of the conventional hidden nodes, so as to avoid gradient vanishing and explosion [81]. Figure 4.6 illustrates the cell schematic which mainly consists of an input

gate, an output gate, and a forget gate. These gates perform the act of collecting data, outputting estimations, and removing needless information, respectively. Another beneficial trait of the LSTM is the cell state. It stores a compilation of past input sequences to prioritise useful information to memorise.

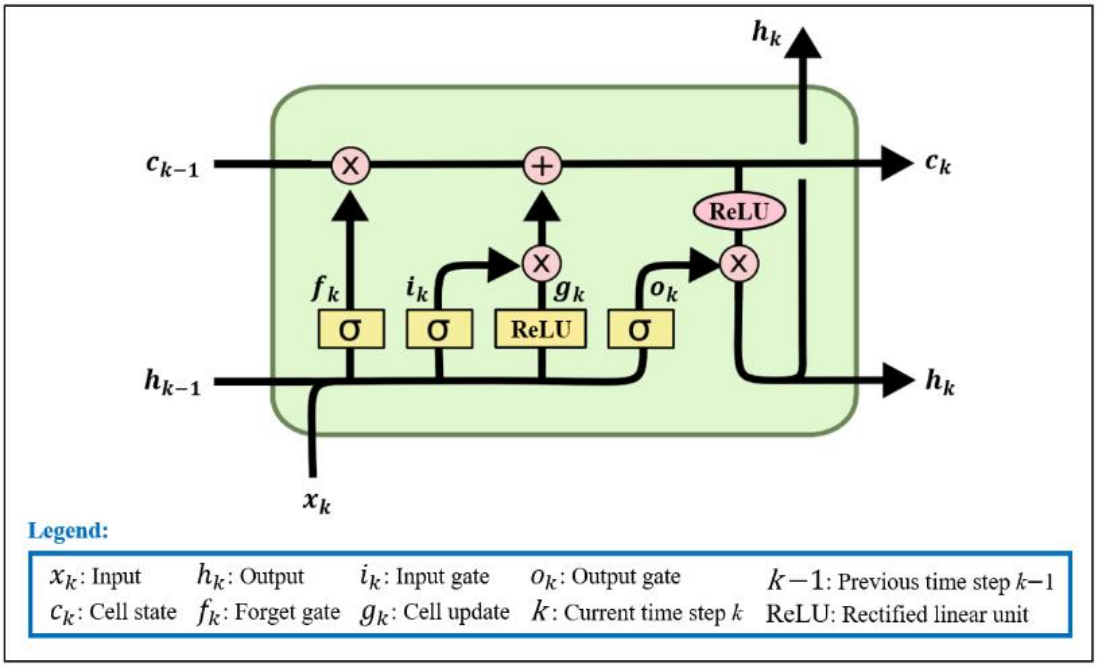

Figure 4.6. Schematic diagram of a memory cell used in LSTM layers.

Eq. (4.4) describes the functionalities of the LSTM, wherein b is the bias parameter, while W_x and W_h represent the weight matrices for the input and the previous output, respectively. The element-wise product is denoted by $\odot$, whereas σ expresses the sigmoid function that is an activation function. The first three equations determine the amount of information for the cell memory to update, forget, and output its state; whereas the last two recursive equations determine the cell state and output.

$$\begin{cases} i_k = \sigma(W_{xi}x_k + W_{hi}h_{k-1} + b_i) \\ f_k = \sigma\left(W_{xf}x_k + W_{hf}h_{k-1} + b_f\right) \\ o_k = \sigma(W_{xo}x_k + W_{ho}h_{k-1} + b_o) \\ c_k = f_k \odot C_{k-1} + i_k \odot \mathrm{ReLU}\,(W_{xc}x_k + W_{hc}h_{k-1} + b_c) \\ h_k = o_k \odot \mathrm{ReLU}\,(c_k) \end{cases} \tag{4.4}$$

To formulate an SOH estimator with the extracted VDTTI, the stacked LSTM topology involving regression (i.e., Figure 4.7) is employed. The increased depth of the network structure, attributed by stacking two LSTM layers, offers a simple

learning solution that requires fewer hidden nodes and expedites training [81]. Herein, only three of the LSTM's hyperparameters need to be actively tuned in order to attain optimised learning efficiency. They are the batch size, number of hidden nodes and epochs.

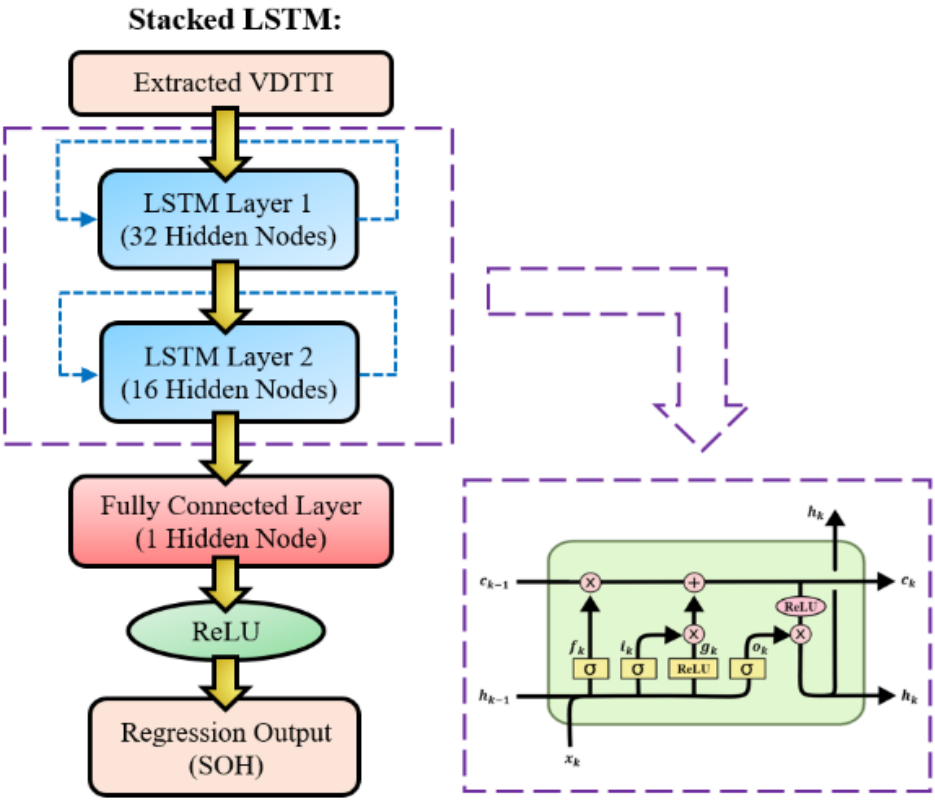

Figure 4.7. Stacked network structure of the LSTM.

4.4 Testing Results and Discussion

With MATLAB R2022a testbed, the four LIBs of the random walk dataset, namely RW3, RW4, RW5 and RW6, are used to evaluate the proposed data-driven method for online SOH estimation. To quantify the estimation errors of the method, the performance metric named RMSE is applied, i.e., Eq. (3.1). For the evaluation test, given the data of the four LIBs, the data of three LIBs are routinely used to train the LSTM to estimate the SOH of the remaining LIB (i.e., the test set); until all four LIBs have been used once as a test set. This test procedure is widely known as four-fold cross validation [21]. Based on the test results shown in Figure 4.8, it is apparent that the proposed data-driven method is well-capable of securing highly accurate SOH estimates; as the reported

RMSEs of the four LIBs are just between 0.73% and 1.24%, and the average RMSE is 0.94%. Moreover, all four SOH degradation curves have demonstrated that the estimated SOHs can closely track the true SOHs, thereby indicating good performance of the proposed VDTTI at various discharging currents when implemented with the LSTM.

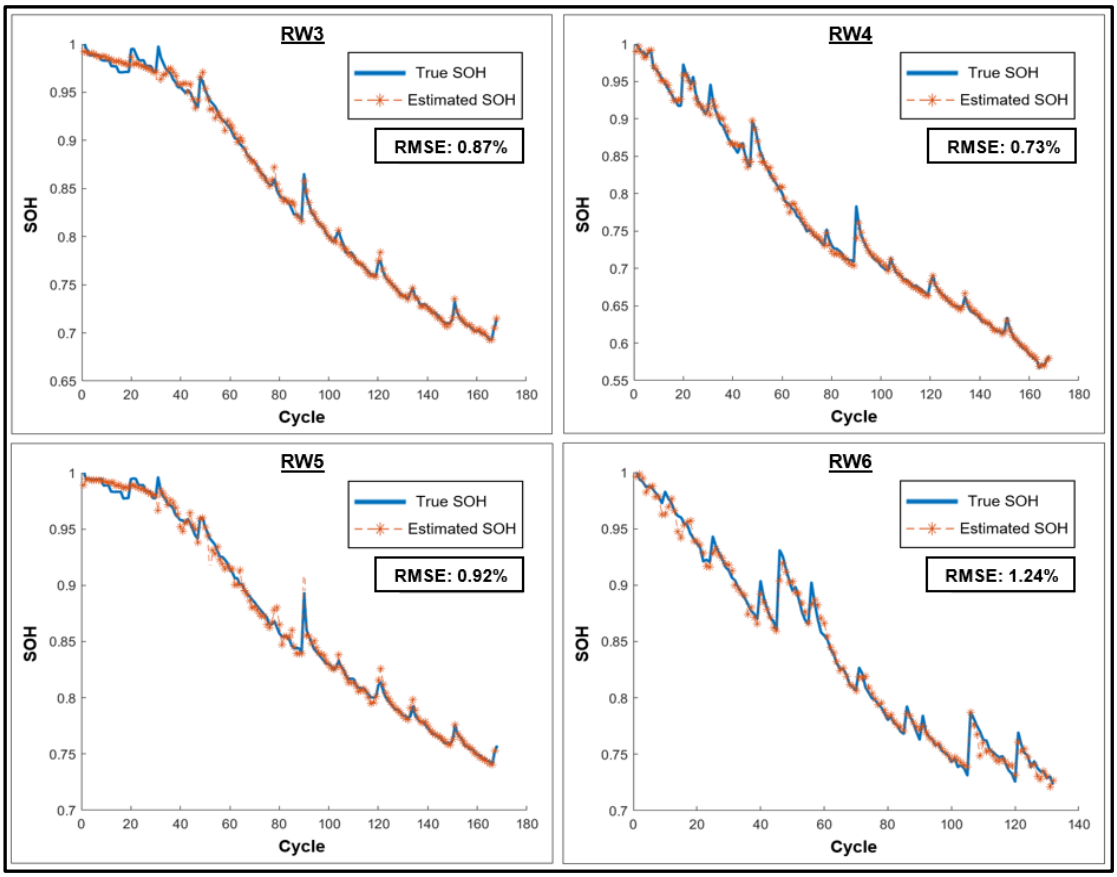

Figure 4.8. SOH estimation results of RW3, RW4, RW5 and RW6, using the proposed VDTTI (i.e., extracted at T = 110 s and V_{init} = 3.7 V).

Table 4.2. Performance comparison of different methods.

Method	RMSE (%)					Time (s)	
	RW3	RW4	RW5	RW6	Avg.	Train.	Test.
VDEDT [69] + LSTM	1.2	1.53	1.61	1.76	1.53	66.48	0.34
VDTTI+LSTM	**0.87**	**0.73**	**0.92**	**1.24**	**0.94**	**51.63**	**0.32**
VDTTI+GPR	0.98	0.81	1.3	1.49	1.15	72.02	0.21
VDTTI+SVR	1.83	2.09	2.26	2.14	2.08	79.55	0.5
VDTTI+DTR	2.03	2.57	2.69	2.25	2.39	98.47	0.38

*****RMSEs are displayed in percentage (%) format for the ease of error analysis.*

Table 4.2 summarises the comparison between the proposed method (i.e., VDTTI+LSTM) and four benchmark methods. The first benchmark method employs VDEDT [69] as the HI and implements it with the LSTM. Herein, the timed HI extraction is 500 seconds, which is much longer than the requirement of the proposed VDTTI. The other benchmark methods employ the proposed VDTTI as the HI and implements it with three renowned, regression-based ML algorithms; namely the Gaussian process regression (GPR) [44], support vector regression (SVR) [48], and decision tree regression (DTR) [82]. Evidently, the proposed method exhibits the highest SOH estimation accuracy and the fastest training time (51.63 s) on average. Its average testing time (0.32 s) however, is longer than that of the GPR.

4.5 Conclusion

This chapter has developed VDTTI as the HI and proposed a data-driven method for online SOH estimation under randomised battery usage, where the discharging currents are stochastic. Since the VDTTI is both a singular and truncated feature, it does not need to be pre-processed with a filter. A shorter time interval (T) can be employed to extract the VDTTI for use in dynamic battery operations, but not without the cost of slight accuracy sacrifice (i.e., 0.04% to 0.25% increase in RMSE when $T \leq 150$ s). Such operations, which typically involve either EV usage or regulation of the power grid frequency, would require T to be 150 s or less, since there would only be marginal variation in the real-time measured LIB variables during that period. Furthermore, T can be optimally selected with the use of statistical methods such as SCC analysis. The testing results show that the proposed method can estimate SOH with high accuracy as the average RMSE is 0.94%.

Chapter 5

Hierarchical Ensemble Model for SOH Estimation Under Dynamic Discharging Currents

The method developed in Chapter 4 enables SOH estimation under randomised battery usage, where the discharge rates are inconsistent and the timed extraction of the HI is 110 seconds. However, if the operating current changes dynamically within a very short time span, e.g., 5 seconds or less, this method would not be able to work. Aiming at online SOH estimation of LIBs under dynamic discharging, this chapter proposes a momentary HI that is extracted from a very short interval (< 0.1 s) when the LIB transits from discharging to rest. This HI is exceptionally easy to implement under various discharging currents and SOC levels. Moreover, it does not require a filtering step as it is both singular and truncated. The rationality of the proposed HI is to indirectly reflect battery internal resistance, which is justified by theoretical analysis with an ECM. Then, a hierarchical ensemble model (HEM) of esteemed ML algorithms is designed to efficiently learn the relationship between the HI and SOH through momentary informatics. The efficacy of the proposed data-driven method is demonstrated by hardware-in-the-loop (HIL) experiments involving the WLTP datasets.

5.1 Introduction

As mentioned in previous chapters, most of the existing HIs are derived from a long sequence of charging/discharging voltage curves. This makes them inflexible for LIBs operating at various currents and limits the expandability of the data-driven method for practical use. For data-driven methods, selecting more HIs as the ML model's input will not necessarily yield a higher estimation accuracy [22]. The HI selection process may also be susceptible to cumulative errors, long extraction time, and interference sensitivity [63], [65]. In practice, the loading profiles of batteries in EV propulsion applications are highly volatile, and the aforementioned condition on HI extraction heavily restrain the real-world applicability of the data-driven method. In the literature, ML algorithms such as the DNN [51], ELM [43], GPR [44] and SVR [48], are well-acknowledged due to

their interpretability and relatively fast learning speed when dealing with HIs, especially if compared to the computationally expensive, RNNs [54], [55].

Hence, this chapter firstly develops a momentary HI that is extracted from the voltage and current profiles during the transition from discharge mode to rest mode, i.e., immediately after the battery stops discharging. Thereafter, the DNN, ELM, GPR and SVR are hierarchically ensembled to intelligently learn the mapping relationship between the HI and SOH, which in turn enables real-time SOH estimation under various discharging currents. In summary, this chapter has the following contributions:

1) A comprehensive analysis of the electrical dynamics surrounding battery aging is performed based on a referenced ECM. It is revealed that the ohmic resistance would increase as the battery capacity degrades, and hence the equivalent voltage and current variables can be aggregated into a HI for indirect expression of SOH.
2) A new, momentary HI, named the electrical transient during short time interval (ETSTI), is derived from the momentary transition phase that occurs in between battery discharging and rest. Since the transition can begin at any voltage level, the ETSTI is easy to extract and implement under various discharging currents and SOC levels. The singular and truncated nature of the ETSTI allows it to be sampled and processed immediately without a filtering step, thereby nullifying the prospect of incurring additional computational costs. Such principle is termed as “momentary informatics”.
3) A hierarchical ensemble model (HEM) of four popular ML algorithms, namely the DNN, ELM, GPR and SVR, is designed for SOH estimation using the ETSTI as the input. The rationale behind this innovation is to: (i) exploit the complementary strengths of different ML algorithms via a dual-level training process. (ii) Diversify and optimise the learning of model weights with only a limited number of ML algorithms. (iii) Attain an estimation accuracy that surpasses both single-model and traditional ensemble model frameworks, with far greater computation savings.
4) The real-time viability of the proposed method is verified through hardware-in-the-loop (HIL) experiments involving an industrial BMS microcontroller.

Besides the estimation errors, model complexities such as training/process time, Flash/RAM size and MACC operations, are also studied.

5.2 Theoretical Analysis and Proposed Health Indicator

5.2.1 Internal Ohmic Resistance

The electrical dynamics of a battery can be modelled with different ECMs. For instance, the Thevenin model [83] illustrated in Figure 5.1a is widely applied to model the battery with the open-circuit voltage (OCV) V_{OC}, ohmic resistance R_{o}, polarised resistance R_1, capacitor C, load current I_L, and load voltage V_L. It is worth noting that V_{OC}, R_{o}, R_1 and C are also associated with the SOC. Hence, the electrical characteristics of the battery can be modelled as:

$$V_{\mathrm{OC}}(\mathrm{SOC}) = I_L \cdot R_{\mathrm{o}}(\mathrm{SOC}) + V_C + V_L \tag{5.1}$$

$$\dot{V}_C = -\frac{V_C}{R_1(\mathrm{SOC}) \cdot C_1(\mathrm{SOC})} + \frac{I_L}{C_1(\mathrm{SOC})} \tag{5.2}$$

It is reported that the ohmic resistance R_{o} would increase as the capacity declines, and therefore it can be used as the HI for capacity-linked SOH estimation [31], i.e., $\mathrm{SOH} = f(R_{\mathrm{o}}(\mathrm{SOC}))$. Traditionally, R_{o} can be estimated using the RLS algorithm [29], in relation to the dynamics in Eqs. (5.1) and (5.2). However, this approach is susceptible to numerical stability issues and an accurate ECM is mandatory. Based on such mechanics, this chapter develops a novel HI that can indirectly reflect the ohmic resistance and be efficiently exploited by data-driven methods.

5.2.2 Momentary Health Indicator

The extraction process of the proposed HI, named the electrical transient during short time interval (ETSTI), is depicted in Figure 5.1b using the WLTP battery data obtained from the University of Michigan. Herein, four CC discharging tests are performed consecutively at various rates. Each discharging cycle lasts 5 minutes and is followed by a very short resting period. The zoomed-in figure on the right indicates one transition from discharge mode ($I_1 = 1.5\ \mathrm{A}$) to rest mode ($I_2 = 0$) of the battery. As shown, there is a sudden voltage rise during the transition. Composed of three parameters that are analogous to momentary

informatics, the ETSTI is expressed as:

$$\mathrm{ETSTI} = [V_{\mathrm{rise}}, V_2, I_1] \tag{5.3}$$

where $V_{\mathrm{rise}} = V_2 - V_1$ is the momentary voltage rise when the battery transits from discharging to resting; V_2 is the voltage at rest mode and I_1 is the current of discharge mode.

The parameters of the ETSTI (voltage and current) can be directly measured by the BMS within a very short time interval (< 0.1 s), thereby making the ETSTI exceptionally easy to obtain in practical applications. Notably, the condition to stop discharging is reasonably easy to meet in practice. This includes the braking of an EV or when a power grid battery enters the resting stage. In view of this analogy, this chapter selects a practical time interval of 0.04 s to extract the ETSTI.

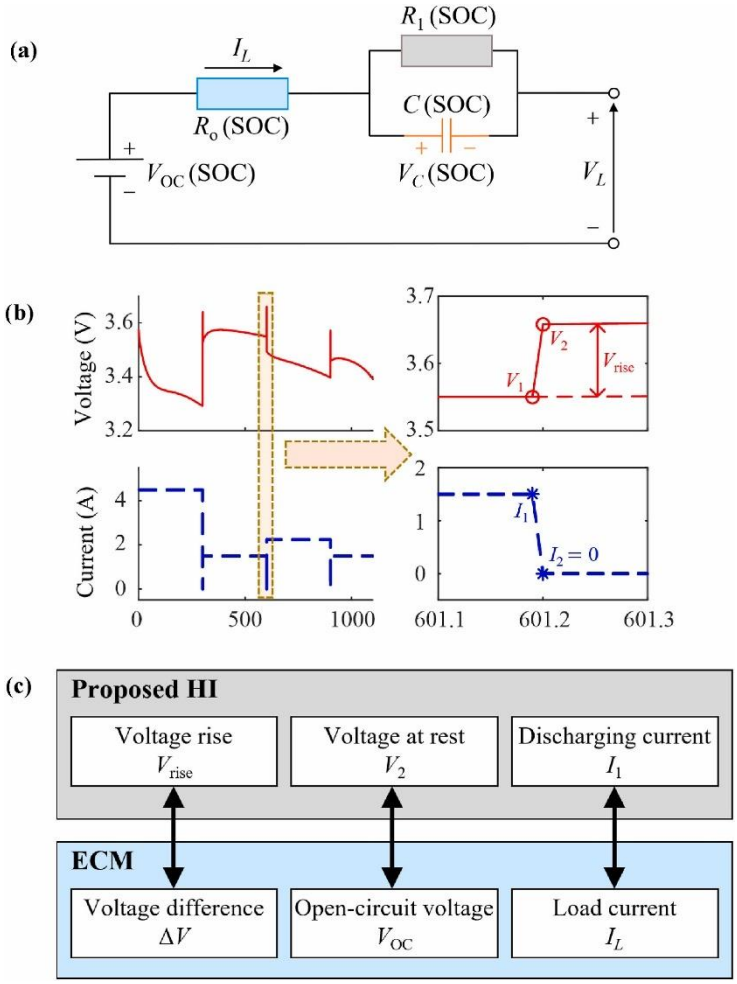

Figure 5.1. (a) Schematic diagram of the Thevenin model of an LIB. (b) HI extraction process. X-axis: Time (s). (c) Links between the proposed HI (ETSTI) and ECM parameters.

5.2.3 Theoretical Analysis

This section justifies the theoretical rationality of the ETSTI. From Eq. (5.1), the voltage difference between V_{OC} and V_L is calculated as:

$$\Delta V = V_{\mathrm{OC}}(\mathrm{SOC}) - V_L = I_L \cdot R_{\mathrm{o}}(\mathrm{SOC}) + V_C \tag{5.4}$$

Under an instant load change, the capacitor voltage V_C remains almost unchanged. Therefore, the ohmic resistance R_{o} can be estimated with the load current I_L, voltage difference ΔV, and battery SOC:

$$R_{\mathrm{o}}(\mathrm{SOC}) = \frac{\Delta V}{I_L} \tag{5.5}$$

The SOC can be represented by V_{OC}, given that OCV is a non-linear function of SOC. Thereafter, Eq. (5.5) can be rewritten as:

$$R_{\mathrm{o}} = g(\Delta V, I_L, V_{\mathrm{oc}}) \tag{5.6}$$

where $g(\cdot)$ denotes the underlying relationship between the input parameters and the ohmic resistance.

In Eq. (5.4), V_{OC} and V_L correspond to V_2 and V_1 in Figure 5.1b when the load current drops from I_L (I_1 of the ETSTI) to zero. Therefore, ΔV in Eq. (5.6) is equivalent to V_{rise} of the ETSTI in Eq. (5.3). Voltage at the resting mode V_2 in Figure 5.1b and Eq. (5.3) can be approximated as V_{OC} because the discharging current is zero. The correlative links between the parameters of the ETSTI in Eq. (5.3) and the ECM parameters in Eq. (5.6) are depicted in Figure 5.1c. On this basis, it can be ascertained that the ETSTI in Eq. (5.3) is an indirect expression of the ohmic resistance, i.e., $R_{\mathrm{o}} = g(\mathrm{ETSTI})$. Taking into consideration of the relationship between the capacity and ohmic resistance, the capacity-based SOH can ultimately be modelled with the ETSTI directly, as shown in Eq. (5.7):

$$\mathrm{SOH} = f(R_{\mathrm{o}}) = f(g(\mathrm{ETSTI})) = h(\mathrm{ETSTI}) \tag{5.7}$$

where h denotes the ML model that directly maps the relationship between the ETSTI and SOH.

Notably, the aggregation of SOC-associated parameters such as the discharging current and momentary voltage rise enables the ETSTI to be

applicable under various discharging currents and SOC levels. It is also worth noting that with any other ECM, the ohmic resistance can still be similarly modelled by the load current I_L, voltage difference ΔV, and battery SOC. Therefore, the theoretical rationality of the ETSTI still holds.

5.3 Hierarchical Ensemble Machine Learning Model

ML models map the input HI to the output prediction and then estimate the SOH based on the data learned. Besides the HI, the choice of ML algorithms also affects the estimation performance. In the literature, the four leading ML algorithms in SOH estimation are the DNN, ELM, GPR and SVR. Hence, this chapter designs a hierarchical ensemble model of them for dual-level, diversified learning based on the complementary strengths of each algorithm. This enables improved estimation accuracy and computational efficiency when compared to both single-model and traditional ensemble model frameworks.

5.3.1 Deep Neural Network

DNNs mathematically mimic the human brain mechanics when dealing with non-linear problems. The DNN consists of an input layer, an output layer, and multiple hidden layers [56]. The input layer receives the pre-processed data and acts as a window between the hidden layers and the input HI. Each neuron in the hidden layers encompasses a mathematical model that determines the output based on the input, and can be described by a weighted linear amalgam stored in the activation function. Herein, the total value is transfigured into the activation value of the neuron by the activation function. It becomes the input to the succeeding neuron until the output activation value is finalised. The accuracy of the output (e.g., estimated SOH) is determined by the chosen number of hidden layers and neurons, the weights of each neuron, and the activation function. Generally, DNNs are trained using backpropagation [36]; an optimisation algorithm that involves the use of gradient descent to optimise the weights and biases. The DNN model is mathematically described in Eq. (2.8).

5.3.2 Support Vector Regression

The SVR is another popular ML algorithm used on non-linear regression

problems such as SOH estimation. It maps data to a high-dimensional space and builds an optimal separating hyperplane within the space. The key to the data transformation is a kernel function. By leveraging the constraints of the Karush–Kuhn–Tucker condition [84], only a fraction of the training data known as support vectors will be kept and used to formulate an estimation model. The SVR model is described as:

$$f(x) = w\varphi(x) + b, x \in R^m, b \in R \tag{5.8}$$

where x is the input matrix with m features, $\varphi(x)$ is a non-linear mapping function, and w and b denote the weight matrix and intercept of the hyperplane, respectively. To solve non-linear regression problems, an insensitive loss function [49] is usually applied:

$$L(f(x), y) = \begin{cases} 0, & |y - f(x)| \leq \varepsilon \\ |y - f(x)| - \varepsilon, & |y - f(x)| > \varepsilon \end{cases} \tag{5.9}$$

where ε is the permissible error between the estimated value and the true value.

5.3.3 Extreme Learning Machine

A randomised learning algorithm, the ELM is renowned for using randomly assigned input weights and biases to augment its computational scalability. Naturally distinct from traditional ML algorithms which mostly adhere to a specific learning trajectory, the ELM strives to attain not only the lowest training error but also the smallest array of output weights. Notably, the ELM requires fewer optimisation constraints than the DNN and SVR; hence attributing a simpler network structure, faster training speed, and superior generalisation performance [85]. The ELM has three layers, i.e., the input, hidden and output layers [42]. Given that a dataset is $Set = \{X, T\}$, where X and T are the input and target, respectively, the ELM can be described as:

$$Y = g(W \cdot X^T + b)^T \cdot \beta \tag{5.10}$$

where $g(\cdot)$ denotes the activation function, W is the randomised input weight matrix, b is the bias of hidden neurons, and β is the output weight vector. As the ELM is structurally plain, the only hyperparameters that need to be actively tuned are the activation function and the number of hidden neurons. The aim of the ELM's learning process is to discover the optimal β that minimises the

training error. This can be effortlessly solved via matrix computation, in which the optimal β is computed as:

$$\hat{\beta} = H^{\dagger} \cdot T \tag{5.11}$$

where $H^{\dagger}$ is the Moore–Penrose generalised inverse matrix [86] of $H = g(W \cdot X^T + b)^T$.

5.3.4 Gaussian Process Regression

The GPR, an advanced probabilistic predictor, is widely engaged for battery SOH estimation due to its non-parametric, flexible and probabilistic traits. Herein, any system behaviour can be modelled via a proper combination of the Gaussian process, which leads to the acquisition of SOH estimates based on a Bayesian framework that has been integrated with prior knowledge [87]. The framework comprises of finite variable sets, where each set is jointly Gaussian distributed. By spreading the multivariate Gaussian distribution to infinite dimension, the Gaussian process $f(x)$ can be obtained. It is formulated using the mean function $m(x)$ and the covariance function $k(x_i, x_j)$:

$$m(x) = E(f(x)) \tag{5.12}$$

$$k_f(x_i, x_j) = E\left[\left(f(x_i) - m(x_i)\right)\left(f(x_j) - m(x_j)\right)\right] \tag{5.13}$$

The covariance function [79] is applied to apprehend the similarity between the input HI and battery SOH. It is very receptive to the GPR's estimation performance, and the hyperparameters are optimised by the best possible prediction of the edge probability. The prior distribution is established based on the training and test data, whereas the predicted posterior distribution is obtained using Bayesian theory:

$$p(y_m \mid x_t, y_t, x_m) = N(\mu_m, \sigma_m^2) \tag{5.14}$$

where x_t, y_t are the input and output of the training sample, x_m, y_m are the input and forecast output of the test sample, m is the predicted mean, and σ_m^2 is the predicted variance.

5.3.5 Proposed SOH Estimation Framework

Figure 5.2 presents the proposed data-driven method for SOH estimation which

involves two phases. In the offline training phase, all the historical voltage, current and temperature data of the LIB are collected as the training data. By referencing the discharge cycles, several momentary HIs are then extracted and correlation analysis is performed to evaluate the effectiveness of the extracted HIs in denoting SOH. Thereafter, the formalised ETSTI is inputted to each of the four ML models (DNN, ELM, GPR and SVR) for first-level training based on momentary informatics. As in the average ensemble model (AEM) framework [88], [89], each ML model at the first level is distinct from others with a unique input weight matrix. Correspondingly, a hierarchical ensemble model (HEM) is established based on all four ML models that have been trained using the same input, with each ML model providing a unique estimated SOH. The four SOHs from the first level are then used as inputs to train a second ELM at the second level, of which the output is the final estimated SOH. In essence, this second-level ELM intelligently aggregates all four outputs from the first level since it may not be optimum to compute the mean SOH instead. The ELM's randomised learning ability induces diversity, which is the foundation of ensemble learning and therefore the ELM is employed in both levels of model training.

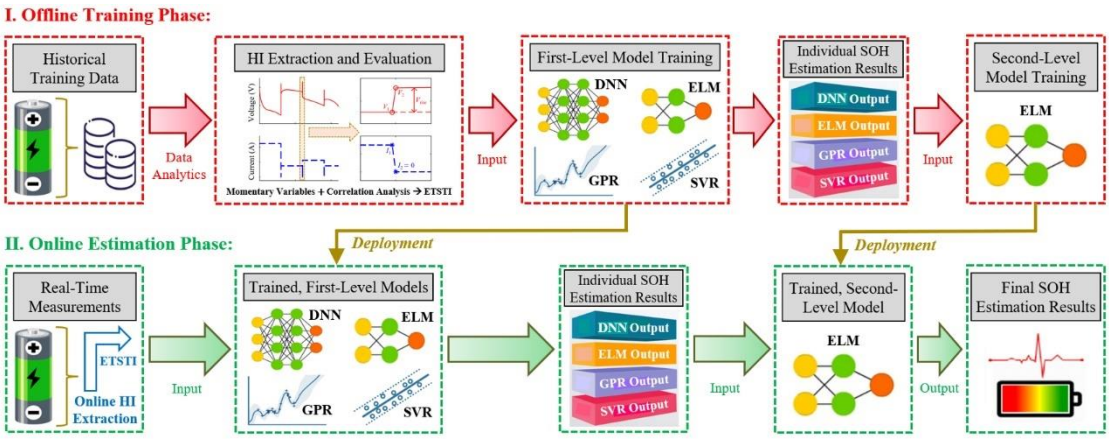

Figure 5.2. Framework of the proposed, hierarchical ensemble-based SOH estimation method.

In the online estimation phase, the ETSTI is extracted from the real-time measurements of the operational LIB and inputted to the four ML models at the first level. Then, the four estimated SOHs are collectively inputted to the well-trained, second-level ELM, which outputs the final estimated SOH. Mathematically, the final estimated SOH can be computed through Eq. (5.11)

and expressed as:

$$SOH_{\text{final}} = g(W \cdot SOH^T + b)^T \cdot \beta \quad (5.15)$$

where SOH is the vector containing N estimated SOHs. The estimated SOH of each first-level ML model is arbitrarily skewed from the true output and therefore, theoretically, the mean value of these SOHs should equate to the true SOH if the quantity of ML models is infinite. In actuality, however, it is impracticable to train an infinite number of ML models.

As such, the proposed HEM framework (Figure 5.2) is curated to intelligently learn the weights of a limited number of ML models across the two training levels, and consequently obtain better results than simply averaging, i.e., using traditional ensemble methods such as the AEM to compute the mean SOH. To achieve high-fidelity estimation performance, the first-level, collective training of the four ML models only requires minimal sets of training iteration (i.e., 45 epochs), while the training of the second-level ELM only requires 15 epochs. This is attributed by the stochastic intelligence of the HEM, derived from the complementary learning strengths of the DNN, ELM, GPR and SVR. Specifically, DNN excels at capturing complex patterns in data and can effectively handle large amounts of data. SVR is effective for handling high-dimensional data and is robust against overfitting, thus making it ideal for modelling complex patterns. GPR is valuable for modelling uncertainty and providing probabilistic predictions. ELM, with its fast training speed and ability to generalise well to unseen data, can reciprocate the other three ML models by providing efficient learning and prediction. It is worth mentioning that unlike the HEM framework, single-model frameworks generally require a more tedious and prolonged training process to attain optimised performance due to their limited learning capacity [90], [91]. Therefore, their computational burden is found to be relatively high.

Although computationally efficient, possible candidate models such as random forest (RF) [92] and extreme gradient boosting (XGBoost) [93] are not chosen for integration into the HEM framework due to the following key reasons: 1) RF may struggle with high-dimensional battery data and will be prone to overfitting if not properly tuned. It also lacks interpretability when compared to the DNN,

ELM, GPR and SVR, thus making it difficult to comprehend the effect of individual features on SOH estimation. 2) XGBoost is highly sensitive to hyperparameter tuning. If not optimised correctly, severe overfitting or underfitting will occur. Furthermore, the architectural complexity of the XGBoost can make it less interpretable, which is a critical aspect in BMSs. Aside from RF and XGBoost, more advanced data-driven methods have been recently proposed for high-accuracy SOH estimation. This includes the IC-based broad learning system system (IC-BLS) [94], the gradual decreasing current with double correlation analysis-based gated recurrent unit (GDCA-GRU) [95], and the incremental energy per SOC-integrated long short-term memory reduction (IES-LSTMR) [96].

However, in comparison to the proposed HEM incorporating DNN, ELM, GPR and SVR, each of these three methods possess the respective major drawbacks which restrict their practicality: 1) the BLS network, while capable of modelling large datasets, requires extensive computational resources and can be complex to deploy effectively in a BMS microcontroller. 2) The effectiveness of GDCA is dependent on specific current profiles, which may not be representative of all battery operating conditions. Moreover, the complexity of the GRU can lead to challenges in training and convergence, especially with limited data. 3) While long short-term memory (LSTM) based networks are highly robust for time series prediction, they can be compute-intensive and require large volumes of training data. The IES approach may also introduce noise if the energy measurements are inaccurate, potentially affecting the precision of SOH estimation. Section 5.4 justifies the superiority of the HEM over the other ML models (AEM, etc.) when integrated with the ETSTI.

5.4 Experimental Results and Discussion

5.4.1 Hardware-in-the-Loop Testbed Description

To evaluate the real-time viability of the proposed method involving ETSTI and HEM, a series of HIL experiments are performed. Figure 5.3 illustrates the HIL testbed employed for the experiments. Prior to the experiments, the MATLAB script of the offline-trained HEM is imported to the Embedded Coder App in

Simulink to generate C code. Then, using AURIX Development Studio IDE, the generated C code of the HEM is flashed to the 133 MHz, 32-bit TriCore AURIX TC234 (BMS microcontroller) from Infineon Technologies. To emulate the real-time BMS operations under varied discharging protocols of the LIB, the AURIX TC234 is interfaced with the Infineon TLE9012DQU and TLE9015DQU evaluation boards. The TLE9012DQU provides the emulated BMS inputs, i.e., LIB voltage, current and temperature; while the TLE9015DQU synchronises the UART communications between the AURIX TC234 and TLE9012DQU.

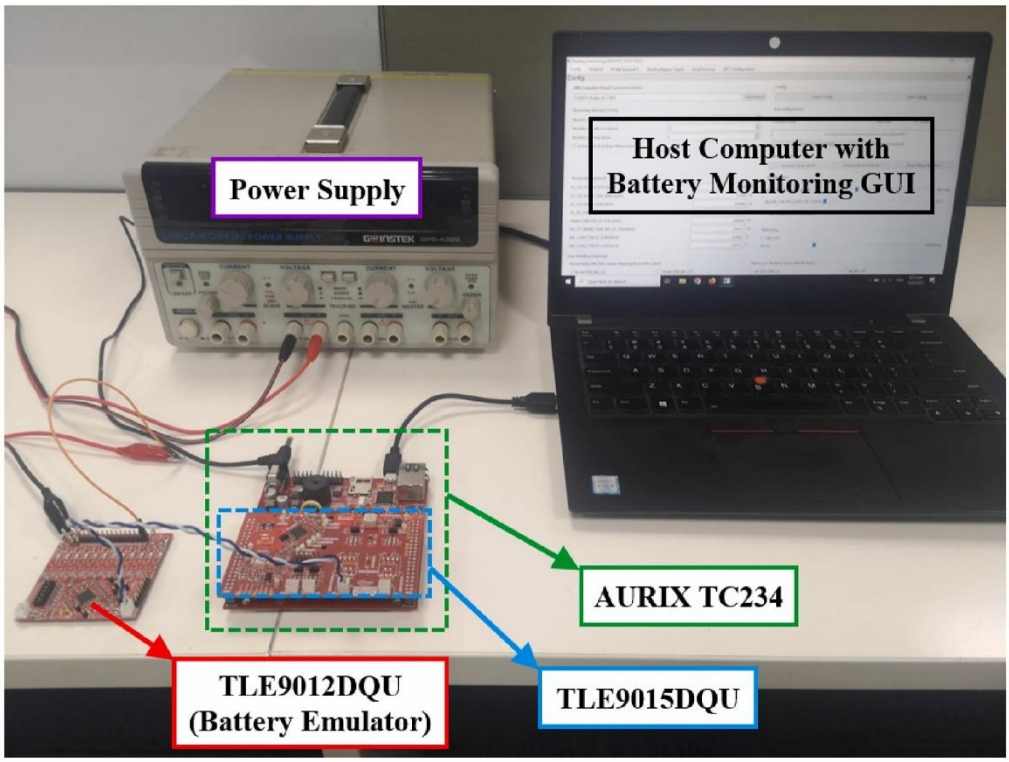

Figure 5.3. HIL testbed involving the AURIX TC234 (BMS microcontroller).

For experimental testing of the HEM, two of the WLTP datasets from Chapter 3 are utilised. Specifically, the open dataset of four NMC batteries (labelled B1 to B4), and the in-house dataset of four LFP batteries (labelled B5 to B8), are consecutively uploaded to the Infineon battery monitoring GUI in a host computer. Herein, the voltage, current and temperature signals are injected with random Gaussian white noise by using a signal-to-noise ratio of 30 dB, so as to match the real-life sensory conditions of the BMS [97]. The obtained signals are then transmitted from the host computer to the TLE9012DQU, via TLE9015DQU. A cut-off frequency of 2 kHz is chosen for the anti-aliasing filters

used in the two evaluation boards. With each data sample received from TLE9012DQU, the battery SOH is estimated online by the HEM-integrated AURIX TC234. Finally, the estimation results are transmitted back to the host computer for monitoring and control purposes. Table 5.1 presents the experimental parameters of the HIL testbed.

Table 5.1. Experimental parameters of the HIL testbed.

Parameter	Value
Dataset 1: NMC batteries (B1 to B4)	UMBL-NMC111
Nominal capacity of NMC batteries	5.0 Ah
Dataset 2: LFP batteries (B5 to B8)	APR18650M1-B
Nominal capacity of LFP batteries	1.1 Ah
Battery emulator/sensor	TLE9012DQU
Communications synchroniser	TLE9015DQU
Controller unit	AURIX TC234
Voltage range	[2.0, 4.2] V
Temperature range	[24, 32] °C
Signal-to-noise ratio	30 dB
Sampling frequency	1 kHz

While temperature is one of the key factors that influences battery SOH, this paper does not consider severe temperature variance for the following two reasons: 1) for many battery applications such as power grid and EV applications, the battery temperature can be well-regulated by the thermal management system [98]. 2) The ETSTI can be extracted from an extremely short time frame (< 0.1 s) where the temperature varies minimally at best. Such swift extraction can be easily supported by most BMSs since their sampling rate is in the milliseconds range [99], [100].

5.4.2 Description of the Test Cases

The LIB data (B1–B8) of the two datasets are used in the HIL testbed experiments, and the SOH estimation results are obtained via four-fold cross validation [21]. Specifically, three LIBs are routinely chosen from each dataset and their data are used as the offline training set for the HEM, whereas the unseen data of the remaining LIB is used as the HIL test set in each of the two cases described below (i.e., Case 1 and Case 2). The entire procedure is

repeated until all four LIBs have been used once as a HIL test set, as shown in Table 5.2. To study the estimation errors on a quantitative basis, the performance metric known as RMSE is applied.

Table 5.2. Validation procedure for each case.

Offline training set	HIL test set
NMC batteries B2, B3 and B4	NMC battery B1
NMC batteries B1, B3 and B4	NMC battery B2
NMC batteries B1, B2 and B4	NMC battery B3
NMC batteries B1, B2 and B3	NMC battery B4
LFP batteries B6, B7 and B8	LFP battery B5
LFP batteries B5, B7 and B8	LFP battery B6
LFP batteries B5, B6 and B8	LFP battery B7
LFP batteries B5, B6 and B7	LFP battery B8

Case 1 (Validation Under Specific Discharging Current): SOH estimation is performed under fixed discharging, whereby the discharging current of the tested LIB data is the same as that of the training data. Among each 1400 erratic sequences, the last one of each current is selected and the capacity is approximated as the coming reference cycle. The specific current is selected with minimum error on the validation data.

Case 2 (Validation Under Various Discharging Currents): SOH estimation is performed under variegated discharging, such that the discharging current of the tested LIB data can be stochastic or dynamic. In other words, the condition which involves the LIB operating at a specific current is not required. Among each 1400 erratic sequences, the last one is chosen, and the capacity is approximated as the coming reference cycle.

5.4.3 Correlation Analysis of the Proposed Health Indicator

Prior to the implementation of the two test cases, the efficacy of the proposed HI (ETSTI) in obtaining SOH estimates is quantitatively evaluated upon extraction. Spearman correlation coefficients (SCCs) [80] are therefore recorded in Table 5.3 to determine the most correlative ETSTI, using battery B1 to exemplify the correlation analysis. For each discharging current I_1 that has been selected, different values of the momentary voltage rise V_{rise} during the

LIB's transition from discharging to rest (within 0.04 s) are analysed until all the permissible voltage magnitudes are covered. Evidently, all the SCCs are very close to either –1 or 1, thereby denoting strong ties between ETSTI and SOH. The ETSTI extracted from both $V_{\text{rise}} = 0.12\ \text{V}$ and $I_1 = 2.25\ \text{A}$ is found to be the most correlative as the SCC is –0.998. Therefore, it is chosen for use in the experiments.

Table 5.3. SCC between ETSTI and SOH for battery B1.

V_{rise} (V) \ I_1 (A)	0.75	1.5	2.25	3	4.5
0.04	−0.979	−0.983	−0.990	−0.976	−0.970
0.08	−0.979	−0.986	−0.993	−0.977	−0.971
0.12	−0.985	−0.995	**−0.998**	−0.978	−0.972
0.16	−0.984	−0.988	−0.988	0.959	0.909
0.2	−0.964	−0.980	−0.983	−0.955	−0.911

Table 5.4. SCC between ETSTI and SOH at different time intervals.

Battery \ T (s)	0.02	0.04	0.06	0.08	0.09
B1	−0.923	**−0.998**	−0.989	−0.990	−0.946
B2	−0.939	**−0.997**	−0.993	0.992	−0.977
B3	−0.938	**−0.995**	0.994	−0.988	0.953
B4	−0.925	**−0.996**	−0.990	−0.991	−0.962
B5	0.930	**−0.998**	−0.997	−0.986	−0.971
B6	−0.948	**−0.995**	−0.991	−0.982	−0.958
B7	−0.930	**−0.997**	−0.995	−0.990	−0.945
B8	−0.944	**−0.998**	0.997	−0.981	−0.969

To further substantiate this inference, Table 5.4 demonstrates the scalability of the chosen ETSTI across various timed extractions (< 0.1 s) and LIBs. It is apparent that the scalability of the ETSTI still holds since all the recorded SCCs are very close to either –1 or 1, with 0.04 s evinced as the most ideal time interval for ETSTI extraction and practical usage in this chapter.

5.4.4 Complexity Profiling and Error Analysis

The computational complexity of an SOH estimator is a major technical concern in real-time BMS applications; notably, before and during the estimator's

deployment. Complexity profiling is therefore performed on the proposed HEM by utilising the HIL testbed, and the results are recorded in Table 5.5. The analysed parameters are the average model training and process time, Random Access Memory (RAM) usage, Flash memory usage, and multiply-accumulate (MACC) operations in 32-bit floating points (fp32). For the purpose of benchmarking, the results obtained from models that are intrinsic to the HEM (e.g., GPR), as well as the results obtained from extrinsic models, i.e., LSTM [55], GRU [54], ECM [83], SPM [26] and P2D [27], are individually recorded in the table and compared. Unlike the ML models which are trained offline using the extracted ETSTI, the ECM, SPM and P2D can only be directly modelled using the underlying physical principles of the NMC and LFP batteries. Hence, there is no training time recorded for these three physics-based models. All models are deployed in the AURIX TC234 for SOH estimation based on Case 1 and Case 2, respectively.

Table 5.5. Complexity analysis results of different methods.

Method	Avg. training time (s)	Avg. process time (ms)	RAM (kB)	Flash (kB)	MACC (fp32)
HEM	**27.64**	**0.12**	**0.08**	**4.93**	**10062**
AEM	86.52	0.25	0.30	25.73	18656
ELM	48.05	0.27	0.05	9.12	32695
GPR	71.34	0.36	1.46	35.79	93591
SVR	95.90	0.33	2.62	52.04	60337
DNN	93.11	0.29	1.41	84.06	76343
LSTM	139.28	0.44	3.95	119.27	124002
GRU	125.49	0.40	3.80	101.88	94048
ECM	–	0.64	8.64	253.92	251020
SPM	–	0.65	8.75	494.74	269113
P2D	–	0.78	11.91	705.80	385279

It is observed that the memory requirement of the proposed HEM is 5.01 kB (Flash and RAM combined), which is a tiny fraction of the useable memory (1096 kB) provided by the AURIX TC234. Furthermore, the process time of the HEM during online SOH estimation is only 0.12 ms on average. The sampling frequency applied is 1 kHz, which is adequately good for SOH estimation under highly stochastic scenarios such as EV usage. Therefore, each computational iteration must be completed within 1 ms and based on the HEM's process time,

only 12% of the CPU resources in the microcontroller is used. The other ten models are more resource-intensive, since their CPU usage range from 25% (AEM) to 78% (P2D). As with its total memory usage and process time, the number of MACC operations executed by the HEM (i.e., 10062) is also found to be the lowest among all the models listed in Table 5.5.

In the context of ML in embedded systems, MACC operations calculate the weighted sum of the input feature (e.g., ETSTI) and corresponding weights, which is a vital step in the computation of activations and predictions. A high number of MACC operations typically indicates that the ML model is complex and compute-intensive. Similarly, for physics-based models, a high number of MACC operations means more computational resources are required to perform mathematical modelling. On this basis, it is observed that the ECM, SPM and P2D use up to 97% more MACC operations than the HEM. The offline computation speed of the HEM is also the fastest among the experimental ML models, as evinced by its average training time of 27.64 s. In view of all the computation savings rendered by the HEM thus far, it can be ascertained that there is no bottleneck for real-time deployment of the HEM.

To further study the underlying causes of the HEM's limited consumption of resources during offline training and within the AURIX TC234, it is crucial to analyse the number of hyperparameters used for optimising its performance, since they can influence the computational load. More hyperparameters generally mean higher complexness of an ML model (e.g., increased model size), leading to a longer training duration and a slower on-board processing speed (i.e., more MACC operations and prolonged process time) whilst consuming more memory. Notably, more complex models require more RAM to store weights, intermediary variables, and decision boundaries during inference. The model size also affects Flash storage on a microcontroller. A model with many hyperparameters that increases its size (e.g., number of layers and neurons of a neural network) may not fit on the available storage of the microcontroller. However, it is possible to offset the quantity of required hyperparameters by employing a few optimal ones that not only simplifies the hyperparameter tuning process but also balances model performance with resource efficiency. This can be achieved through the implementation of a

powerful, hyperparameter optimisation technique such as multi-objective Bayesian optimisation (MOBO) [38], [101].

Table 5.6. Number of hyperparameters used for optimising each method.

Method	Number of hyperparameters
HEM	**7**
AEM	11
ELM	3
GPR	4
SVR	4
DNN	5
LSTM	7
GRU	7

Table 5.7. Optimisation scheme of each method employed in the HEM.

Method	Number of hyperparameters used for optimisation	Hyperparameter name(s) and configuration
DNN	2	Hidden layers = 3, Neurons per hidden layer = 10
ELM	2	Hidden neurons = 4 (first-level ELM), Hidden neurons = 8 (second-level ELM)
GPR	1	Length scale = 2
SVR	2	Regularisation parameter (C) = 10, Kernel type = RBF

As recorded in Tables 5.6 and 5.7, the HEM only requires seven hyperparameters to be tuned for it to perform optimally, which is a significant achievement given that certain single-model frameworks such as the LSTM and GRU require the same number of hyperparameters to be tuned. It is worth mentioning that in this paper, the selection and tuning of all the experimental ML models' hyperparameters is performed using MOBO. This automated technique is particularly useful for ensemble model frameworks, since it can help optimise for multiple competing objectives across multiple models simultaneously. Importantly, MOBO not only discovers the best-performing hyperparameter configurations but also helps prioritise and focus the search on the combination of hyperparameters that is most effective towards the ensemble model's

performance. The combination is directly influenced by the type and quantity of models used in the ensemble, as well as the chosen ensemble learning technique.

Due to the dual-level, diversified learning framework of the HEM, the final combination of hyperparameters obtained in Table 5.7 is simple yet highly effective. The number of hidden layers and neurons as well as the magnitude of length scale and regularisation parameter, are all in the scale of 2–10, which is significantly lower than the configurations (i.e., 18–56) adopted by the same hyperparameters of the other seven experimental ML models. As discussed, the size of an ML model corresponds to its complexity in terms of computational load and resource consumption. A greater quantity of tuning hyperparameters and a higher numeric configuration in each hyperparameter will collectively constitute a larger, more complex model. Notably, the HEM's second-level ELM employs more hidden neurons than the first-level ELM to model the higher-level, more complex interactions between the predictions of the first-level models (DNN, etc.). The increased number of neurons allows the second-level ELM to have the capacity to capture more complex patterns, higher-order relationships, and non-linearities including battery capacity regeneration trends, which is essential for enhancing the overall ensemble performance.

Table 5.8. RMSE (%) of SOH estimation results for Cases 1 and 2 based on different methods.

Battery	Case	HEM	AEM	ELM	GPR	SVR	DNN	LSTM	GRU	ECM	SPM	P2D
B1	1	**0.36**	0.65	1.09	0.94	0.74	0.72	1.11	1.19	1.64	1.76	1.15
	2	**0.50**	0.84	1.53	1.29	1.19	1.47	1.68	1.80	1.55	1.76	1.28
B2	1	**0.47**	0.91	0.60	1.25	1.06	0.98	1.19	1.07	1.50	1.70	1.24
	2	**0.61**	1.15	1.16	1.80	1.56	1.57	1.47	1.46	1.46	1.41	0.91
B3	1	**0.53**	0.75	0.92	0.98	1.15	1.11	1.25	1.54	1.56	1.69	1.31
	2	**0.72**	1.08	1.24	1.46	1.84	1.84	1.68	1.85	1.65	2.13	0.97
B4	1	**0.26**	0.49	0.55	0.75	0.80	0.78	0.96	1.76	1.24	1.09	0.92
	2	**0.31**	0.61	0.63	0.84	1.34	1.12	1.28	2.19	1.38	0.75	0.68
B5	1	**0.41**	0.74	0.82	1.17	0.90	0.58	0.81	1.43	1.25	1.61	1.23
	2	**0.58**	1.14	0.86	1.79	1.24	0.95	1.39	1.67	1.43	1.43	1.04
B6	1	**0.51**	0.69	1.01	0.92	0.83	0.75	0.95	1.30	1.43	1.34	0.81
	2	**0.69**	1.02	1.06	1.24	1.06	1.37	1.44	1.54	1.51	1.05	0.83
B7	1	**0.34**	0.62	0.76	0.93	0.94	0.44	0.89	1.01	1.62	1.45	0.97
	2	**0.49**	0.82	2.14	1.30	1.53	0.77	0.92	1.31	1.59	1.09	0.90
B8	1	**0.28**	0.47	0.57	0.84	0.75	0.85	0.96	1.25	1.27	1.08	0.87
	2	**0.29**	0.51	0.65	0.76	1.54	1.15	1.31	1.43	1.39	1.16	0.82
Average	1	**0.40**	0.67	0.79	0.97	0.90	0.78	1.02	1.32	1.44	1.47	1.06
	2	**0.52**	0.90	1.16	1.31	1.41	1.28	1.40	1.66	1.50	1.35	0.93

Table 5.8 compares the SOH estimation results of the HEM across the eight LIBs (HIL test sets), under Cases 1 and 2. As with the HEM, the other ML models are evaluated according to the validation procedure described in Table 5.2. Figures 5.4 and 5.5 illustrate the SOH-tracking ability of the HEM with the corresponding estimation curves. It is evident that the estimated SOHs can closely track the true SOHs, reporting a high estimation accuracy. For Case 1, the average RMSEs of the collective SOH estimation results are between 0.4% and 1.47%, in which the HEM's error (0.4%) is the lowest. As for Case 2, the average RMSEs are between 0.52% and 1.66%, in which the HEM's error (0.52%) is the lowest.

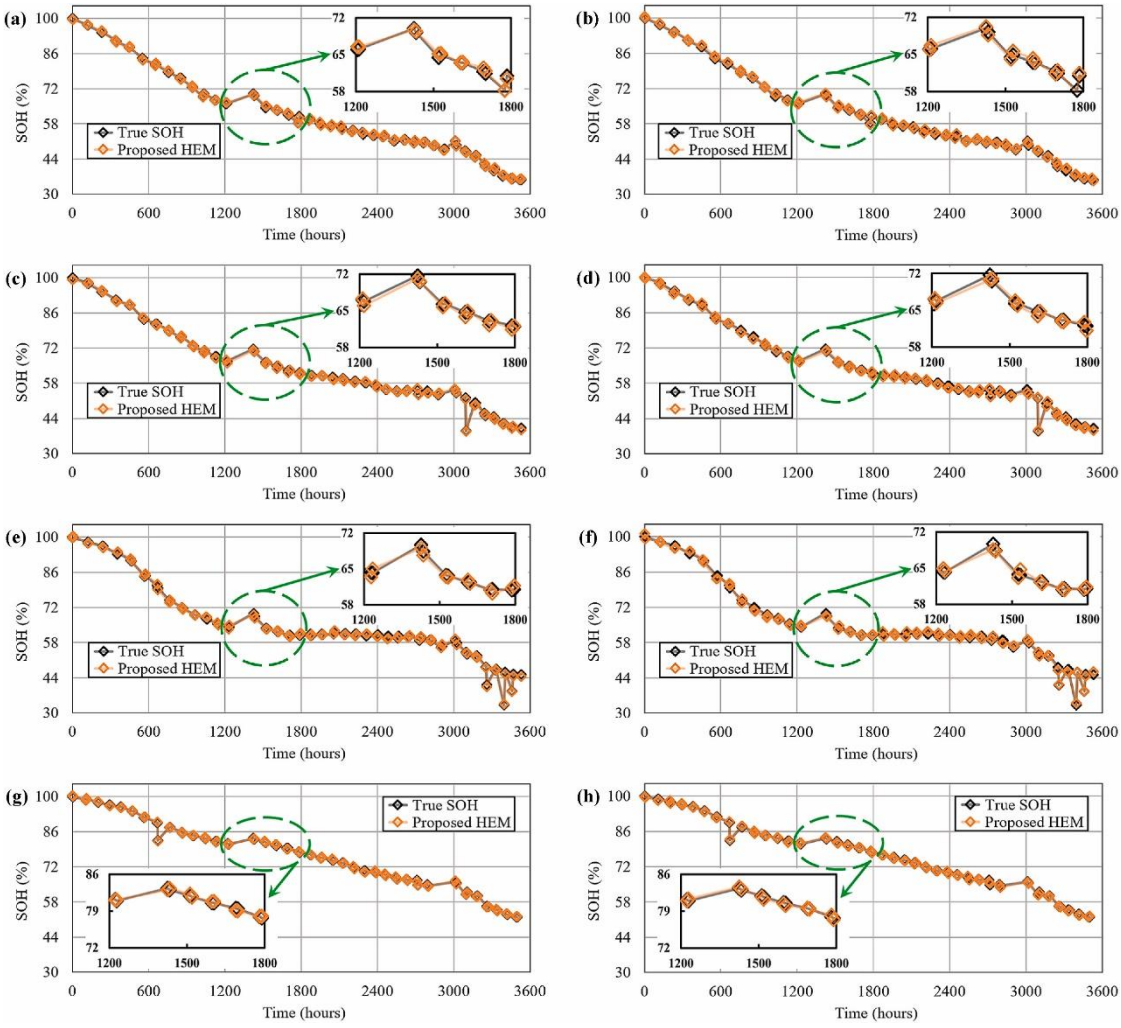

Figure 5.4. SOH estimation results of NMC batteries based on the proposed HEM. (a) SOH estimation results of B1 under Case 1. (b) SOH estimation results of B1 under Case 2. (c) SOH estimation results of B2 under Case 1. (d) SOH estimation results of B2 under Case 2. (e) SOH estimation results of B3 under Case 1. (f) SOH estimation results of B3 under Case 2. (g) SOH estimation results of B4 under Case 1. (h) SOH estimation results of B4 under Case 2.

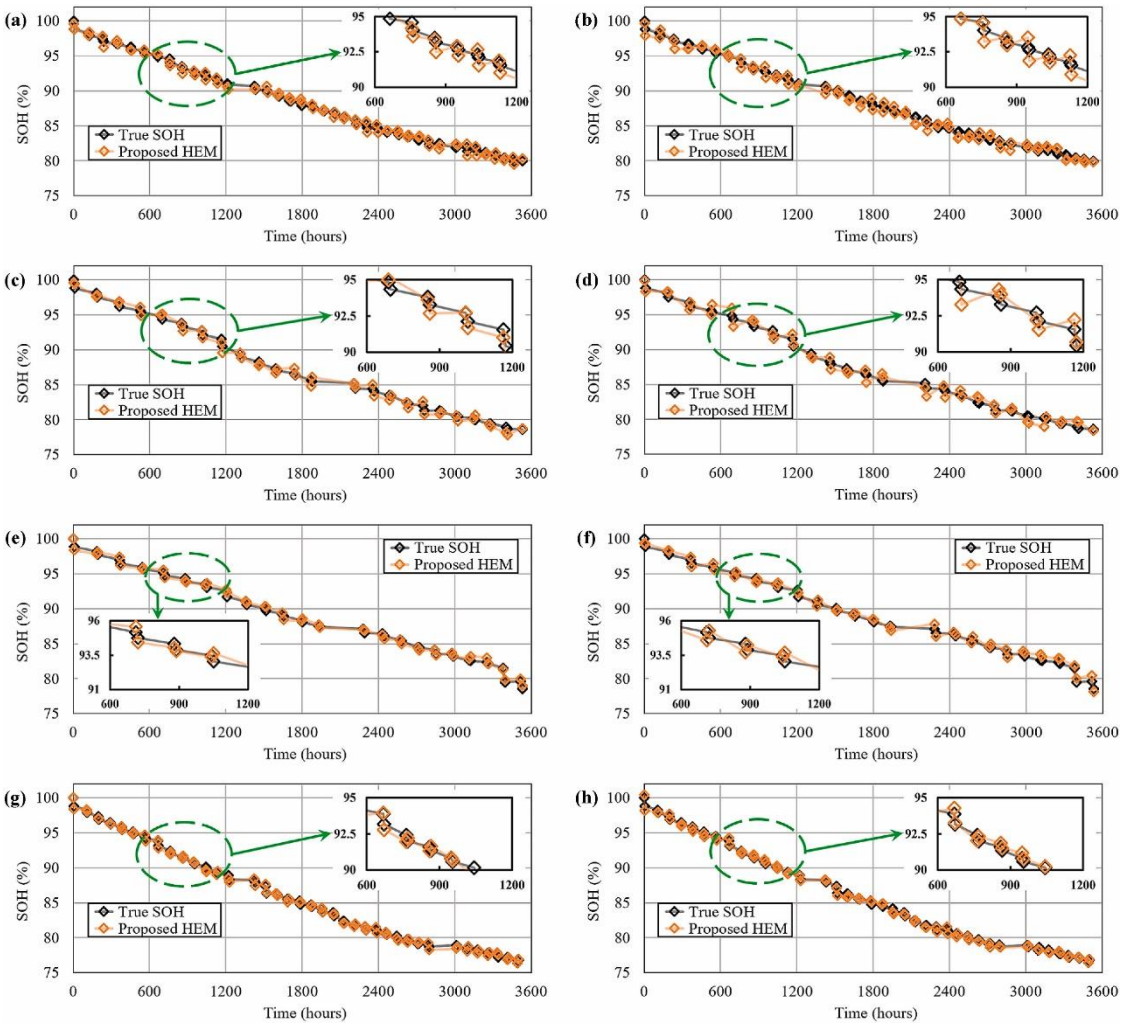

Figure 5.5. SOH estimation results of LFP batteries based on the proposed HEM. (a) SOH estimation results of B5 under Case 1. (b) SOH estimation results of B5 under Case 2. (c) SOH estimation results of B6 under Case 1. (d) SOH estimation results of B6 under Case 2. (e) SOH estimation results of B7 under Case 1. (f) SOH estimation results of B7 under Case 2. (g) SOH estimation results of B8 under Case 1. (h) SOH estimation results of B8 under Case 2.

The highest RMSEs of Cases 1 and 2 are mostly observed in the NMC batteries (B1 to B4), indicating that the experimental models generally perform better on the LFP batteries (B5 to B8). This is attributed by the battery capacity regeneration trends, which are more volatile in NMC chemistry. Still, the average SOH estimation accuracy of the HEM surpasses that of all other experimental models by at least 40%, due to its reciprocal traits, as stated in Section 5.3.5. It is worth emphasising that due to the truncated nature of the ETSTI (i.e., timed extraction < 0.1 s), dynamic parameters such as battery current and temperature can be seen as static. This also makes the ETSTI adaptable to the electrical inconsistencies [102], [103] which may occur across multiple,

interconnected batteries during charging and discharging operations.

Table 5.9. Comparative analysis results of different HEM variants.

HEM variant	Avg. training time (s)	Avg. process time (ms)	Average RMSE (%)
Proposed HEM	**27.64**	**0.12**	**0.46**
LSTM+ELM+GPR+SVR	59.39	0.30	0.67
DNN+LSTM+GPR+SVR	73.66	0.40	0.54
DNN+ELM+LSTM+SVR	64.05	0.36	0.59
DNN+ELM+GPR+LSTM	61.57	0.35	0.78
GRU+ELM+GPR+SVR	52.06	0.31	0.70
DNN+GRU+GPR+SVR	60.32	0.37	0.61
DNN+ELM+GRU+SVR	55.64	0.38	0.78
DNN+ELM+GPR+GRU	49.78	0.27	0.85
DNN+ELM+GPR	30.48	0.26	1.00
DNN+ELM+SVR	25.42	0.22	0.88
DNN+GPR+SVR	27.95	0.28	0.94
ELM+GPR+SVR	30.34	0.19	1.09
Combination of any 2 ML algorithms intrinsic to the proposed HEM	71.83–79.52	0.17–0.29	1.15–1.24
LSTM+GRU	110.91	0.53	1.36

To further validate the superiority of the proposed HEM under both test cases, the key performances elicited by various combinations of ML algorithms in its framework are averaged as a whole and studied in Table 5.9. The combination of distinct ML algorithms at the first level, coupled with the second-level ELM and the ETSTI, has given rise to different HEM variants. As elaborated in Sections 5.3.3 and 5.3.5, the ELM is an advanced, randomised learning algorithm and hence it is kept unchanged at the second level of each HEM variant to learn the first-level model outputs intelligently. It is discovered that by increasing the variety of ML algorithms used in the first level of a HEM variant, a higher SOH estimation accuracy (lower RMSE) is ensured, and with either LSTM or GRU incorporated, there will be at least a 44% increment in the average training and process time (i.e., computational cost) when compared to that of the proposed HEM. It should be noted that the incorporation of two or more identical ML algorithms in the first level will not necessarily yield better

overall performance in the HEM, as these algorithms may end up making similar estimates and not adding much diversity to the ensemble.

Table 5.10. Number of hyperparameters used for optimising each HEM variant.

HEM variant	Number of hyperparameters
Proposed HEM	**7**
LSTM+ELM+GPR+SVR	9
DNN+LSTM+GPR+SVR	15
DNN+ELM+LSTM+SVR	15
DNN+ELM+GPR+LSTM	14
GRU+ELM+GPR+SVR	13
DNN+GRU+GPR+SVR	14
DNN+ELM+GRU+SVR	13
DNN+ELM+GPR+GRU	10
DNN+ELM+GPR	12
DNN+ELM+SVR	8
DNN+GPR+SVR	11
ELM+GPR+SVR	9
Combination of any 2 ML algorithms intrinsic to the proposed HEM	7–11
LSTM+GRU	12

Table 5.10 records the number of tuning hyperparameters used by the HEM variants, and considering the corresponding results in Table 5.9, it is jointly evident that the proposed HEM enables the most optimal balance between computational efficiency and estimation accuracy. This is attributed by the matching characteristics of its first-level models, which eliminates the need for extensive tuning of each individual model and collectively, the models compensate for each other's shortcomings with fewer hyperparameters. Specifically, DNN captures complex non-linear patterns but may overfit and be slow to train. ELM provides a fast and simpler alternative, compensating for the DNN's overfitting and high computational cost. GPR offers smooth, probabilistic predictions and handles uncertainty well, compensating for noise and outliers that might affect SVR or DNN. SVR offers robustness against outliers and works well in high-dimensional spaces, where the DNN might struggle with overfitting. The second-level ELM learns to combine the predictions of the four, first-level

models in a way that optimises performance with minimal tuning. It is also observed that among the HEM variants, the proposed HEM is the least sensitive to hyperparameter choices since its combined predictions can smooth out individual model biases and errors.

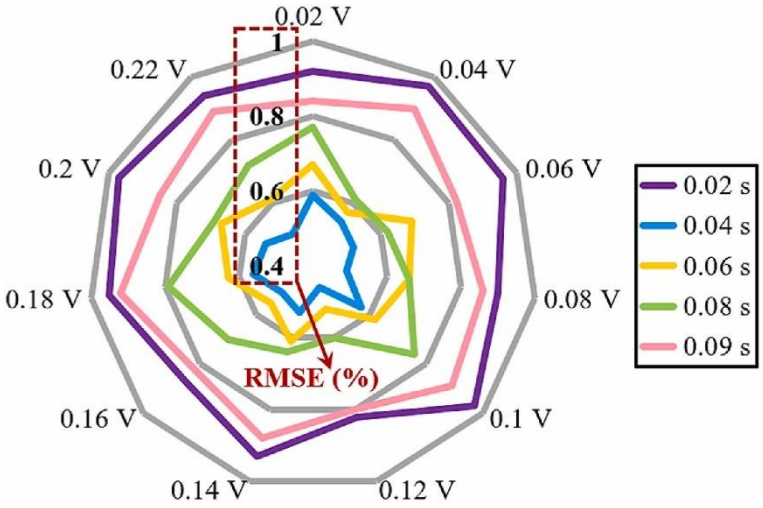

Figure 5.6. Average RMSE at various time intervals and momentary voltage rise.

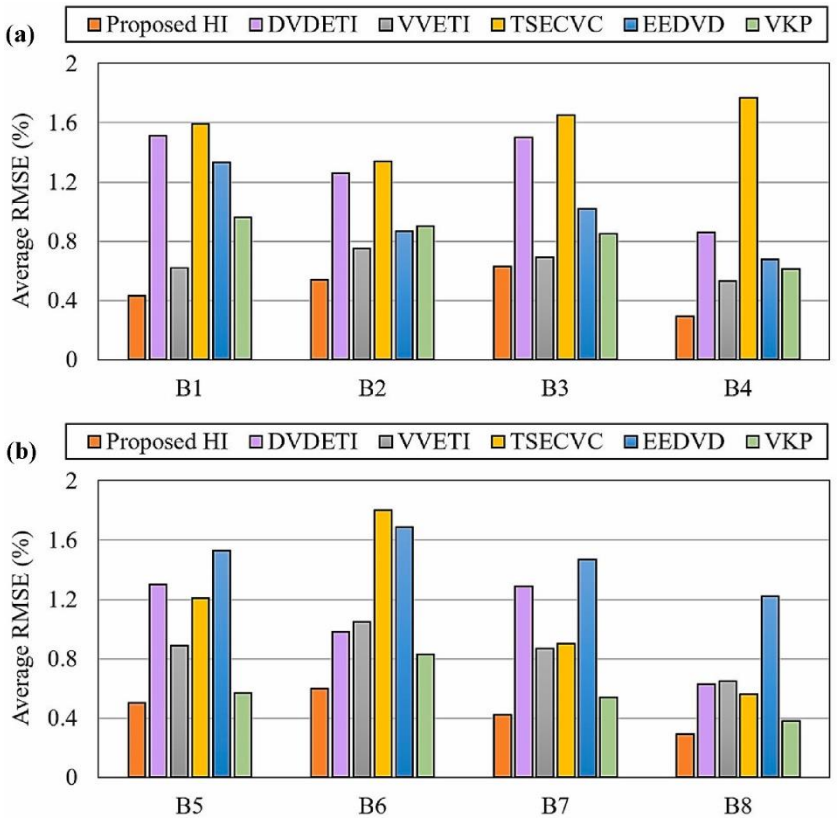

Figure 5.7. Error analysis results of different HIs. (a) Average RMSE for NMC batteries B1 to B4. (b) Average RMSE for LFP batteries B5 to B8.

Figure 5.6 demonstrates the robust estimation performance of the proposed HEM (< 1% RMSE) at various time intervals and voltages used for obtaining the input ETSTI. As with Table 5.9, the results demonstrated in Figure 5.6 have been averaged based on Cases 1 and 2, collectively. Herein, it is evident that the proposed HEM exhibits peak SOH estimation performance at 0.04 s and 0.12 V, respectively; in which the corresponding RMSEs are all between 0.46% and 0.82%. Such observation substantiates the SCCs recorded in Tables 5.3 and 5.4, where the most correlative ETSTI was identified for use. Increasing either the time interval (0.04 s) or momentary voltage rise (0.12 V) generally compromises the estimation accuracy, and with a time interval of 0.02 s, the accuracy of the HEM is sharply reduced. Even so, the maximum RMSE observed in Figure 5.6 is only 0.97%. To further validate the superiority of the proposed HI (ETSTI), it is also compared against five cutting-edge HIs discussed in Chapter 2 by using the HEM as the common training algorithm, and the SOH estimation results are summarised in Figure 5.7. Evidently, the proposed HI enables the highest estimation accuracy (i.e., RMSEs below 0.7% on average) while the other five HIs require a much longer, timed extraction (≥ 300 s).

5.5 Conclusion

This chapter has proposed a momentary informatics-centric, data-driven method based on a momentary HI and a hierarchical-ensembled ML model for online SOH estimation of LIBs under dynamic discharging. Extracted from a very short duration (< 0.1 s), the HI, named ETSTI, is exceptionally easy to derive and therefore applicable under various discharging currents. Since the ETSTI is both a singular and a truncated feature, filtering is not required; thereby minimising the computational cost. To validate the proposed method's effectiveness, dual-case HIL tests involving a BMS microcontroller are performed using various LIBs and SOH estimation models.

The experimental results show that the ETSTI is highly effective in denoting SOH as the obtained RMSEs are all below 2.2% for the tested ML models. Appropriate ETSTI extraction, coupled with the proposed ensemble model, has consumed only 12% of the processor resources and the RMSEs have all

become less than 0.8%. Through intelligent, stochastic-based learning of model weights across the DNN, ELM, GPR and SVR, the proposed method enables much faster computation speed as compared to both single-model and average ensemble model frameworks. The key limitation of this method is that it may be unviable for BMSs with slow measurement rate, as the ETSTI is designed to be sampled and processed within a very short time span. On the flip side, variables such as battery current and temperature can be seen as static when the timed extraction of the ETSTI is below 0.1 s.

Chapter 6

LLM-assisted Distilled Lifelong Learning Model for SOH Estimation Under Variable Conditions

The methods in the previous two chapters can only be more robust to both noisy and incomplete data at the cost of complexity and interpretability, especially when dealing with different LIB chemistries across varied operations of the battery. Considering this issue, coupled with the recent technological breakthrough of large language models (LLMs), this chapter exploits the strong generalisation capability of the generative pre-trained transformer-4 (GPT-4) for SOH estimation under variable conditions. Since battery data usually arrives sequentially with varied distribution in the real world, the teacher-to-student model-based distillation of knowledge and lifelong learning (LL) are incorporated into GPT-4 to estimate SOH adaptively with minimal fine-tuning. The real-time accuracy and computation performance of the proposed method is validated on an EV application-oriented embedded system.

6.1 Introduction

As is common in many of the existing ML models, a sizeable amount of data is required for their offline training, thereby prolonging the training duration. Moreover, in practice, the training data and test data may have different distributions, whereby the data labels of the battery training set are limited, and the data acquired from different battery types or at the different charging/discharging conditions, are usually inconsistent. This means that an ML model trained on a prior set of data labels might not be fully compatible with the new scenario data, even with the aid of transfer learning (TL) techniques [104].

In contrast to TL, lifelong learning (LL) [105] is dynamically evolving, which enables DL models to continuously learn by processing incoming non-stationary data from a data stream. However, with the introduction of new time-series data, the models may forget previously learned information, which leads to a degradation in performance on earlier tasks. In recent literature, LLMs such as

PaLM-2 [106] and GPT-4 [107] have shown exceptional flair for natural language and generic time-series analyses. In this regard, it is worth exploring whether the powerful generalisation capability of an LLM can be migrated to a univariant, supervised regression problem such as battery SOH estimation.

This chapter proposes a novel GPT-based framework that enables cross-battery SOH estimation. For the first time ever, the language-based perceptivity of the GPT-4 is converted to LIB data-based by only retraining its input and adaptors on selected LIB labels, since modifying and training the entire model on vast, labelled datasets is impractical. LL is applied to exploit the incrementally acquired unlabelled data, adapting the GPT-4 to the real-world scenario where an LIB undergoes temporal aging via charging/discharging. This reduces the errors amassed from temporal distribution shifts of LIB data over long periods, while previously learned information is retained by distilling the pre-trained GPT-4's knowledge into a student learner. Besides, the real-time viability of the proposed method is verified using a BMS microcontroller that incorporates three different WLTP datasets.

6.2 Proposed Method

Figure 6.1 illustrates the proposed SOH estimation framework, which comprises of offline training and online application. In the offline phase, the HI is first extracted from historical data [77], [78] and a teacher model is pre-trained to map the relationship between the HI and SOH. Then, the vital knowledge is distilled into a student model and during which, the model is minimally trained on existing unlabelled data and periodically fine-tuned. In the online phase, the student model is deployed with its input HI obtained from real-time measurements of raw LIB data. Whenever the student model encounters new, unlabelled LIB data (i.e., a new task) that is adequately dissimilar to a previous learned task, it will attempt to "learn" the data by autonomously expanding its network; whereas the knowledge of previous learned tasks is retained by "freezing" specific components of the network. Herein, the model's ability to generalise its knowledge to new tasks that it has not been explicitly trained on is termed as "zero-shot adaptation". Finally, the estimated SOH is obtained at the output of the student model.

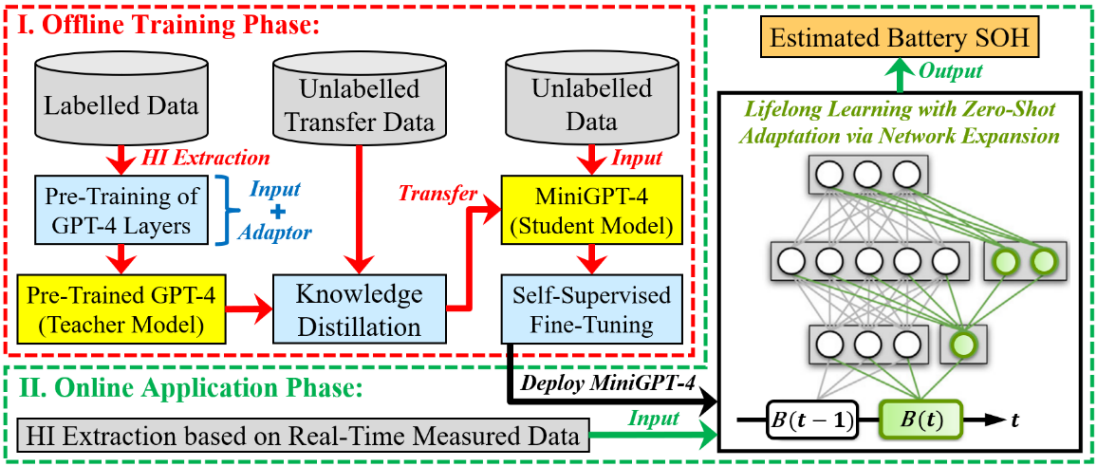

Figure 6.1. LLM-assisted framework of the proposed SOH estimation method.

6.2.1 Extraction of Health Indicator from Partial Charging Data

With reference to Eq. (1.2), the battery SOH formula can be reformatted to Eq. (6.1) as shown below. It is expressed as the ratio between the capacity at the s^{th} cycle (Q_s) and the nominal capacity (Q):

$$SOH_s = \frac{Q_s}{Q} \times 100\% \tag{6.1}$$

During the CC charging process of a battery, the measured voltage $V(t)$ and current $I(t)$ are typically stored by the BMS at every time step. Given a voltage sampling window, the partial charging data at the s^{th} cycle is described as:

$$q_i^s(V) = \int_{V_{min}}^{V_{min}+i\Delta V} |I(t)|dt, i \in \{0,1,\cdots,K\} \tag{6.2}$$

The cycle's charging feature $q_i(V)$ is obtained by spatially interpolating the voltage sampling window with step ΔV from V_{min} to $V_{min} + K\Delta V$. Then, it is expanded to a one-dimensional vector and normalised with the nominal capacity Q in order to adapt it to different LIBs. On this basis, the HI is expressed as:

$$\text{HI} = q^s(V) = [q_0(V), q_1(V), \ldots q_K(V)]/Q \tag{6.3}$$

The battery capacity-based SOH is modelled with the extracted HI, as described by Eq. (6.4). Herein, h represents the ML model that directly maps the relationship between the HI and SOH;

$$SOH_s = f(q^s(V)) = f(g(\text{HI})) = h(\text{HI}) \tag{6.4}$$

A D-labelled sample set $D = \{(x_1, y_1), (x_2, y_2), \ldots, (x_D, y_D)\}$ is introduced for pre-training of the GPT-4, where x denotes the HI and y is the target SOH label. The fine-tuning dataset contains only U unlabelled data $U = \{x_1, x_2, \ldots, x_U\}$, which arrives sequentially as the operating LIB ages over time. The labels are inaccessible due to incomplete discharging of the LIB in real-world application (e.g., EV), thereby rendering difficulty in supervised fine-tuning. In spite of this, the partial charging curve of the first cycle (i.e., fresh LIB state) is easily attainable for use as a HI, since SOH ≈ 100%. Partial charging curves capture the battery's behaviour over a smaller SOC range, which is often where the most sensitive changes in capacity occur. This enables more precise identification of battery health issues such as capacity fade and voltage drops, which can be less visible in a full charge cycle.

6.2.2 Layer-Wise Adaptive Training of GPT-4 (Teacher Model)

The pre-training process of the GPT-4 is made efficient and sustainable by freezing its trained, multi-head attention (MHA), normalisation and feedforward layers while only retraining its input and adaptor layers. Since the MHA, normalisation and feedforward layers hold the most knowledge [107], [108], freezing them would migrate the GPT-4's generalisation capability from language to downstream tasks. Linear probing is applied on the input layer to minimise external computations. Figure 6.2 describes the architectural workflow of the proposed method, where it is worth noting that the input layer employs a text vectorisation technique known as embedding, to convert the text specifications of the LIB into processable data. Herein, each of the chosen specifications (chemistry, etc.) is encoded into a unique, one-dimensional binary vector, allowing it to be logically processed.

The model performance on downstream tasks is maximised with ease by using battery-specific adaptors that incorporate each LIB's vectorised text specifications for battery-specific fine-tuning. For the l-th $l \in [1, D]$ adaptor layer, the input $H_{\mathrm{A}}^{l} \in \mathbb{R}^{(m+n)\times d}$ is formed by vertically concatenating the hidden features $\widetilde{H}_{\mathrm{P}}^{l} \in \mathbb{R}^{m\times d}$ from the l-th pre-trained layer and the vectorised text specifications of battery $H_{\mathrm{A}}^{l} \in \mathbb{R}^{n\times d}$ from knowledge. The length of the model input sequence and knowledge piece are denoted by m and n, respectively,

while d is the hidden size. Vital query information is obtained through a learnable gate function that filters the hidden features, namely:

$$H_{\mathrm{A}}^{l} = \left[\widetilde{H}_{\mathrm{P}}^{l} \odot \sigma(G); H_{\mathrm{A}}\right] \tag{6.5}$$

Given the input H_{A}^{l}, the adaptor layer projects it down to the r dimension with a fully connected (FC) layer. Both the battery knowledge and the query information from the model are then merged using a self-attention layer. A second FC layer projects H_{A}^{l} up to the original dimension d, and finally, the output $\widetilde{H}_{\mathrm{A}}^{l}$ is fed to the normalisation layer through a residual link. For each distinct LIB, a separate, battery-specific adaptor is employed to augment the fine-tuning performance.

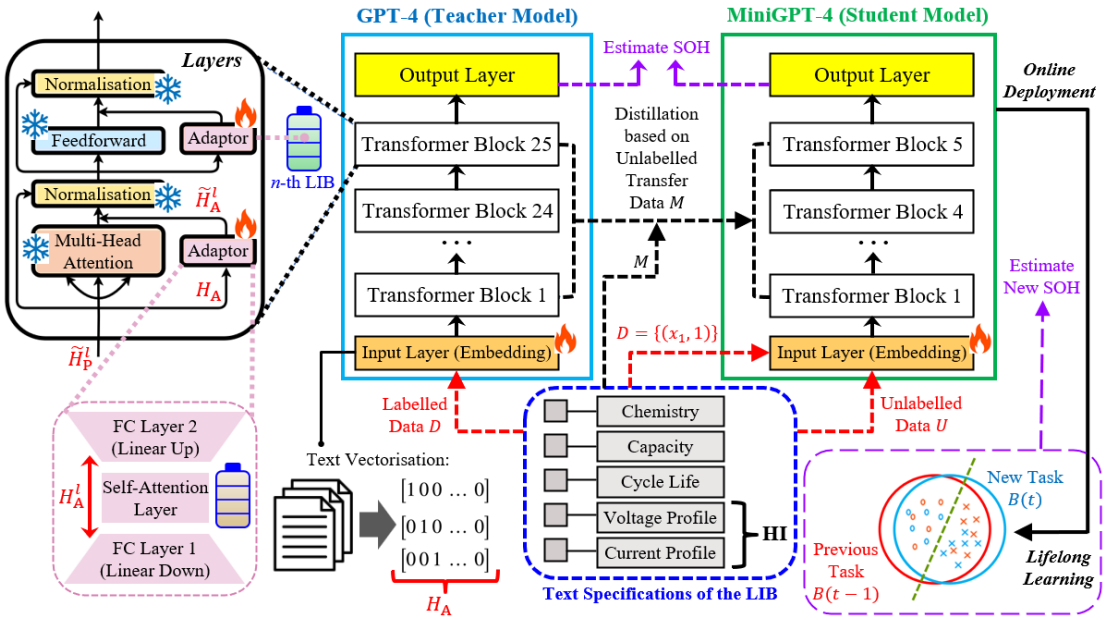

Figure 6.2. Teacher-student model architecture of the proposed method.

6.2.3 Pre-Trained Distillation and Lifelong Learning

To streamline the vast, learned knowledge of the teacher model (GPT-4), a simple ML technique for building compact yet accurate models, named pre-trained distillation, is first proposed, as described by Lines 1 to 7 in Algorithm 1. It operates in three steps using a student model (MiniGPT-4) as follows: 1) pre-train on unlabelled data U, 2) update knowledge base in respect of knowledge distilled from the teacher model, and 3) fine-tune on the first-cycle label to ensure model robustness against potential mismatches between the distribution

of the labelled data D and the unlabelled transfer data $M = \{x'_1, \ldots, x'_M\}$. It is worth mentioning that during distillation, the teacher model transfers knowledge to the student model by exposing its label predictions for instances x'_M.

Algorithm 1: Distilled Lifelong Learning (DLL)

Require: Teacher model Ω, student model θ, labelled data D, unlabelled transfer data M, unlabelled data U

1: Initialise θ by pre-training on U
2: **for each** $x \in M$ **do**
3: Get loss $L \leftarrow -\sum_y P_\Omega(y \mid x) \log P_\theta(y \mid x)$
4: Update student model $\theta \leftarrow \text{BACKPROP}(L, \theta)$
5: **end for**
6: Fine-tune θ with first-cycle label, where $D = \{(x_1, 1)\}$
7: **return** θ
// Given that tasks $B(0), \ldots, B(t-1)$ have been learned
8: Recruit free nodes for $B(t)$ and unfreeze new weights
9: Freeze the weights of previous tasks to retain learned knowledge
10: Initialise weights from prior nodes to newly recruited nodes via network expansion (forward transfer)
11: Generalise on the data of new task $B(t)$ to minimise Eq. (6.6)

The second part (Lines 8 to 11) of Algorithm 1 applies LL via the strategic and flexible expansion of the GPT network. If the new task $B(t)$ is marginally similar to the previous task $B(t-1)$, positive transfer is expected from $B(t-1)$ to $B(t)$. If the similarity is high, the expansion volume for $B(t)$ will be smaller. The degree of similarity between the two tasks is assessed by calculating the distance between their respective feature distribution, through the maximum mean discrepancy (MMD) test [107]. If both tasks exhibit a trace of similarity, their feature distributions will be close, leading to a low MMD score that ranges from 0 (perfect similarity) to 4 (marginal similarity). The performance of the student model is augmented by minimising the new loss function:

$$L_{\text{new}}(w) = L_B(w) + \sum_i b_i \left(w_i - w_i^{\text{target}}\right)^2 \tag{6.6}$$

where a hyperparameter b controls how flexibly the weights can be adjusted during gradient descent. Each network weight, w_i, is linked to a consolidation

value of $b_i \geq 0$. Here, w_i^{target} is the target weight value. Notably, a large b_i causes changing w_i away from w_i^{target} to be strongly penalised during LL. When $b_i = \infty$, these weights are deemed "frozen". Correspondingly, w_i is viewed as masked during backpropagation and prevented from changing to boost efficiency. In contrast, $b_i = 0$ indicates that w_i is free to change, i.e., it is "unfrozen". This allows an obsolete learned task to be forgotten through unfreezing, since the expanding network may eventually reach a threshold where it is unable to provide free nodes to learn a new task well. In summary, the MMD-quantified task similarity influences b_i to freeze or unfreeze weights and whether network expansion is required. When MMD > 0, new weights become unfrozen and the learned weights are frozen to trigger network expansion.

6.3 Testing Results and Discussion

6.3.1 Embedded System Testbed Description

As with the HIL experiments in Chapter 5, the proposed method is demonstrated on the 133 MHz, 32-bit TriCore BMS microcontroller known as the Infineon AURIX TC234. Before testing, the offline-trained student model is imported to the Embedded Coder App in Simulink to generate C code. The C-script is then flashed to the AURIX TC234 for deployment. This test employs all three WLTP datasets described in Chapter 3. Collectively, the datasets cover three popular LIB chemistries (i.e., NCA, LFP and NMC) with nominal capacities ranging from 1.1 Ah to 5 Ah. For each dataset, the model is evaluated using *k*-fold cross validation [91] for each of the following two cases: 1) SOH estimation under fixed current profile, and 2) SOH estimation under dynamic current profile. Notably, as with the cross validation procedure described in Chapters 4 and 5, an unseen LIB from each dataset is used as the test data while the rest of the LIBs are used as the training data.

6.3.2 Validation Test Results

Figure 6.3 exemplifies the robust SOH estimation ability (RMSEs < 1%) of the proposed method with the estimation results obtained from three unseen LIBs that are of different chemistry. The corresponding, averaged test results such

as memory usage, MACC operations in 32-bit floating points (fp32), computation time, and RMSE, are recorded in Table 6.1 as benchmarks against the test results obtained from six other methods. They include the classic GPT-4 [107], TL-integrated GPT-4 [102], and the widely used, TL-integrated LSTM [104], XGBoost [93], GPR [44], and SVR [48].

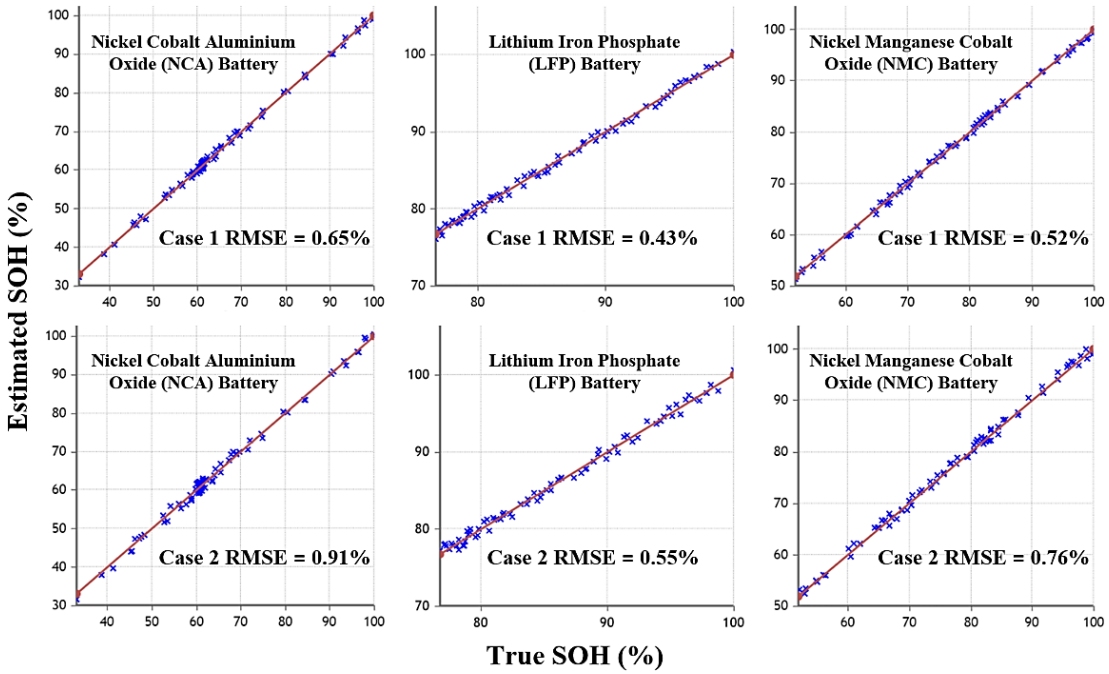

Figure 6.3. SOH estimation results for the three LIBs under Cases 1 and 2. The red diagonal line denotes a perfect match between the estimated and true SOH.

Table 6.1. Comparative analysis results (averaged across Cases 1 and 2).

Method	RMSE (%)	RAM (MB)	Flash (MB)	MACC (fp32)	Training Time (s)	Process Time (ms)
Proposed	**0.64**	**0.01**	**0.13**	**2689**	**53.06**	**0.15**
GPT-4	1.22	0.07	0.74	9620	2104.45	0.72
GPT-4+TL	0.98	0.04	0.59	7447	934.01	0.41
LSTM+TL	1.53	0.02	0.20	4758	391.63	0.25
XGBoost	1.59	0.08	0.61	5812	584.16	0.32
GPR	1.85	0.10	0.73	6824	750.04	0.40
SVR	2.06	0.05	0.48	5395	472.56	0.27

Evidently, the proposed method consumes the least memory (0.14 MB in total) and based on its process time and the sampling frequency (1 kHz), only 15% of the CPU resources in the microcontroller is utilised; whereas the other methods utilise up to 72% of the resources. This is attributed by the condensed size and

parameters of the student model, wherein the minimised, weighted sum of the input HI and corresponding model weights is only 2689 (fp32). The proposed method also exhibits the highest estimation accuracy (average RMSE = 0.64%) with the least training, since the student model does not need to learn the full complexity of new tasks on its own but is instead guided by the teacher model's knowledgeable outputs during distilled lifelong learning (DLL); hence negating the need to retrain from scratch. Figure 6.4 demonstrates the robust estimation performance (RMSEs < 2%) of the proposed method when incorporating different HIs derived from different LIB operating conditions, in which the proposed HI yields the best results due to its strong correlation with SOH.

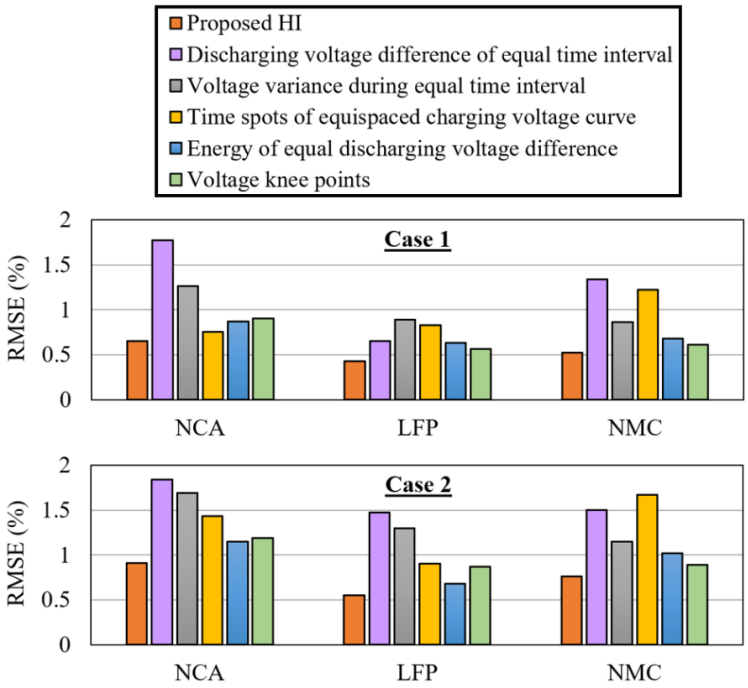

Figure 6.4. Error analysis results of different HIs for the three LIBs under Cases 1 and 2, where the DLL-integrated GPT-4 is used as the common training algorithm.

6.4 Conclusion

This chapter has proposed a novel LLM-based, SOH estimation method that exploits the strong generalisation prowess of GPT-4 when integrated with DLL. Importantly, DLL is robust against data shifts and noise as it continuously updates the GPT model and retains vital knowledge. The proposed method is computational resource-efficient and highly precise when estimating the SOH of various LIBs under two practical-use cases with a BMS microcontroller.

Chapter 7

Conclusion and Future Works

7.1 Conclusion

Accurate battery SOH estimation is highly vital for expediting the development and optimisation of BMS software, as well as ensuring the safe and reliable operation of ESSs, such as EVs. This thesis focused on the data-driven ML methods for LIB health prognostics in automotive applications. In Chapter 2, a comprehensive review of the existing SOH estimation methods was conducted with an emphasis on data-driven approaches involving battery HIs. It was found that most of the existing HIs are designed for conditions of CC charging/discharging at a specific rate over a long duration, which heavily limit their real-world applicability. Moreover, the existing ML models used for HI and SOH mapping are not state-of-the-art, and thus, more advanced ML models and HIs need to be developed to improve the robustness of online SOH estimation.

Chapters 4, 5 and 6 address the existing challenges in SOH estimation by introducing three novel, data-driven ML methods that can be implemented in different scenarios.

The method in Chapter 4 can be applied at different discharge rates which mainly involve randomised discharging. The voltage range required for the extraction of the proposed VDTTI is flexible. A shorter time interval (< 110 s) can be employed to extract the VDTTI for use in dynamic battery operations, but not without the cost of slight accuracy sacrifice. Unlike traditional ML models, the proposed, stacked LSTM structure offers a simple yet effective learning solution that requires fewer tuning hyperparameters and expedites training. The test results show that robust SOH estimation performance is achieved without any additional hardware or system downtime.

The method in Chapter 5 can be applied under dynamic discharging currents, where the currents may undergo rapid change within an extremely short time. The rationality of the proposed ETSTI is to indirectly reflect battery internal ohmic resistance, and it can be extracted from an extremely short interval (< 0.1 s) when the battery momentarily transits from discharging to rest, given that

most of the existing SOH estimation methods are designed for a lengthy CC charging/discharging process without accounting for the volatility of an EV's regenerative braking. The highly truncated nature of the ETSTI makes it exceptionally easy to implement under various currents and SOC levels, whilst removing the need for filtering. The HEM comprising of four popular ML algorithms, i.e., DNN, ELM, GPR and SVR, is proposed to efficiently learn the relationship between ETSTI and SOH via momentary informatics. The proposed method exhibits superior real-time capability in a BMS microcontroller when experimentally verified against various LIBs, HIs and SOH estimation models.

The method in Chapter 6 can be applied in various conditions which include varied battery chemistry, partial charging, fixed current, and dynamic current. It integrates GPT-4 within a DLL framework that adopts a teacher-student model structure for SOH estimation, based on the HI extracted from partial charging data of an EV. Knowledge distillation is applied to transfer information from the teacher model with the aid of unlabelled LIB data, thereby guiding the training of the student model. Then, an LL strategy is applied to optimise the model's performance over time. The proposed method is found to be resource-efficient and highly accurate when estimating the SOH with a BMS microcontroller.

7.2 Future Works on SOH Estimation

In spite of the aforementioned studies, there is still room to improve and further validate the practicality of the novel methods proposed in thesis. For instance, taking into account the electrical inconsistencies which may occur across multiple, interconnected LIBs (i.e., an EV battery pack) during charging and discharging operations. Another viable possibility is to integrate cloud-edge technology with LLMs (e.g., GPT-4) for battery SOH estimation, since edge devices can handle real-time data processing while the cloud provides powerful computation for model rectification. Correspondingly, through the deployed LLM, both user interaction and understanding of battery health can be achieved in the form of explainable artificial intelligence. These future works are elaborated in the following sub-sections.

7.2.1 Pack-Level SOH Estimation Considering Battery Inconsistencies

A battery pack is composed of multiple individual battery cells that are typically arranged in series and parallel configurations, so that they can cohesively operate as a singular, high energy density unit. Each cell has its own unique traits, such as internal resistance, capacity, voltage, and degradation rate. While these cells may be nominally identical, there are always intrinsic variations in their performance due to manufacturing tolerances, aging, and operational conditions (e.g., temperature and charge/discharge cycles). Due to such inconsistencies, a single weak or failing cell can adversely affect the performance of the entire battery pack; most notably in the form of reduced overall capacity and faster degradation rate. It is henceforth crucial to improve the existing data-driven methods to provide accurate pack-level SOH estimation, which as a result will enable timely maintenance or replacement of cells before they cause major issues. This is important for applications like EVs, where the pack's performance directly influences the vehicle's range, safety and reliability.

7.2.2 Integrating Cloud-Edge Technology with Large Language Model

As opposed to using conventional ML models for battery SOH estimation, it is recommended to employ LLMs instead, as they could potentially bring about several major advantages, especially if paired with edge devices and the cloud infrastructure. Firstly, LLMs can help interpret complex data patterns by analysing vast volumes of battery monitoring logs and specifications, providing insights or generating summaries of battery HIs. Secondly, with edge computing, the data can be processed locally on devices close to the sensors in the battery pack, thereby reducing the latency and bandwidth usage while enabling real-time, health monitoring and performance-tracking of the cells. Lastly, cloud computing provides scalable storage and computational power for more resource-intensive tasks, such as running large-scale analyses (e.g., in-situ battery aging data analytics for HI extraction) and training an LLM. It is worth mentioning that careful consideration of data security, latency, and resource optimisation is essential for this integration to be a success.

Author's Publications

Journal Publications:

1) **W. Q. T. Poh**, Y. Xu, and R. T. P. Tan, "Data-Driven Estimation of Li-Ion Battery Health: Integrating GPT-4 With Distilled Lifelong Learning," *IEEE Trans. Energy Convers.*, vol. 40, no. 2, pp. 1682–1685, Jun. 2025, doi: 10.1109/TEC.2025.3548400.

2) **W. Q. T. Poh**, Y. Xu, W. Liu, and R. T. P. Tan, "Momentary Informatics based Data-Driven Estimation of Lithium-Ion Battery Health Under Dynamic Discharging Currents," *J. Power Sources*, vol. 629, pp. 236041, Feb. 2025, doi: 10.1016/j.jpowsour.2024.236041.

Conference Publications:

1) **W. Q. T. Poh**, Y. Xu, and R. T. P. Tan, "Data-Driven Estimation of Li-Ion Battery Health using a Truncated Time-based Indicator and LSTM," in *2023 IEEE Power & Energy Soc. General Meeting (PESGM)*, Orlando, FL, USA, Jul. 2023, pp. 1–5, doi: 10.1109/PESGM52003.2023.10252352.

2) **W. Q. T. Poh**, Y. Xu, and R. T. P. Tan, "A Review of Machine Learning Applications for Li-Ion Battery State Estimation in Electric Vehicles," in *2022 IEEE PES Innovative Smart Grid Technologies – Asia (ISGT Asia)*, Singapore, Nov. 2022, pp. 265–269, doi: 10.1109/ISGTAsia54193.2022.10003481.

Bibliography

[1] K. Maalej, S. Kelouwani, K. Agbossou, Y. Dubé, and N. Henao, “Long-trip optimal energy planning with online mass estimation for battery electric vehicles,” *IEEE Trans. Veh. Technol.*, vol. 64, no. 11, pp. 4929–4941, Nov. 2015.

[2] C. Chen and S. Duan, “Microgrid economic operation considering plug-in hybrid electric vehicles integration,” *J. Modern Power Syst. Clean Energy*, vol. 3, no. 2, pp. 221–231, Jun. 2015.

[3] J. Wu, X. Cui, H. Zhang, and M. Lin, “Health prognosis with optimized feature selection for lithium-ion battery in electric vehicle applications,” *IEEE Trans. Power Electron.*, vol. 36, no. 11, pp. 12646–12655, Nov. 2021.

[4] J. D. Power, “Global EV sales from 2014 to 2023,” *ev-volumes.com*. https://ev-volumes.com/news/ev/global-ev-sales-for-2023/ (accessed Jul. 16, 2024).

[5] Navigant Research, “Total vehicle li-ion battery revenue by region, World Markets: 2015-2024,” *electriccarsreport.com*. https://electriccarsreport.com/2015/08/market-for-li-ion-electric-car-batteries-to-reach-30b-in-2024/ (accessed Jul. 16, 2024).

[6] International Energy Agency, “Global EV outlook 2024,” *iea.org*. https://www.iea.org/reports/global-ev-outlook-2024 (accessed Jul. 19, 2024).

[7] G. Berckmans, M. Messagie, J. Smekens, N. Omar, L. Vanhaverbeke, and J. V. Mierlo, “Cost projection of state of the art lithium-ion batteries for electric vehicles up to 2030,” *Energies*, vol. 10, no. 9, pp. 1314, Sep. 2017.

[8] I. Saba, M. Ullah, and M. Tariq, “Advancing electric vehicle battery analysis with digital twins in intelligent transportation systems,” *IEEE Trans. Intell. Transp. Syst.*, vol. 25, no. 9, pp. 12141–12150, Sep. 2024.

[9] Z. Wei, H. Ruan, Y. Li, J. Li, C. Zhang, and H. He, “Multistage state of health estimation of lithium-ion battery with high tolerance to heavily partial charging,” *IEEE Trans. Power Electron.*, vol. 37, no. 6, pp. 7432–7442, Jun. 2022.

[10] W. Q. T. Poh, Y. Xu, and R. T. P. Tan, “A review of machine learning applications for li-Ion battery state estimation in electric vehicles,” in *2022 IEEE PES Innovative Smart Grid Technologies – Asia (ISGT Asia)*, Singapore, Nov. 2022, pp. 265–269.

[11] A. Jose and S. Shrivastava, “Evolution of electrical vehicles, battery state estimation, and future research directions: A critical review,” *IEEE Access*, vol. 12, pp. 158627–158646, Oct. 2024.

[12] W. Vermeer, G. R. Chandra Mouli, and P. Bauer, “A comprehensive review on the characteristics and modeling of lithium-ion battery aging,” *IEEE Trans. Transp. Electrific.*, vol. 8, no. 2, pp. 2205–2232, Jun. 2022.

[13] P. Shrivastava, P. A. Naidu, S. Sharma, B. K. Panigrahi, and A. Garg, “Review on technological advancement of lithium-ion battery states estimation methods for electric vehicle applications,” *J. Energy Storage*, vol. 64, pp. 107159, Aug. 2023.

[14] X. Chen, H. Lei, R. Xiong, W. Shen, and R. Yang, “A novel approach to reconstruct open circuit voltage for state of charge estimation of lithium ion batteries in electric vehicles,” *Appl. Energy*, vol. 255, pp. 113758, Dec. 2019.

[15] G. S. Misyris, D. I. Doukas, T. A. Papadopoulos, D. P. Labridis, and V. G. Agelidis, “State-of-charge estimation for li-ion batteries: A more accurate hybrid approach,” *IEEE Trans. Energy Convers.*, vol. 34, no. 1, pp. 109–119, Mar. 2019.

[16] Z. He, Z. Yang, X. Cui, and E. Li, “A method of state-of-charge estimation for EV power lithium-ion battery using a novel adaptive extended Kalman filter,” *IEEE Trans. Veh. Technol.*, vol. 69, no. 12, pp. 14618–14630, Dec. 2020.

[17] R. Xiong, J. Tian, H. Mu, and C. Wang, “A systematic model-based degradation behavior recognition and health monitoring method for lithium-ion batteries,” *Appl. Energy*, vol. 207, pp. 372–383, Dec. 2017.

[18] X. Chen *et al.*, “State of health (SoH) estimation and degradation modes analysis of pouch NMC532/graphite li-ion battery,” *J. Power Sources*, vol. 498, pp. 229884, Jun. 2021.

[19] M. K. S. Verma *et al.*, “On-board state estimation in electrical vehicles: Achieving accuracy and computational efficiency through an electrochemical model,” *IEEE Trans. Veh. Technol.*, vol. 69, no. 3, pp. 2563–2575, Mar. 2020.

[20] S. Amir, M. Gulzar, M. O. Tarar, I. H. Naqvi, N. A. Zaffar, and M. G. Pecht, “Dynamic equivalent circuit model to estimate state-of-health of lithium-ion batteries,” *IEEE Access*, vol. 10, pp. 18279–18288, Feb. 2022.

[21] M. Ng, J. Zhao, Q. Yan, G. J. Conduit, and Z. W. Seh, “Predicting the state of charge and health of batteries using data-driven machine learning,” *Nature Mach. Intell.*, vol. 2, pp. 161–170, Mar. 2020.

[22] N. Li, F. He, W. Ma, R. Wang, L. Jiang, and X. Zhang, “An indirect state-of-health estimation method based on improved genetic and back propagation for online lithium-ion battery used in electric vehicles,” *IEEE Trans. Veh. Technol.*, vol. 71, no. 12, pp. 12682–12690, Dec. 2022.

[23] Z. Pang, K. Yang, Z. Song, P. Niu, G. Chen, and J. Meng, “A new method for determining SOH of lithium batteries using the real-part ratio of EIS specific frequency impedance,” *J. Energy Storage*, vol. 72, part D, pp. 108693, Nov. 2023.

[24] C. J. Ko and K. C. Chen, “Using tens of seconds of relaxation voltage to estimate open circuit voltage and state of health of lithium ion batteries,” *Appl. Energy*, vol. 357, pp. 122488, Mar. 2024.

[25] S. Zhang, X. Guo, X. Dou, and X. Zhang, “A rapid online calculation method for state of health of lithium-ion battery based on coulomb counting method and differential voltage analysis,” *J. Power Sources*, vol. 479, pp. 228740, Dec. 2020.

[26] D. Zhang, S. Dey, L. D. Couto, and S. J. Moura, “Battery adaptive observer for a single-particle model with intercalation-induced stress,” *IEEE Trans. Control Syst. Technol.*, vol. 28, no. 4, pp. 1363–1377, Jul. 2020.

[27] Y. Gao, K. Liu, C. Zhu, X. Zhang, and D. Zhang, “Co-estimation of state-of-charge and state-of-health for lithium-ion batteries using an enhanced electrochemical model,” *IEEE Trans. Ind. Electron.*, vol. 69, no. 3, pp. 2684–2696, Mar. 2022.

[28] X. Ding, D. Zhang, J. Cheng, B. Wang, and P. C. K. Luk, “An improved Thevenin model of lithium-ion battery with high accuracy for electric vehicles,” *Appl. Energy*, vol. 254, pp. 113615, Nov. 2019.

[29] Q. Wang, Z. Wang, L. Zhang, P. Liu, and Z. Zhang, “A novel consistency evaluation method for series-connected battery systems based on real-world operation data,” *IEEE Trans. Transp. Electrific.*, vol. 7, no. 2, pp. 437–451, Jun. 2021.

[30] M. Hossain, S. Saha, M. T. Arif, A. M. T. Oo, N. Mendis, and M. E. Haque, “A parameter extraction method for the li-ion batteries with wide-range temperature compensation,” *IEEE Trans. Ind. Appl.*, vol. 56, no. 5, pp. 5625–5636, Oct. 2020.

[31] Y. Zou, X. Hu, H. Ma, and S. E. Li, “Combined state of charge and state of health estimation over lithium-ion battery cell cycle lifespan for electric vehicles,” *J. Power Sources*, vol. 273, pp. 793–803, Jan. 2017.

[32] D. Deng, S. Y. Liu, S. L. Wang, L. L. Xia, and L. Chen, “An improved second-order electrical equivalent modeling method for the online high power li-ion battery state of charge estimation,” in *2021 IEEE 12th Energy Convers. Congr. & Expo. – Asia (ECCE Asia)*, Singapore, May 2021, pp. 1725–1729.

[33] M. F. Bauomy, H. Gamal, and A. A. Shaltout, “Dynamic modeling of DC nanogrid local branch using enhanced PV and third order battery models,” in *2016 18th Eur. Conf. on Power Electron. and Appl. (EPE'16 ECCE Europe)*, Karlsruhe, Germany, Sep. 2016, pp. 1–10.

[34] G. Dong, Z. Chen, J. Wei, and Q. Ling, “Battery health prognosis using Brownian motion modeling and particle filtering,” *IEEE Trans. Ind. Electron.*, vol. 65, no. 11, pp. 8646–8655, Nov. 2018.

[35] F. Zhu and J. Fu, “A novel state-of-health estimation for lithium-ion battery via unscented Kalman filter and improved unscented particle filter,” *IEEE Sensors J.*, vol. 21, no. 22, pp. 25449–25456, Nov. 2021.

[36] C. Wang, S. Wang, J. Zhou, J. Qiao, X. Yang, and Y. Xie, “A novel back propagation neural network-dual extended Kalman filter method for state-of-charge and state-of-health co-estimation of lithium-ion batteries based on limited memory least square algorithm,” *J. Energy Storage*, vol. 59, pp. 106563, Mar. 2023.

[37] A. P. Renold and N. S. Kathayat, “Comprehensive review of machine learning, deep learning, and digital twin data-driven approaches in battery health prediction of electric vehicles,” *IEEE Access*, vol. 12, pp. 43984–43999, Mar. 2024.

[38] W. Q. T. Poh, Y. Xu, W. Liu, and R. T. P. Tan, “Momentary informatics based data-driven estimation of lithium-ion battery health under dynamic discharging currents,” *J. Power Sources*, vol. 629, pp. 236041, Feb. 2025.

[39] M. Landi and G. Gross, “Measurement techniques for online battery state of health estimation in vehicle-to-grid applications,” *IEEE Trans. Instrum. Meas.*, vol. 63, no. 5, pp. 1224–1234, May 2016.

[40] P. Ananto, F. Syabani, W. D. Indra, O. Wahyunggoro, and A. I. Cahyadi, “The state of health of li-po batteries based on the battery's parameters and a fuzzy logic system,” in *Joint Int. Conf. on Rural Inf. & Commun. Technol. and Electric-Veh. Technol. (rICT & ICeV-T)*, Bandung, Indonesia, Nov. 2016, pp. 1–4.

[41] J. Tang, Q. Liu, S. Liu, X. Xie, J. Zhou, and Z. Li, “A health monitoring method based on multiple indicators to eliminate influences of estimation dispersion for lithium-ion batteries,” *IEEE Access*, vol. 7, pp. 122302–122314, Aug. 2019.

[42] X. Li, D. Fan, X. Liu, S. Xu, and B. Huang, “State of health estimation for lithium-ion batteries based on improved bat algorithm optimization kernel extreme learning machine,” *J. Energy Storage*, vol. 101, part A, pp. 113756, Nov. 2024.

[43] D. Yang, Y. Wang, R. Pan, R. Chen, and Z. Chen, “A neural network based state-of-health estimation of lithium-ion battery in electric vehicles,” *Energy Procedia*, vol. 105, pp. 2059–2064, May 2017.

[44] A. Bracale, P. De Falco, L. P. D. Noia, and R. Rizzo, “Probabilistic state of health and remaining useful life prediction for li-Ion batteries,” *IEEE Trans. Ind. Appl.*, vol. 59, no. 1, pp. 578–590, Feb. 2023.

[45] J. Wu, Y. Wang, X. Zhang, and Z. Chen, “A novel state of health estimation method of li-ion battery using group method of data handling,” *J. Power Sources*, vol. 327, pp. 457–464, Sep. 2016.

[46] J. Kim, J. Yu, M. Kim, K. Kim, and S. Han, “Estimation of li-ion battery state of health based on multilayer perceptron: as an EV application,” *IFAC-PapersOnLine*, vol. 51, no. 28, pp. 392–397, 2018.

[47] C. She, Y. Li, C. Zou, T. Wik, Z. Wang, and F. Sun, “Offline and online blended machine learning for lithium-ion battery health state estimation,” *IEEE Trans. Transp. Electrific.*, vol. 8, no. 2, pp. 1604–1618, Jun. 2022.

[48] X. Tan, D. Zhan, P. Lyu, J. Rao, and Y. Fan, “Online state-of-health estimation of lithium-ion battery based on dynamic parameter identification at multi timescale and support vector regression,” *J. Power Sources*, vol. 484, pp. 229233, Feb. 2021.

[49] Z. Chen, M. Sun, X. Shu, R. Xiao, and J. Shen, “Online state of health estimation for lithium-ion batteries based on support vector machine,” *Appl. Sciences*, vol. 8, no. 6, pp. 925, Jun. 2018.

[50] C. Vidal, P. Malysz, P. Kollmeyer, and A. Emadi, “Machine learning applied to electrified vehicle battery state of charge and state of health estimation: State-of-the-art,” *IEEE Access*, vol. 8, pp. 52796–52814, Mar. 2020.

[51] Z. Wei, X. Han, and J. Li, “State of health assessment for echelon utilization batteries based on deep neural network learning with error correction,” *J. Energy Storage*, vol. 51, pp. 104428, Jul. 2022.

[52] M. Haris, M. N. Hasan, and S. Qin, “Degradation curve prediction of lithium-ion batteries based on knee point detection algorithm and convolutional neural network,” *IEEE Trans. Instrum. Meas.*, vol. 71, pp. 1–10, Jun. 2022.

[53] H. Chaoui and C. C. Ibe-Ekeocha, “State of charge and state of health estimation for lithium batteries using recurrent neural networks,” *IEEE Trans. Veh. Technol.*, vol. 66, no. 10, pp. 8773–8783, Oct. 2017.

[54] J. Hong *et al.*, “A novel state of health prediction method for battery system in real-world vehicles based on gated recurrent unit neural networks,” *Energy*, vol. 289, pp. 129918, Feb. 2024.

[55] S. Kim, Y. Y. Choi, K. J. Kim, and J. Choi, “Forecasting state-of-health of lithium-ion batteries using variational long short-term memory with transfer learning,” *J. Energy Storage*, vol. 41, pp. 102893, Sep. 2021.

[56] P. Khumprom and N. Yodo, “A data-driven predictive prognostic model for lithium-ion batteries based on a deep learning algorithm,” *Energies*, vol. 12, no. 4, pp. 660, Feb. 2019.

[57] A. Poernomo and D. K. Kang, “Biased dropout and crossmap dropout: Learning towards effective dropout regularization in convolutional neural network,” *Neural Netw.*, vol. 104, pp. 60–67, Aug. 2018.

[58] M. K. Tran *et al.*, “A comprehensive equivalent circuit model for lithium-ion batteries, incorporating the effects of state of health, state of charge, and temperature on model parameters,” *J. Energy Storage*, vol. 43, pp. 103252, Nov. 2021.

[59] H. Liu *et al.*, “An analytical model for the CC-CV charge of li-ion batteries with application to degradation analysis,” *J. Energy Storage*, vol. 29, pp. 101342, Jun. 2020.

[60] J. Yang, B. Xia, W. Huang, Y. Fu, and C. Mi, “Online state-of-health estimation for lithium-ion batteries using constant-voltage charging current analysis,” *Appl. Energy*, vol. 212, pp. 1589–1600, Feb. 2018.

[61] M. Lin, D. Wu, S. Chen, J. Meng, W. Wang, and J. Wu, “Battery health prognosis based on sliding window sampling of charging curves and independently recurrent neural network,” *IEEE Trans. Instrum. Meas.*, vol. 73, pp. 1–9, Jan. 2024.

[62] E. Schaltz, D. I. Stroe, K. Nørregaard, L. S. Ingvardsen, and A. Christensen, “Incremental capacity analysis applied on electric vehicles for battery state-of-health estimation,” *IEEE Trans. Ind. Appl.*, vol. 57, no. 2, pp. 1810–1817, Apr. 2021.

[63] S. Zhang, X. Guo, X. Dou, and X. Zhang, “A rapid online calculation method for state of health of lithium-ion battery based on coulomb counting method and differential voltage analysis,” *J. Power Sources*, vol. 479, pp. 228740, Dec. 2020.

[64] M. Cao, T. Zhang, B. Yu, and Y. Liu, “A method for interval prediction of satellite battery state of health based on sample entropy,” *IEEE Access*, vol. 7, pp. 141549–141561, Sep. 2019.

[65] X. Hu, J. Jiang, D. Cao, and B. Egardt, “Battery health prognosis for electric vehicles using sample entropy and sparse bayesian predictive modeling,” *IEEE Trans. Ind. Electron.*, vol. 63, no. 4, pp. 2645–2656, Apr. 2016.

[66] T. Ouyang, P. Xu, J. Lu, X. Hu, B. Liu, and N. Chen, “Co-estimation of state-of-charge and state-of-health for power batteries based on multithread dynamic optimization method,” *IEEE Trans. Ind. Electron.*, vol. 69, no. 2, pp. 1157–1166, Feb. 2022.

[67] S. Jia, B. Ma, W. Guo, and Z. S. Li, “A sample entropy based prognostics method for lithium-ion batteries using relevance vector machine,” *J. Manuf. Syst.*, vol. 61, pp. 773–781, Oct. 2021.

[68] D. Liu, W. Xie, H. Liao, and Y. Peng, “An integrated probabilistic approach to lithium-ion battery remaining useful life estimation,” *IEEE Trans. Instrum. Meas.*, vol. 64, no. 3, pp. 660–670, Mar. 2015.

[69] Y. Zhou, M. Huang, Y. Chen, and Y. Tao, “A novel health indicator for on-line lithium-ion batteries remaining useful life prediction,” *J. Power Sources*, vol. 321, pp. 1–10, Jul. 2019.

[70] Z. Deng, X. Hu, X. Lin, L. Xu, Y. Che, and L. Hu, “General discharge voltage information enabled health evaluation for lithium-ion batteries,” *IEEE/ASME Trans. Mechatronics*, vol. 26, no. 3, pp. 1295–1306, Jun. 2021.

[71] W. Liu, Y. Xu, and X. Feng, “A hierarchical and flexible data-driven method for online state-of-health estimation of li-ion battery,” *IEEE Trans. Veh. Technol.*, vol. 69, no. 12, pp. 14739–14748, Dec. 2020.

[72] D. Liu, Y. Song, L. Li, H. Liao, and Y. Peng, “On-line life cycle health assessment for lithium-ion battery in electric vehicles,” *J. Cleaner Prod.*, vol. 199, pp. 1050–1065, Oct. 2018.

[73] W. Liu and Y. Xu, “Data-driven online health estimation of li-ion batteries using a novel energy-based health indicator,” *IEEE Trans. Energy Convers.*, vol. 35, no. 3, pp. 1715–1718, Sep. 2020.

[74] H. Zhang, Y. Su, F. Altaf, T. Wik, and S. Gros, “Interpretable battery cycle life range prediction using early cell degradation data,” *IEEE Trans. Transp. Electrific.*, vol. 9, no. 2, pp. 2669–2682, Jun. 2023.

[75] S. Greenbank and D. Howey, “Automated feature extraction and selection for data-driven models of rapid battery capacity fade and end of life,” *IEEE Trans. Ind. Inform.*, vol. 18, no. 5, pp. 2965–2973, May 2022.

[76] B. Bole, C. Kulkarni, and M. Daigle, “Randomized battery usage dataset,” *NASA Prognostics Data Repository*, NASA Ames Research Center, Moffett Field, CA, USA, Oct. 2022.

[77] P. Mohtat, J. B. Siegel, A. G. Stefanopoulou, and S. Lee, “Pouch cell voltage and expansion cyclic aging datasets,” *Univ. of Michigan – Deep Blue Data*, U-M Battery Lab, Ann Arbor, MI, USA, Apr. 2024.

[78] Infineon Technologies AG (Automotive), “In-house datasets: WLTP-LFP batteries,” *confluencewikiprod.intra.infineon.com*. https://confluencewikiprod.intra.infineon.com/display/ABMS/In+House+Datasets (accessed May 7, 2024).

[79] Z. Wang, C. Yuan, and X. Li, “Lithium battery state-of-health estimation via differential thermal voltammetry with Gaussian process regression,” *IEEE Trans. Transp. Electrific.*, vol. 7, no. 1, pp. 16–25, Mar. 2021.

[80] J. Liu and Z. Chen, “Remaining useful life prediction of lithium-ion batteries based on health indicator and Gaussian process regression model,” *IEEE Access*, vol. 7, pp. 39474–39484, Mar. 2019.

[81] W. Q. T. Poh, Y. Xu, and R. T. P. Tan, “Data-driven estimation of li-ion battery health using a truncated time-based indicator and LSTM,” in *2023 IEEE Power & Energy Soc. General Meeting (PESGM)*, Orlando, FL, USA, Jul. 2023, pp. 1–5.

[82] J. Zhang and Wei Lu, “Sparse data machine learning for battery health estimation and optimal design incorporating material characteristics,” *Appl. Energy*, vol. 307, pp. 118165, Feb. 2022.

[83] J. A. Braun, R. Behmann, D. Schmider, and W. G. Bessler, “State of charge and state of health diagnosis of batteries with voltage-controlled models,” *J. Power Sources*, vol. 544, pp. 231828, Oct. 2022.

[84] J. Wei and G. Dong, “Remaining useful life prediction and state of health diagnosis for lithium-ion batteries using particle filter and support vector regression,” *IEEE Trans. Ind. Electron.*, vol. 65, pp. 634–643, Jul. 2019.

[85] T. Tang and H. Yuan, “The capacity prediction of li-ion batteries based on a new feature extraction technique and an improved extreme learning machine algorithm,” *J. Power Sources*, vol. 514, pp. 230572, Dec. 2021.

[86] T. Oji, Y. Zhou, S. Ci, F. Kang, X. Chen, and X. Liu, “Data-driven methods for battery SOH estimation: survey and a critical analysis,” *IEEE Access*, vol. 9, pp. 126903–126916, Sep. 2021.

[87] X. Li, C. Yuan, and Z. Wang, “Multi-time-scale framework for prognostic health condition of lithium battery using modified Gaussian process regression and nonlinear regression,” *J. Power Sources*, vol. 467, pp. 228358, Aug. 2020.

[88] B. Gou, Y. Xu, and X. Feng, “State-of-health estimation and remaining-useful-life prediction for lithium-ion battery using a hybrid data-driven method,” *IEEE Trans. Veh. Technol.*, vol. 69, no. 10, pp. 10854–10867, Oct. 2020.

[89] D. Ji, Z. Wei, C. Tian, H. Cai, and J. Zhao, “Deep transfer ensemble learning-based diagnostic of lithium-ion battery,” *IEEE/CAA J. Automatica Sinica*, vol. 10, no. 9, pp. 1899–1901, Sep. 2023.

[90] L. Cai *et al.*, “A unified deep learning optimization paradigm for lithium-ion battery state-of-health estimation,” *IEEE Trans. Energy Convers.*, vol. 39, no. 1, pp. 589–600, Mar. 2024.

[91] J. Zhao *et al.*, “Battery prognostics and health management from a machine learning perspective,” *J. Power Sources*, vol. 581, pp. 233474, Oct. 2023.

[92] K. S. R. Mawonou, A. Eddahech, D. Dumur, D. Beauvois, and E. Godoy, “State-of-health estimators coupled to a random forest approach for lithium-ion battery aging factor ranking,” *J. Power Sources*, vol. 484, pp. 229154, Feb. 2021.

[93] Y. Zhao, Z. Wang, Z. Sun, P. Liu, D. Cui, and J. Deng, “Data-driven lithium-ion battery degradation evaluation under overcharge cycling conditions,” *IEEE Trans. Power Electron.*, vol. 38, no. 8, pp. 10138–10150, Aug. 2023.

[94] C. Zhang, S. Zhao, Z. Yang, and Y. Chen, “A reliable data-driven state-of-health estimation model for lithium-ion batteries in electric vehicles,” *Front. Energy Res.*, vol. 10, pp. 1–16, Sep. 2022.

[95] L. Luo *et al.*, “Battery SOH estimation method based on gradual decreasing current, double correlation analysis and GRU,” *Green Energy & Intell. Transp.*, vol. 2, no. 5, pp. 100108, Oct. 2023.

[96] C. Zhang *et al.*, “Flexible method for estimating the state of health of lithium-ion batteries using partial charging segments,” *Energy*, vol. 295, pp. 131009, May 2024.

[97] F. Naseri, E. Farjah, T. Ghanbari, Z. Kazemi, E. Schaltz, and J. L. Schanen, “Online parameter estimation for supercapacitor state-of-energy and state-of-health determination in vehicular applications,” *IEEE Trans. Ind. Electron.*, vol. 67, no. 9, pp. 7963–7972, Sep. 2020.

[98] Z. Haddad *et al.*, “Advancements and comprehensive overview of thermal management systems for lithium-ion batteries: Nanofluids and phase change materials approaches,” *J. Power Sources*, vol. 603, pp. 234382, May 2024.

[99] Z. Wei, K. Liu, X. Liu, Y. Li, L. Du, and F. Gao, “Multilevel data-driven battery management: From internal sensing to big data utilization,” *IEEE Trans. Transp. Electrific.*, vol. 9, no. 4, pp. 4805–4823, Dec. 2023.

[100] S. Nyamathulla and C. Dhanamjayulu, “A review of battery energy storage systems and advanced battery management system for different applications: Challenges and recommendations,” *J. Energy Storage*, vol. 86, part A, pp. 111179, May 2024.

[101] H. Wang, H. Xu, and Z. Zhang, “High-dimensional multi-objective Bayesian optimization with block coordinate updates: Case studies in intelligent transportation system,” *IEEE Trans. Intell. Transp.*, vol. 25, no. 1, pp. 884–895, Jan. 2024.

[102] Y. Shang, S. Wang, N. Tang, Y. Fu, and K. Wang, “Research progress in fault detection of battery systems: A review,” *J. Energy Storage*, vol. 98, part A, pp. 113079, Sep. 2024.

[103] Y. Liu, Q. Li, and K. Wang, “Revealing the degradation patterns of lithium-ion batteries from impedance spectroscopy using variational auto-encoders,” *Energy Storage Materials*, vol. 69, pp. 103394, May 2024.

[104] Z. Deng, X. Lin, J. Cai, and X. Hu, “Battery health estimation with degradation pattern recognition and transfer learning,” *J. Power Sources*, vol. 525, pp. 231027, Mar. 2022.

[105] G. Sun, Y. Cong, Q. Wang, B. Zhong, and Y. Fu, “Representative task self-selection for flexible clustered lifelong learning,” *IEEE Trans. Neural Netw. Learn. Syst.*, vol. 33, no. 4, pp. 1467–1481, Apr. 2022.

[106] N. Mughal, G. Mujtaba, S. Shaikh, A. Kumar, and S. M. Daudpota, “Comparative analysis of deep natural networks and large language models for aspect-based sentiment analysis,” *IEEE Access*, vol. 12, pp. 60943–60959, Apr. 2024.

[107] S. Dhingra, M. Singh, S. Vaisakh, N. Malviya, and S. S. Gill, “Mind meets machine: Unravelling GPT-4’s cognitive psychology,” *BenchCouncil Trans. Benchmarks, Standards and Eval.*, vol. 3, pp. 100139, Sep. 2023.

[108] W. Q. T. Poh, Y. Xu, and R. T. P. Tan, “Data-driven estimation of li-ion battery health: Integrating GPT-4 with distilled lifelong learning,” *IEEE Trans. Energy Convers.*, vol. 40, no. 2, pp. 1682–1685, Jun. 2025.